Non-invasive quantification of CNS pathology with dynamic PET information:
Investigation of advanced methods for the characterisation of multiple sclerosis and glioma lesions

Lena Kaiser geb. Vomacka

2019

Aus der Klinik und Poliklinik für Nuklearmedizin - Campus Großhadern
der Ludwig-Maximilians-Universität München

Direktor: Prof. Dr. Peter Bartenstein

Non-invasive quantification of CNS pathology with dynamic PET information:
Investigation of advanced methods for the characterisation of multiple sclerosis and glioma lesions

Kumulative Dissertation
zum Erwerb des Doktorgrades der Naturwissenschaften (Dr. rer. nat.)
an der Medizinischen Fakultät
der Ludwig–Maximilians–Universität zu München

vorgelegt von
Lena Kaiser geb. Vomacka
aus München

2019

Mit Genehmigung der Medizinischen Fakultät
der Universität München

Betreuer:	Priv. Doz. Dr. Guido Böning
Zweitgutachter:	Prof. Dr. Olaf Dietrich
Dekan:	Prof. Dr. Reinhard Hickel
Tag der mündlichen Prüfung:	27.06.2019

Eidesstattliche Versicherung

Kaiser geb. Vomacka, Lena

Ich erkläre hiermit an Eides statt,

dass ich die vorliegende Dissertation mit dem Thema

Non-invasive quantification of CNS pathology with dynamic PET information: Investigation of advanced methods for the characterisation of multiple sclerosis and glioma lesions

selbständig verfasst, mich außer der angegebenen keiner weiteren Hilfsmittel bedient und alle Erkenntisse, die aus dem Schriftum ganz oder annährend übernommen sind, als solche kenntlich gemacht habe und nach ihrer Herkunft und Bezeichnung der Fundstelle einzeln nachgewiesen habe.

Ich erkläre des Weiteren, dass die hier vorgelegte Dissertation nicht in gleicher oder in ähnlicher Form bei einer anderen Stelle zur Erlangung eines akademischen Grades eingereicht wurde.

Lena Kaiser geb. Vomacka

München, 09.07.2019

Contents

Nomenclature

TSPO	18-kDa translocator protein
AAT	Amino acid transporter
ANCOVA	Analysis of covariance
ANOVA	Analysis of variance
AUC	Area under the curve
BP	Binding potential
BS	Blood sampling
BBB	Blood-brain barrier
BRT	Boundary reproducing threshold
CNS	Central nervous system
COV	Coefficient of variation
CA	Contrast agent
CE	Contrast-enhanced
AIC$_C$	Corrected Akaike information criterion
DVR	Distribution volume ratio
DCE	Dynamic contrast-enhanced
EC	Electron capture
E	Extraction fraction
FPR	False positive rate
FBP	Filtered back-projection
FC	Frontal cortex
GA	Graphical analysis
GLCM	Grey level co-occurrence matrix

HAB	High affinity binder
HGG	High-grade glioma
HPLC	High-pressure liquid chromatography
IDIF	Image-derived input function
IRF	Impulse response function
IF	Input function
IDH	Isocitrate dehydrogenase
LOR	Line of response
LAB	Low affinity binder
LGG	Low-grade glioma
MRI	Magnetic resonance imaging
MLEM	Maximum likelihood expectation maximisation
MAB	Medium affinity binder
MTF	Modulation transfer function
MNI	Montreal Neurological Institute
MS	Multiple sclerosis
MLRM	Multivariate linear regression model
K_i	Net influx rate
1TC	One-tissue compartment model
OSEM	Ordered subsets expectation maximisation
PVE	Partial volume effect
PVF	Percentage volume fraction
PVH	Percentage volume histogram
F	Perfusion
PSF	Permeability surface area product
PSF	Point spread function
PET	Positron emission tomography
PML	Progressive multifocal leukoencephalopathy
PMS	Progressive multiple sclerosis

PRR　　　　　Pseudo-reference region

ROC　　　　　Receiver-operating characteristics

RT　　　　　　Reference tissue

RRMS　　　　Relapsing-remitting multiple sclerosis

RE　　　　　　Relative equilibrium

SBR　　　　　Signal-to-background ratio

SPECT　　　　Single photon emission computed tomography

SUV　　　　　Standardised uptake value

SUVR　　　　 Standardised uptake value ratio

SPM　　　　　Statistical parametric mapping

TBR　　　　　Target-to-background ratio

TLC　　　　　Thin layer chromatography

TAC　　　　　Time-activity curve

TTP　　　　　Time-to-peak

2TC　　　　　Two-tissue compartment model

VOI　　　　　Volume of interest

WRSS　　　　Weighted residual sum of squares

List of publications

Original publications included in this cumulative dissertation

In this thesis, the following two publications are summarised to a cumulative dissertation according to the promotion regulation for natural sciences in the medical faculty of the Ludwig-Maximilians-Universität München:

L. Vomacka, N. L. Albert, S. Lindner, M. Unterrainer, C. Mahler, M. Brendel, L. Ermoschkin, A. Gosewisch, A. Brunegraf, C. Buckley, T. Kümpfel, R. Rupprecht, S. Ziegler, M. Kerschensteiner, P. Bartenstein, G. Böning, "TSPO imaging using the novel pet ligand [18F]GE-180: quantification approaches in patients with multiple sclerosis," EJNMMI research, vol. 7, no. 89, pp. 1–9, 2017.

L. Vomacka, M. Unterrainer, A. Holzgreve, E. Mille, A. Gosewisch, J. Brosch, S. Ziegler, B. Suchorska, F.-W. Kreth, J.-C. Tonn, P. Bartenstein, N. L. Albert, and G. Böning, "Voxel-wise analysis of dynamic 18F-FET PET: a novel approach for non-invasive glioma characterisation," EJNMMI research, vol. 8, no. 91, pp. 1–13, 2018.

Further publications

V. Bernard-Gauthier, J. J. Bailey, A. V. Mossine, S. Lindner, **L. Vomacka**, A. Aliaga, X. Shao, C. A. Quesada, P. Sherman, A. Mahringer, A. Kostikov, M. Grand'Maison, P. Rosa-Neto, J.-P. Soucy, A. Thiel, D. R. Kaplan, G. Fricker, B. Wängler, P. Bartenstein, R. Schirrmacher, P. J. H. Scott, "A kinome-wide selective radiolabeled TrkB/C inhibitor for in vitro and in vivo neuroimaging: Synthesis, preclinical evaluation, and first-in-human," J Med Chem, vol. 60, no. 16, pp. 6897–6910, 2017.

N. L. Albert, M. Unterrainer, D. Fleischmann, S. Lindner, F. Vettermann, A. Brunegraf, **L. Vomacka**, M. Brendel, V. Wenter, C. Wetzel, R. Rupprecht, J.-C. Tonn, C. Belka, P. Bartenstein, M. Niyazi, "TSPO pet for glioma imaging using the novel ligand 18F-GE-180: first results in patients with glioblastoma," Eur J Nucl Med Mol Imaging, vol. 44, no. 13, pp. 2230–2238, 2017.

M. Deussing, T. Blume, **L. Vomacka**, C. Mahler, C. Focke, A. Todica, M. Unterrainer, N. L. Albert, S. Lindner, B. von Ungern-Sternberg, K. Baumann, A. Zwergal,

P. Bartenstein, J. Herms, A. Rominger, M. Brendel, "Coupling between physiological TSPO expression in brain and myocardium allows stabilization of late-phase cerebral [18F]GE180 PET quantification," NeuroImage, vol. 165, pp. 83–91, 2018.

M. Unterrainer, C. Mahler, **L. Vomacka**, S. Lindner, J. Havla, M. Brendel, G. Böning, B. Ertl-Wagner, T. Kümpfel, V. Milenkovic, R Rupprecht, M. Kerschensteiner, P. Bartenstein, N. L. Albert, "TSPO PET with [18F]GE-180 sensitively detects focal neuroinflammation in patients with relapsing-remitting multiple sclerosis," Eur J Nucl Med Mol Imaging, vol. 45, no. 8, pp. 1423–1431, 2018.

M. Deussing, T. Blume, **L. Vomacka**, C. Mahler, C. Focke, A. Todica, M. Unterrainer, N. L. Albert, S. Lindner, B. von Ungern-Sternberg, K. Baumann, A. Zwergal, P. Bartenstein, J. Herms, A. Rominger, M. Brendel, "Data on specificity of [18F]GE180 uptake for TSPO expression in rodent brain and myocardium," Data in Brief, vol. 19, pp. 331–336, 2018.

A. Gosewisch, A. Delker, S. Tattenberg, H. Ilhan, A. Todica, J. Brosch, **L. Vomacka**, A. Brunegraf, F. J. Gildehaus, S. Ziegler, P. Bartenstein, G. Böning, "Patient-specic image-based bone marrow dosimetry in Lu-177-[DOTA0,Tyr3]-Octreotate and Lu-177-DKFZ-PSMA-617 therapy: investigation of a new hybrid image approach," EJNMMI research, vol. 8, no. 76, pp. 1–16, 2018.

M. Unterrainer, D. Fleischmann, C. Diekmann, **L. Vomacka**, S. Lindner, F. Vettermann, M. Brendel, V. Wenter, B. Ertl-Wagner, J. Herms, C. Wetzel, R. Rupprecht, J.-C. Tonn, C. Belka, P. Bartenstein, K.-M. Niyazi, and N. L. Albert, "Comparison of 18F-GE-180 and dynamic 18F-FET PET in high grade glioma: a double tracer pilot study," Eur J Nucl Med Mol Imaging, pp. 1–11, 2018.

C. Mahler, M. Unterrainer, C. Muth, R. Egensperger, **L. Vomacka**, S. Lindner, B. Ertl-Wagner, M. Patzig, P. Bartenstein, N. Albert, M. Kerschensteiner, and T. Kümpfel, "Imaging microglial activation in tacrolimus-associated CNS vasculitis with translocator protein PET," Neurology, vol. 91, no. 20, pp. 936–937, 2018.

Conference abstracts

L. Vomacka, A. Delker, A. Gosewisch, W. Fendler, P. Bartenstein, and G. Böning, "Automatische Bildsegmentierung für die 3D Dosimetrie unter Verwendung eines robusten Cluster Algorithmus auf 4D SPECT Daten bei der Therapie von Patienten mit kastrationsresistentem metastasierten Prostatakarzinom mit Lu-177 DKFZ-PSMA-617," in *Nuklearmedizin 2016 – 54. Jahrestagung der Deutschen Gesellschaft für Nuklearmedizin*, no. V72, (Dresden), Thieme, 2016.

L. Vomacka, N. Albert, E. Mille, B. Suchorska, M. Unterrainer, P. Bartenstein, and G. Boening, "Comparison of pharmacokinetic parameters in dynamic 18F-FET PET of glioma," J Nucl Med, vol. 57, no. supplement 2, pp. 370–370, 2016.

L. Vomacka, A. Gosewisch, A. Delker, W. Fendler, P. Bartenstein, and G. Böning,

"Automatic image segmentation for 3D dosimetry in Lu-177 DKFZ-PSMA-617 therapy of castrate-resistant metastatic prostate cancer using a robust cluster algorithm on 4D SPECT data," J Nucl Med, vol. 57, no. supplement 2, pp. 497–497, 2016.

L. Vomacka, A. Delker, A. Gosewisch, F. Wolfgang, F.-J. Gildehaus, A. Brunegraf, P. Bartenstein, and G. Böning, "Automatic image segmentation for efficient 3D dosimetry with reduced influence of registration-errors and noise in Lu-177 DKFZ-PSMA-617 therapy using a robust cluster algorithm on sequential SPECT data and subsequent voxel-wise re-scaling," in *Annual Congress of the European Association of Nuclear Medicine 2016*, no. OP111, (Barcelona), Eur J Nucl Med Mol Imaging, Springer, 2016.

L. Vomacka, N. L. Albert, E. Mille, B. Suchorska, M. Unterrainer, A. Gosewisch, P. Bartenstein, and G. Böning, "3D analysis of glioma heterogeneity with pseudo-kinetic and pharmacokinetic model parameters in dynamic 18F-FET PET," in Annual Congress of the European Association of Nuclear Medicine 2016, no. OP650, (Barcelona), Eur J Nucl Med Mol Imaging, Springer, 2016.

L. Vomacka, N. L. Albert, M. Unterrainer, S. Lindner, A. Brunegraf, L. Ermoschkin, A. Gosewisch, C. Mahler, T. Kümpfel, M. Kerschensteiner, P. Bartenstein, and G. Böning, "Quantizierung des neuen TSPO Liganden F-18-GE-180 bei Multipler Sklerose – erste Ergebnisse," in *Nuklearmedizin 2017 – 55. Jahrestagung der Deutschen Gesellschaft für Nuklearmedizin*, no. V101, (Dresden), Thieme, 2017.

L. Vomacka, V. Heigl, J. Zellmer, H. Ilhan, A. Gosewisch, P. Bartenstein, and G. Böning, "Quantizierung der Nierenfunktion nach Peptidrezeptor-Therapie anhand eines erweiterten FUR Modells am Beispiel dynamischer Tc-99m-MAG3 Szintigraphie in Mäusen," in *Nuklearmedizin 2017 – 55. Jahrestagung der Deutschen Gesellschaft für Nuklearmedizin*, no. V140, (Dresden), Thieme, 2017.

L. Vomacka, N. Albert, S. Lindner, M. Unterrainer, C. Mahler, M. Brendel, L. Ermoschkin, A. Gosewisch, A. Brunegraf, T. Kümpfel, M. Kerschensteiner, P. Bartenstein, and G. Böning, "Quantication of the new TSPO ligand [18F]GE-180 in patients with multiple sclerosis-initial results," J Nucl Med, vol. 58, no. supplement 1, pp. 208–208, 2017.

L. Vomacka, N. L. Albert, M. Unterrainer, A. Holzgreve, E. Mille, A. Gosewisch, B. Suchorska, P. Bartenstein, and G. Böning, "Voxel-weise Analyse der dynamischen F-18-FET PET ermöglicht Dierenzierung von low und high grade Gliomen," in *Nuklearmedizin 2018 – 56. Jahrestagung der Deutschen Gesellschaft für Nuklearmedizin*, no. V12, (Bremen), Thieme, 2018.

L. Vomacka, M. Unterrainer, A. Holzgreve, E. Mille, A. Gosewisch, J. Brosch, S. Ziegler, B. Suchorska, F.-W. Kreth, J.-C. Tonn, P. Bartenstein, N. L. Albert, and G. Böning, "Voxel-basierte Analyse der dynamischen 18F-FET PET ermöglicht molekulargenetische und histologische Gliom Charakterisierung," in *49. Jahrestagung der Deutschen Gesellschaft für Medizinische Physik*, no. V101, (Nürnberg), Thieme, 2018.

L. Vomacka, M. Unterrainer, A. Holzgreve, E. Mille, A. Gosewisch, J. Brosch, S. Ziegler, B. Suchorska, F.-W. Kreth, J.-C. Tonn, P. Bartenstein, N. L. Albert, and G. Böning, "Voxel-based analysis of dynamic 18F-FET PET enables molecular genetic and histologic glioma characterisation," in *Annual Congress of the European Association of Nuclear Medicine 2018*, no. OP087, (Düsseldorf), Eur J Nucl Med Mol Imaging, Springer, 2018.

Abstract

Diagnostic strategies for assessing brain pathology include clinical and a para-clinical documentation, which is supported by imaging of morphological and functional properties. The pathophysiology of the central nervous system (CNS) can be visualised e. g. by imaging the biodistribution of a specific radio-pharmaceutical with positron emission tomography (PET). This work deals with a non-invasive characterisation of CNS lesions in patients suffering from (1) relapsing-remitting multiple sclerosis (RRMS) or from (2) a glial brain tumour (glioma). In this context – besides biochemical properties such as e. g. the (patho-) physiology of the blood-brain barrier (BBB) – methodological aspects are of paramount importance and will be addressed in this thesis.

First, preliminary phantom measurements were performed, aiming to establish and evaluate methods for the delineation of focal MS and glioma lesions. For this, various segmentation methods and the resulting PET signal within lesion volumes were investigated by performing measurements with a NEMA NU 2-2001 spheres phantom for varying signal-to-background ratios (SBR), background concentrations, and image reconstruction algorithms. The ability to reproduce true boundaries was evaluated for different threshold-based segmentation approaches.

The main goal of the first publication was to establish a reference tissue-based quantification approach – aiming to avoid invasive blood-sampling and long scan durations – for the assessment of acute RRMS lesions with the novel PET tracer ^{18}F-GE-180, which targets the 18-kDa translocator protein (TSPO). Besides the occurrence of acute focal white matter lesions, MS may potentially affect the entire brain especially in progressive state. A voxel-wise comparison of tissue uptake in RRMS patients and healthy controls with statistical parametric mapping (SPM) revealed, that frontal cortex (FC) is least affected by disease, and a normalisation to FC uptake mostly reduced the inter-subject variability of white matter uptake in healthy controls. A method for the exclusion of affected voxels from the FC volume was established, yielding a pseudo-reference region (PRR). The obtained tissue uptake values normalised to the PRR uptake significantly correlated with parameters from pharmacokinetic modelling. A further characterisation of MS lesions with texture and shape parameters might enable e. g. a non-invasive differentiation of focal MS and diffuse progressive multifocal leukoencephalopathy (PML) lesions.

In the second study voxel-wise parametric information derived from dynamic ^{18}F-FET (amino acid) PET images was utilised for non-invasive glioma grading. The ability to distinguish molecular genetic and histologic glioma grades was assessed for different intensity, histogram, texture, shape, and pharmacokinetic modelling parameters. In univariate analysis the highest accuracy for non-invasive grading was obtained for a quantification of parameter distributions based on percentage volume histograms (PVH). Among pharmacokinetic modelling parameters, the most significant differences between

grades were found for transfer rates K_1 and k_2 from 1-tissue compartment model with blood volume fraction (1TC-V_B), k_4 from 2TC-V_B, and parameters from Patlak plots. It has been demonstrated, that e. g. static and kinetic parameter maps provide complementary information, thus enabling the detection of aggressive sub-volumes and tumour heterogeneity.

The presented results are encouraging and form the basis for future applications in clinical routine, enhancing the efficiency and accuracy of diagnostic procedures. The next steps should include a validation of suspected tumour heterogeneity by performing stereotactic biopsies. This might enable the utilisation of multi-parametric and multi-modal information for a voxel-wise classification, or an estimation of probability maps e. g. predicting disease progression or recurrence on a voxel-basis.

Zusammenfassung

Eine diagnostische Beurteilung von Gehirn-Pathologien beinhaltet eine klinische und para-klinische Dokumentation, welche durch morphologische und funktionelle Bildgebung unterstützt wird. Die Pathophysiologie des zentralen Nervensystems (ZNS) kann beispielsweise visualisiert werden, indem die Biodistribution spezifischer Radiopharmazeutika mit Positronen-Emissions-Tomographie (PET) abgebildet wird. Diese Arbeit befasst sich mit der nicht-invasiven Charakterisierung von ZNS-Läsionen in Patienten, die unter schubförmig-remittierender Multipler Sklerose (RRMS) oder einem glialen Hirn-Tumor (Gliom) leiden. In diesem Zusammenhang sind – neben biochemischen Eigenschaften wie z.B. der (Patho-) Physiologie der Blut-Hirn-Schranke (BBB) – methodische Aspekte von besonderer Wichtigkeit und werden in dieser Arbeit adressiert.

Als erstes wurden vorbereitende Phantommessungen durchgeführt, um Methoden für die Segmentierung von fokalen MS und Gliom Läsionen zu etablieren und zu beurteilen. Hierfür wurden verschiedene Segmentierungsmethoden und das resultierende PET Signal innerhalb der Läsions-Volumina durch Messungen mit einem NEMA NU 2-2001 Kugel-Phantom mit verschiedenen Signal-zu-Hintergrund Verhältnissen (SBR), Hintergrund-Konzentrationen und Bildrekonstruktionsalgorithmen untersucht. Die Fähigkeit die wahren Objektgrenzen zu reproduzieren, wurde für verschiedene Grenzwert-basierte Segmentierungsmethoden evaluiert.

Das Hauptziel der ersten Publikation war die Etablierung eines Referenz-Gewebe basierten Ansatzes für die Beurteilung akuter RRMS Läsionen mit dem PET-Tracer ^{18}F-GE-180, welcher spezifisch an das 18-kDa Translokator-Protein (TSPO) bindet, wobei eine invasive Entnahme von Blutproben und lange Scan-Zeiten vermieden werden sollten. Neben dem akuten Auftreten fokaler Läsionen in der weißen Substanz kann MS potenziell das gesamte Gehirn beeinträchtigen, insbesondere im fortgeschrittenem Stadium. Ein Voxel-weiser Vergleich der Tracer-Aufnahme in Gewebe bei RRMS Patienten und gesunden Kontrollen mit statistisch-parametrischem Mapping (SPM) ergab, dass der frontale Kortex (FC) am wenigsten durch die Krankheit beeinträchtigt ist und, dass eine Normierung auf die Tracer-Aufnahme im FC am meisten die Variabilität der Aufnahme in der weißen Substanz zwischen Individuen reduziert. Es wurde eine Methode zum Ausschluss beeinträchtigter Voxel aus dem FC-Volumen etabliert, und somit eine pseudo-Referenz Region (PRR) generiert. Die mit dem PRR-Wert normierte Gewebe-Aufnahme korrelierte signifikant mit pharmakokinetischen Modell-Parametern. Eine weiterführende Charakterisierung von MS-Läsionen anhand von Textur- oder Form-Parametern könnte beispielsweise eine nicht-invasive Unterscheidung zwischen fokalen MS- und diffusen Läsionen der progressiven multifokalen Leukenzephalopathie (PML) ermöglichen.

In der zweiten Studie wurde Voxel-weise parametrische Information aus dynamischen ^{18}F-FET (Aminosäure) PET-Bildern für eine nicht-invasive Gliom-Einstufung

genutzt. Die Fähigkeit molekulargenetische und histologische Gliom-Grade zu unterscheiden wurde für verschiedene Intensitäts-, Histogramm-, Form-, und pharmakokinetische Modell-Parameter beurteilt. In univariater Analyse konnte die höchste Genauigkeit für eine nicht-invasive Klassifizierung durch eine Quantifizierung der Parameterverteilung anhand von prozentualen Volumen-Anteil-Histogrammen (PVH) erreicht werden. Für die pharmakokinetischen Modell-Parameter wurden die signifikantesten Unterschiede zwischen den Tumor-Graden für die Transferraten K_1 und k_2 aus einem 1-Gewebe Kompartiment-Modell mit Blutvolumen-Anteil (1TC-V_B), k_4 aus einem 2TC4k-V_B Modell und für Parameter aus Patlak-Plots festgestellt. Es konnte gezeigt werden, dass z.B. statische und kinetische Parameter-Bilder komplementäre Information liefern, und somit eine Identifizierung von aggressiven Sub-Volumina und von Tumor-Heterogenität ermöglichen.

Die vorgestellten Ergebnisse sind vielversprechend, und bilden die Basis für zukünftige Anwendungen in der klinischen Routine, zur Verbesserung der Effizienz und Genauigkeit diagnostischer Verfahren. Die nächsten Schritte sollten eine Validierung bei Verdacht auf Tumor-Heterogenität durch Entnehmen stereotaktischer Biopsien beinhalten. Dies könnte eine Anwendung multi-parametrischer und multi-modaler Information für eine Voxel-weise Klassifikation, oder eine Schätzung von Wahrscheinlichkeits-Bildern welche z.B. einen Krankheits-Progress oder ein Rezidiv auf Voxel-Basis vorhersagen, ermöglichen.

Chapter 1

Introduction

Medical imaging has proven to be indispensable in clinical routine. This includes an application for diagnostic purposes, treatment planning and monitoring, or the prediction of disease progression. Besides **morphological** information, it is often desirable to retrieve information on **physiological or biochemical** processes. This can be achieved by the intravenous injection of a pharmaceutical, where a so-called **carrier** molecule is selected to monitor a specific process of interest. For diagnostic purposes such a pharmaceutical is often referred to as "tracer" or "contrast agent".

In nuclear medicine the **spatial and temporal distribution (biodistribution)** of a pharmaceutical within the body is "traced" with a so-called **radio-pharmaceutical**, where the carrier is labelled with a radionuclide. Images of gamma-emitting radioisotopes can be acquired with a gamma (or scintillation) camera. 3-dimensional gamma camera imaging is called **single photon emission computed tomography (SPECT)**. To be able to deduce the decay position within tissue, SPECT imaging relies on the application of a collimator placed in front of the photon detection crystals, which confines the solid angle of incident photons. Positron emitting radioisotopes have the advantage that positron annihilation is followed by the emission of two photons, which are emitted approximately in opposite directions (co-linear). This is utilised in **positron emission tomography (PET)** to estimate the decay position from the respective **line of response (LOR)**, without requiring an absorbing collimator. Therefore, PET is more sensitive and yields more uniform images with a higher resolution than SPECT for clinical imaging.

Besides the usage for diagnostic purposes in oncology, cardiology, or neurology, in-vivo targeting with radio-pharmaceuticals is also applied for targeted radionuclide therapy including the assessment of delivered dose. Among others, a pharmaceutical can for example mimic a metabolic substrate (e. g. glucose), specifically target receptors (e. g. dopamine, benzodiazepine, serotonin, somatostatin, and others), amino acid transporters, antigens, or translocator proteins (TSPO) [1–3]. Ideally such a radio-pharmaceutical should be **metabolically stable**, provide a **high specific binding**, and a low unspecific binding affinity. Also, the **availability** at the location of the molecular target may become relevant, as it is the case e. g. for targets within the brain, where the radio-pharmaceutical needs to cross the blood-brain-barrier (BBB, see section 2.4.4).

Structure of this thesis

In this work first a summary on the essential methodological aspects for quantification of brain PET images (chapter 2) is given. This includes basic principles of PET imaging (section 2.1), quantification of physiological or biochemical properties (section 2.2), and advanced image processing and analysis including voxel-based feature extraction (section 2.3).

The study section (chapter 3) starts with preliminary phantom measurements, aiming to establish and evaluate various threshold-based segmentation methods utilised for the delineation of focal MS or glioma lesions. This is followed by two studies showing the described methodological challenges arising for brain PET imaging, and aiming to enable a clinical assessment of pathologies of the central nervous system.

Chapter 2

Background

2.1 Basic principles of positron emission tomography

In this chapter the basic principles of nuclear physics are summarised for imaging with positron emission tomography. A detailed description on the respective aspects of nuclear physics can be found in [4–6].

2.1.1 Radioactive decay

The spontaneous radioactive decay of an unstable nuclide can be described as an exothermic process where either mass is converted into **binding energy** (E_{bin}) in order to maximise the binding energy per nucleon, or excess energy is released by gamma ray emission. The so-called **mass defect** (Δm) describes the phenomenon, that the mass of a nucleus composed of protons and neutrons is smaller than the mass of the separate nucleons. Due to the short-range nuclear force the aggregation of nucleons can be energetically favourable. The released binding energy corresponds to the mass defect (equivalence of mass and energy):

$$E_{bin} = \Delta m \cdot c^2 = [Z \cdot m_p + N \cdot m_n - m(Z, N)] \cdot c^2 \ , \tag{2.1}$$

where c is the speed of light, Z the atomic or proton number, and N the neutron number. The binding energy is described semi-empirically by the **Bethe-Weizsäcker mass formula**. This means, that mathematical assumptions are derived from a simplified model description of the nucleus (liquid drop model) and used to fit a model to experimentally determined binding energies:

$$E_{bin} = a_v \cdot A - a_s \cdot A^{2/3} - a_C \cdot \frac{Z^2}{A^{1/3}} - a_a \cdot \frac{(A - 2Z)^2}{A} + \begin{cases} +a_p \cdot A^{-1} & \text{Z, N even} \\ 0 & \text{A odd} \\ -a_p \cdot A^{-1} & \text{Z, N odd} \end{cases} , \tag{2.2}$$

where the parameters a_i with $i \in \{v, s, C, a, p\}$ quantify the contribution of each term to the binding energy, and $A = Z + N$ is the nucleon or mass number.

- Volume (a_v): The short-range nuclear force is a secondary effect of the strong force between quarks. For a better understanding, this can be compared to the hydrogen bridge bond between neutral water molecules, which is a secondary effect of the coulomb force. Due to the short range each nucleon they only interact with the nearest neighbours.

- Surface (a_s): The binding of nucleons at the surface is reduced due to a lower number of neighbouring nucleons. This effect is comparable to the surface tension effect of liquids.

- Coulomb (a_C): The coulomb repulsion of protons reduces the binding energy. Therefore, stable nuclides with a high mass number are constituted of a higher fraction of neutrons than protons.

- Asymmetry (a_a): The Pauli exclusion principle states that identical fermions cannot occupy the same quantum state simultaneously. Thus, additional fermions occupy higher energy levels (with a lower binding energy). Therefore, the same number of protons and neutrons is energetically favourable, if coulomb interaction is neglected.

- Pairing (a_p): The last term takes into account spin coupling of particle pairs. Hence, an even Z or N is preferred compared to an odd Z or N.

Unstable nuclides with too many neutrons are called n-unstable and tend to undergo $\boldsymbol{\beta^-}$ **decay**. Nuclides with too many protons (p-unstable) undergo $\boldsymbol{\beta^+}$ **decay** or electron capture (EC). For a very high mass number α decay or spontaneous fission can occur due to the increased influence of the coulomb term.

2.1.2   Statistical description of radioactive decay

Radioactive decay of statistically independent nuclides can be described as a Bernoulli process (binomial probability distribution). Under the assumption that the number of mother nuclides (N) is large compared to the number of decay events ($dZ = -dN$), the total number of decays (Z) in a given time interval can be drawn from a Poisson distribution

$$P(Z) = \frac{\bar{Z}^Z}{Z!} \cdot e^{-\bar{Z}} \ , \tag{2.3}$$

where $\bar{Z}$ is the average number of decays. For a large Z this can be approximated by a symmetrical Gaussian distribution $\mathcal{N}(\mu = \bar{Z}, \sigma = \sqrt{\bar{Z}})$. However, both is only an approximation of the underlying binomial distribution, and the applicability should be validated for each purpose [7].

The average decay rate (in the following denoted without bars) is proportional to the number of present mother nuclides:

$$\frac{dZ(t)}{dt} = -\frac{dN(t)}{dt} = \lambda \cdot N(t) \ , \tag{2.4}$$

where the proportionality factor is the **decay constant $\boldsymbol{\lambda}$**. This equation can be solved with an exponential law

$$N(t) = N_0 \cdot e^{-\lambda t} \ , \tag{2.5}$$

with radionuclide **half-life $\boldsymbol{T_{1/2}}$**, i.e. $N(t = T_{1/2}) = N_0/2$:

$$T_{1/2} = \frac{ln(2)}{\lambda}. \tag{2.6}$$

The **activity $A(t)$** is defined as:

$$
\begin{aligned}
A(t) &= \frac{dZ(t)}{dt} \\
&= -\frac{dN(t)}{dt} = \lambda N(t) = \lambda N_0 \cdot e^{-\lambda t} \\
&= A_0 \cdot e^{-\lambda t} \ .
\end{aligned}
\tag{2.7}
$$

2.1.3 Positron emission tomography

β decay processes are **isobar transitions**, i.e. the mother and daughter nuclides have the same mass number A. During β^+ decay, which is utilised for PET imaging, a proton is transformed into a neutron, a positron (e^+), and – to preserve lepton number – an electron neutrino (ν_e):

$$
{}^A_Z X \rightarrow {}^A_{Z-1} \tilde{X} + e^+ + \nu_e \ .
\tag{2.8}
$$

Due to the created positron and the higher neutron mass, the released binding energy must equal at least twice the electron mass (m_e). As a consequence, p-unstable nuclides with a transition energy lower than 2×511 keV = 1022 can only decay by electron capture (EC). The remaining excess energy released during β^+ decay is distributed as kinetic energy among the decay products. This results in a continuous e^+ energy spectrum, which is characteristic for the decaying radionuclide. A short excerpt of radionuclides applied for imaging with PET is given in table 2.1, showing the respective mean energies and ranges. The most frequently applied radionuclide for PET imaging is fluorine-18 (^{18}F), which has a relatively long half-life, a short positron range, and can be deployed as a hydrogen substitute.

Radio-nuclide	Half-life (min)	Decay modes (%)	$E_{e+,mean}$ (keV)	$R_{e+,max}$ (mm)	$R_{e+,mean}$ (mm)
^{18}F	109.7	β^+(97), EC(3)	252	2.6	0.7
^{11}C	20.4	β^+(100)	390	4.5	1.3
^{13}N	10.0	β^+(100)	488	5.6	1.7
^{15}O	2.0	β^+(100)	730	9.1	3.0
^{68}Ga	67.7	β^+(89), EC(11)	844	10.3	3.6
^{82}Rb	1.3	β^+(95), EC(5)	1551	18.6	7.5

Table 2.1: Characteristics of exemplary positron emitting radionuclides used in PET imaging: half-lifes, decay modes, mean energy ($E_{e+,mean}$), maximal ($R_{e+,max}$) and mean range ($R_{e+,mean}$) of emitted positrons in water [8, 9].
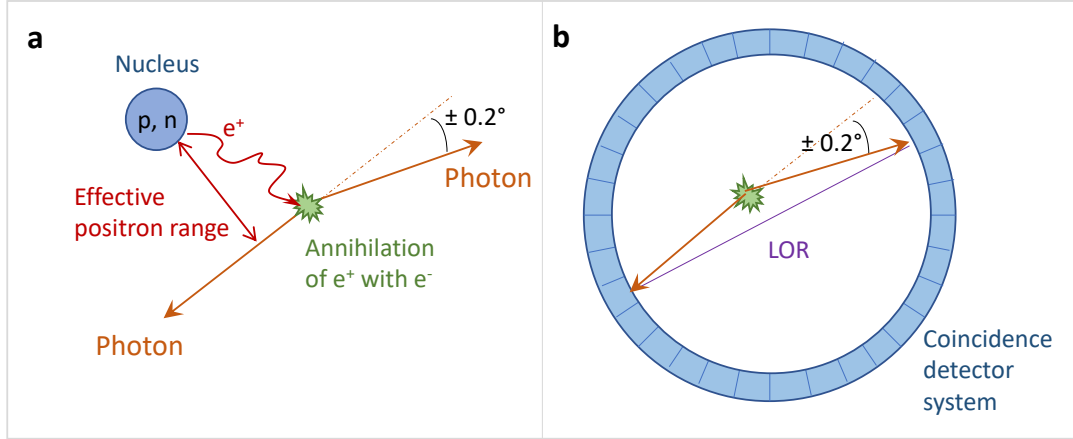
Figure 2.1: **a**: β^+ decay followed by positron annihilation and an approximately co-linear emission of two photons. **b**: Coincidence detection by a detector pair and estimated line of response (LOR).

The positron slows down in tissue due to elastic scattering, ionisation, or excitation processes. After the positron is slowed down in tissue, it either undergoes directly free **annihilation** with a bound electron, or first combines with an electron and builds a hydrogen like bound state called **positronium**. In most cases the positronium then annihilates by co-linear two-photon (2×511 keV) emission. The connection line between two detection points is defined as the **line of response (LOR)** (figure 2.1). The probability of positron annihilation increases for low energies. Positron annihilation at rest results in a co-linear photon emission in opposite directions. Due to momentum conservation residual kinetic energy can cause small angle deviations of about 0.2 degrees [10].

When two detectors measure incident photons within a specified **coincidence time window** and photopeak energy window, it is assumed that the two photons originate from the same annihilation process. However, the detected coincidences can include true, random, scattered, and multiple events. An encompassing summary on different types of events and correction approaches is e. g. given by Leahy and Qi [11].

The activity concentration f_k within voxel $k = 1, ..., K$ is measured by coincidence detection of detector pairs $d = 1, ..., D$. The measured **projection data y_d** originating from the LOR defined by detection pair d, can be mathematically described by the application of a forward projection matrix, the so-called **system matrix** H_{dk}:

$$y_d = \sum_{k=1}^{K} H_{dk} \cdot f_k + b_d \ , \tag{2.9}$$

where the scattered and random fractions are inserted as an additive error term $b_d = b_{d,sc} + b_{d,ra}$. The system matrix H_{dk} includes all relevant (image degrading) processes affecting the measurement of true events: positron range, scanner geometry, attenuation within tissue, detector blur, and sensitivity (matrix application order from right to left) [11]:

$$H = H_{\text{sensitivity}} \cdot H_{\text{blur}} \cdot H_{\text{attenuation}} \cdot H_{\text{geometry}} \cdot H_{\text{positron}} \ . \tag{2.10}$$

Further corrections which can be applied include e. g. decay and motion correction. Attenuation correction is ideally performed based on measured transmission data.

2.1.4 Tomographic image reconstruction

A straight forward analytical 2D image reconstruction can be performed by simply back-projecting the measured y_d with **filtered back-projection (FBP)**. In order to enable the restoration of sharp object boundaries, additional filters have to be applied on projection data before backprojection. Advantages of FBP reconstruction are the simplicity and efficiency. However, it is not possible to incorporate a model of image degrading factors or statistical noise.

Therefore, iterative image reconstruction has been implemented. This procedure aims to find the most probable image estimate $\hat{f}$, i.e. maximising the probability to obtain the measured projections y_d. Assuming that the measured y_d are Poisson distributed (section 2.1.2), the likelihood function can be written as

$$L(f) = P(y|f) = \prod_d e^{-\bar{y}_d} \cdot \frac{(\bar{y}_d)^{y_d}}{y_d!} \ , \tag{2.11}$$

with $\bar{y}_d = \sum_k H_{dk} f_k + b_d$ (from equation (2.9)). The maximum likelihood estimate can be derived by maximising the monotonically increasing log-likelihood function $l(f) = \ln L(f)$, i.e. by solving $\frac{\partial \ln L(f)}{\partial f} = 0$ with fixed point iteration. This yields the following **maximum likelihood expectation maximisation (MLEM)** equation for iterative reconstruction [11, 12]:

$$\hat{f}_k^{n+1} = \frac{\hat{f}_k^n}{\sum_{d'} H_{kd'}} \cdot \left[\sum_d H_{kd} \cdot \left(\frac{y_d}{\sum_k H_{dk} \hat{f}_k^n + b_d} \right) \right] \ . \tag{2.12}$$

This iteration equation provides positive image estimates in case of a non-negative initial estimate $f_d^0 > 0$. Moreover, iterative reconstruction provides better noise properties than FBP (higher signal-to-noise ratio, SNR), especially for low activities. For an accelerated convergence of the procedure **ordered subsets EM (OSEM)** was introduced, where each iteration step is applied on a varying subset of the data [13].

2.1.5 System point spread function

In general the term **partial volume effect (PVE)** relates to image degradation due to two different phenomena: (1) a finite image resolution depending on the **point spread function (PSF)** of the imaging system resulting in a so-called **spill-in and spill-out** of activity with respect to a target region, and (2) a simple sampling effect due to a finite voxel size of the images, which becomes relevant when different tissue types are enclosed within one voxel [14–16]. The width and shape of the system PSF depends on the image degrading processes described in section 2.1.3. Attarwala *et al.* [17] found that the PSF is best described by three 3-dimensional Gaussian functions, which further underlines the influence from multiple processes.

For simplicity reasons it is assumed here, that the PSF is spatially invariant and independent of the activity distribution $f(r)$ (linear system). Hence, the measured image $g(r)$ can be described as a convolution of object $f(r)$ with the PSF and an error term $n(r)$ (assumed to be additive):

$$g(r) = f(r) \circledast \mathrm{PSF}(r) + n(r). \tag{2.13}$$

A simple deconvolution can be performed using the Fourier transformation (FT) operation $\mathrm{FT}(f(r)) = F(u) = \int_{\mathbb{R}} f(r) \cdot e^{-2\pi i u r} dr$, with spatial frequency u. The PSF in

frequency domain is called **modulation transfer function (MTF)**. FT applied to equation (2.13) gives

$$G(u) = F(u) \cdot \text{MTF}(u) + N(u) \ . \tag{2.14}$$

By a simple rearrangement of equation (2.14), and a subsequent transformation back into the spatial domain, the deconvolution can be expressed as

$$f(r) = \int_{\mathbb{R}} \frac{G(u) - N(u)}{\text{MTF}(u)} \cdot e^{2\pi i u} du \ . \tag{2.15}$$

Unfortunately, for a decreasing $\text{MTF}(u)$ at high spatial frequencies u the noise term becomes dominant. Therefore, several other deconvolution methods have been developed [18, 19]. This includes methods directly applied during reconstruction, and methods applied post reconstruction. During iterative image reconstruction the system PSF can be incorporated in the system matrix, which simultaneously can improve noise properties, but causes Gibbs artefacts at object boundaries (corresponding to high spatial frequencies, where the system MTF is zero), and yields unreliable quantification for small lesions [20]. Post reconstruction methods have to deal among others with the described noise-amplification issue [21–23].

2.2 Quantification of tracer pharmacokinetics

The gold standard for evaluation of physiological and biochemical processes from dynamic PET data is **compartmental modelling**. This relies (1) on invasive continuous arterial blood sampling and a subsequent determination of free parent in plasma fraction, and (2) on non-linear regression with multiple fitting parameters. Non-linear fitting minimising an objective function (e. g. least squares) may provide several local minima and not an explicit solution, and is not time-efficient in case of a voxel-wise estimation of parametric maps [24, 25].

For the determination of inter- and intra-patient comparable macro-parameters it is in general desirable to provide a less extensive, but still reliable, and robust method. This was for example achieved by **graphical analysis (GA)** aiming to linearise the model equations in order to apply linear regression [26–29]. GA has the further advantage that no a priori knowledge on the exact compartmental model is required (data-driven). Yet, the main drawback remains the need for arterial blood sampling. As a consequence several approaches have been proposed using image-derived information [30–32].

The first section of this chapter summarises the basic principles of compartmental modelling and discusses the determination of an arterial input function. This is followed by an introduction to graphical analysis and reference tissue modelling. The last section of this chapter deals with quantification based on heuristic parameters.

2.2.1 Compartmental modelling of specific and non-specific binding

Compartmental models are introduced in order to provide a suitable description of physiological and biochemical processes by quantifying the spatial and temporal distribution of a radio-pharmaceutical within the body, i. e. the time-dependent **delivery**, **retention**, and **clearance** of tracer after intravenous injection [33]. In such models the spatial (e. g. different organs, tissues, or vessels) and biochemical state (e. g. parent, metabolised, specifically bound, or trapped compound) of the tracer is represented by separated **compartments** i, and the temporal change of the respective tracer concentration $C_i(t)$ is quantified by **transfer rates** (first-order rate constants) for tracer influx k_{ij} from, and efflux k_{ji} to compartment j:

$$\frac{d}{dt}C_i(t) = \sum_{j \neq i; j=1}^{N} \left[k_{ij} \cdot C_j(t) - k_{ji} \cdot C_i(t) \right] , \qquad (2.16)$$

where N is the number of compartments considered in the pharmacokinetic model [34]. The applicability of such models relies on the following assumptions [35]: (1) the injected amount of tracer is low enough to have no influence on the physiologic and molecular processes of interest, which (2) are assumed to be constant during the scan time; (3) tracer concentration is homogeneously distributed (instantaneous mixing) within the distinct compartments.

Since tracer is injected intravenously, it is important to include an plasma **input function (IF)** compartment, representing the tracer delivery to a tissue of interest from arterial plasma $C_P(t)$. Integration of equation (2.16) and subsequent summation over all compartments i yields a model representation for the total tissue concentration $C_T(t)$, which can be expressed for linear compartmental systems in terms of a convolution of

the plasma input function with an **impulse response function (IRF)** [36]:

$$
\begin{aligned}
C_T(t) &= C_P(t) \circledast \mathrm{IRF}(t) \\
&= \int_0^t C_P(\tau) \cdot \mathrm{IRF}(t - \tau) d\tau \\
\mathrm{IRF}(t) &= \sum_{i=1}^{N-1} \phi_i \cdot e^{-\theta_i t} \ ,
\end{aligned}
\tag{2.17}
$$

where ϕ_i and θ_i are functions of the transfer rate constants, and $N - 1$ is the number of tissue compartments (excluding the arterial plasma compartment). In general, not only different tissue compartments, but blood vessels themselves can be present within the assessed tissue volume. The fractional blood volume V_B, and the whole blood concentration C_B can be included in equation (2.16) [36]:

$$
C_T(t) = V_B \cdot C_B(t) + (1 - V_B) \cdot C_P(t) \circledast \mathrm{IRF}(t) \ .
\tag{2.18}
$$

For models with only few compartments, the transfer rates in equation (2.16) are indexed with numbers, e. g. K_1 is the **transfer rate from blood to tissue** (clearance, $K_1 = \sum_{i=1}^{N-1} \phi_i$ [36]), and k_2 the transfer rate from tissue to blood. If the efflux transfer rate is negligible for at least one compartment, the model is called **irreversible**. This assumption can also be applied for PET radio-pharmaceuticals with very slow reversible binding kinetics, i. e. showing an continuously increasing kinetic without washout within the scanning time-window [37].

Model selection

In case of new radio-pharmaceuticals, the capability of different models to appropriately describe the measured data needs to be assessed. A summary on common compartmental **model selection** criteria which quantify the goodness of fit can be found in [38,39]. The optimisation algorithm itself, the chosen weighting method, parameter constraints, and in case of voxel-wise fitting the noise reduction strategies are of high importance [40,41].

For example, compartmental models are frequently compared using the **corrected Akaike information criterion (AIC$_C$)**, which is suitable in case of a high number of parameters p compared to the sample size n ($n/p \leq 40$) [39,42]:

$$
\mathrm{AIC}_C = n \cdot \ln\left(\mathrm{WRSS}\right) + 2 \cdot p + \frac{2 \cdot p \cdot (p + 1)}{n - p - 1} \ ,
\tag{2.19}
$$

where **WRSS** is the **weighted residual sum of squares** defined as the sum over the squared errors, i. e. the differences between measured activity concentrations C_f in frames f and the fitted values $\tilde{C}_f$:

$$
\mathrm{WRSS} = \sum_f w_f \cdot (C_f - \tilde{C}_f)^2.
\tag{2.20}
$$

General compartmental model considerations

In a simplified tracer model (figure 2.2, V_B neglected), total tissue concentration $C_T(t)$ can be interpreted as a combination of specifically (S) and non-specifically (NS) bound tracer, and of tracer freely (F) available in tissue:

$$
C_T(t) = C_S(t) + C_{NS}(t) + C_F(t).
\tag{2.21}
$$

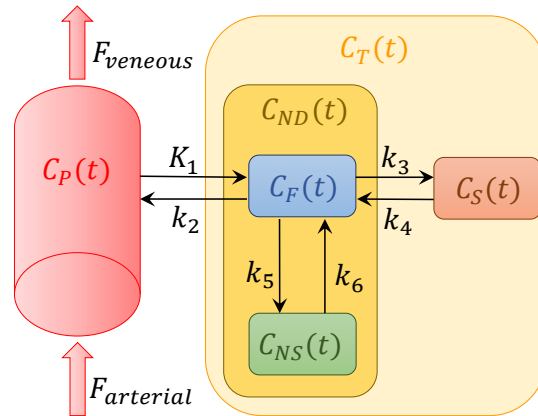**Non-displaceable (ND)** tracer concentration is defined as: $C_{ND}(t) = C_{NS}(t) + C_F(t)$ [43, 44].

Figure 2.2: Schematic illustration of a 3-tissue compartment (3TC) model incorporating concentrations of plasma input $C_P(t)$, free tracer in tissue $C_F(t)$, non-specific $C_{NS}(t)$ and specific binding $C_S(t)$. $C_F(t)$ and $C_{NS}(t)$ can be merged to one non-displaceable compartment with $C_{ND}(t)$, yielding a 2TC model. In a 1TC model no tissue compartments are differentiated.

Perfusion and extraction fraction

Several physiological parameters are relevant for the exchange of tracer between blood plasma and brain tissue across the blood-brain barrier. While blood flow is defined as the blood volume delivered per unit of time (units $\mathrm{mL} \cdot \mathrm{min}^{-1}$), **perfusion ($F$)** is defined as the volume of blood delivered per unit of tissue mass and time (units $\mathrm{mL} \cdot \mathrm{g}^{-1} \cdot \mathrm{min}^{-1}$) [5, 44]. The product of permeability (P) (units $\mathrm{cm} \cdot \mathrm{min}^{-1}$) and available surface area (S) per unit of tissue volume (units $\mathrm{cm}^2 \cdot \mathrm{g}^{-1}$) is called the **permeability surface area product (PS**, units $\mathrm{mL} \cdot \mathrm{g}^{-1} \cdot \mathrm{min}^{-1}$). From the PS the (unitless) **extraction fraction E** can be derived, which quantifies the fraction of tracer transferred from blood to tissue during first pass through the capillary (unidirectional). In the Renkin-Crone model a capillary is assumed to be a rigid cylindrical tube [45, 46], yielding

$$E = 1 - e^{-\frac{PS}{F}} , \tag{2.22}$$

i. e. E increases with PS and decreases with F. With this the transfer rate from blood to tissue can be expressed as the product of perfusion and extraction fraction:

$$K_1 = F \cdot E , \tag{2.23}$$

which increases with perfusion F for higher PS values [35].

Equilibrium condition and quantification with macro-parameters

Since relative tracer concentrations vary over time, a robust quantification can only be achieved under the condition of a **true equilibrium**. This is reached, when the steady state condition for blood ($\frac{dC_P(t)}{dt} \approx 0$) and tissue ($\frac{dC_T(t)}{dt} \approx 0$) is fulfilled over a period of time, similar to le Chatelier's principle for chemical reactions. This should not

be confused with the peak of tissue tracer concentration after bolus injection. Under the idealised assumption of a closed system, true equilibrium can be approximated by constant tracer infusion [47, 48]. Tissue uptake C_T of reversible tracers at equilibrium relative to plasma concentration C_P is quantified by introducing the concept of **volume of distribution (V_T)**:

$$V_T = \frac{C_T}{C_P} \ . \tag{2.24}$$

Specific uptake $C_S = C_T - C_{ND}$ at equilibrium relative to a chosen reference concentration C_X is defined as **binding potential (BP)**: $\text{BP}_X = \frac{C_S}{C_X} = \frac{C_T - C_{ND}}{C_X}$. For example specific uptake relative to plasma concentration C_P yields $\text{BP}_P = \frac{C_T - C_{ND}}{C_P} = V_T - V_{ND} = V_S$ and relative to non-displaceable uptake C_{ND} [44] yields

$$\text{BP}_{ND} = \frac{C_T - C_{ND}}{C_{ND}} \ . \tag{2.25}$$

V_T and BP_{ND} can either be obtained by performing a continuous infusion protocol, or in case of a single bolus injection by performing kinetic modelling. For a compartmental model defined according to equation (2.17), V_T can be calculated as [24, 36]:

$$V_T = \int_0^\infty \text{IRF}(t)dt = \sum_{i=1}^{N-1} \frac{\phi_i}{\theta_i} \ . \tag{2.26}$$

In case of irreversibly binding tracers equilibrium condition cannot be reached for the entire tissue, and the above mentioned macro-parameters V_T, and BP_{ND} are not applicable. Irreversible tracer kinetics are described instead by a **net influx rate K_i** from plasma into the irreversible compartment n ($\theta_n = 0$ in equation (2.17)) [36]:

$$K_i = \lim_{t \to \infty} \text{IRF}(t) = \phi_n \ . \tag{2.27}$$

For bolus injection of reversibly binding radio-pharmaceuticals only a **pseudo- (or relative) equilibrium** can be reached, which is defined as a state during which the ratio of tissue and plasma concentration is constant over time: $\frac{C_T(t)}{C_P(t)} \approx const$. This constant ratio is referred to as apparent volume of distribution, and does not correspond to V_T at true equilibrium [35].

One- and two-tissue compartment models

PET tracers intended to measure perfusion (no specific binding) can be modelled by an **1-tissue compartment (1TC)** model. Setting $N = 2$ in equations (2.16) and (2.17) yields:

$$\frac{d}{dt}C_T(t) = K_1 \cdot C_P(t) - k_2 \cdot C_T(t) \ ,$$
$$C_T(t) = C_P(t) \circledast K_1 e^{-k_2 t} \ , \tag{2.28}$$
$$\text{and } V_T = \frac{K_1}{k_2} \ .$$

The equation of a **2TC** model ($N = 3$ in equation (2.17)) is:

$$C_T(t) = C_P(t) \circledast \left[\phi_1 \cdot e^{-\theta_1 t} + \phi_2 \cdot e^{-\theta_2 t} \right] \ , \tag{2.29}$$

with $\phi_{1,2}$ and $\theta_{1,2}$ as specified in [37] this yields the macro-parameters of reversible binding

$$V_T = V_{ND} \cdot (1 + \text{BP}_{ND}) \; ,$$

$$\text{with } V_{ND} = \frac{K_1}{k_2} \text{ and } \text{BP}_{ND} = \frac{k_3}{k_4} \; , \tag{2.30}$$

and of irreversible binding ($k_4 = 0$)

$$K_i = \phi_2 = \frac{K_1 \cdot k_3}{k_2 + k_3} \; . \tag{2.31}$$

Input function determination

The input function $C_P(t)$ for compartmental modelling should represent free unmetabolised tracer concentration in blood plasma. Hence, not only a continuous measurement of arterial blood activity concentration $C_B(t)$ is required, but also the determination of free parent fraction in plasma for several discrete time points. Separation of plasma from blood cells is generally performed by centrifugation, yielding a **plasma-to-blood ratio (f_{pwb})**. For extraction of **plasma parent fraction (f_{ppf})**, the most common procedure is to perform high-pressure liquid chromatography (HPLC) on plasma samples, followed by fitting a mathematical function to the discrete data [49]. Lastly, the **plasma free fraction (f_p)** can be determined, in order to exclude the fraction of tracer non-specifically bound to plasma proteins. Typically, it is assumed that f_p is constant during the scan time. However, f_p measurements (e.g. with ultrafiltration) have a high level of uncertainty [50]. Therefore, f_p is often neglected. Nevertheless, knowledge on f_p can support the understanding of new tracer properties. Moreover, the measurement of $C_B(t)$ with a **continuous blood sampler** [51,52] itself can be prone to errors, originating from noise in measured data and tubing effects (e.g. clotting, sticking to tube walls for lipophilic tracers) [53,54].

Despite the susceptibility to methodological errors, high cost, and patient discomfort, the gold standard for quantification of physiologic processes remains the extraction of $C_P(t)$ from blood samples. For parent fraction estimation of metabolically unstable tracers, it is inevitable to draw a few blood samples. Nevertheless, it is desirable to replace the invasive and time-consuming continuous blood sampling by other methods. For example $C_B(t)$ can be directly estimated from PET images [31,32,53,55–57], measured e.g. with non-invasive wrist detectors [58–60], or derived based on a rescaled **population-based standard IF** [61,62]. The reliability and applicability of an **image-derived input function (IDIF)** has shown to be tracer specific, and dependent on image quality (correction for partial volume effects), i.e. the ability to recover signal over a large range of activity concentrations within arteries or blood pools of varying size [53,57,63].

2.2.2 Graphical analysis

Compartmental modelling relies on non-linear fitting and prior knowledge on the model structure. The high computational cost and sensitivity to initial estimates becomes especially important in case of fitting noisy time-activity curves (TACs) of single voxels [25]. In most cases the macro-parameters described in section 2.2.1 are of interest, which are independent of a specific compartmental configuration. Hence, so-called graphical

analysis (GA) methods aim to estimate the macro-parameters using simplified linear regression analysis [64, 65].

The linear relation is basically obtained by assuming a pseudo-equilibrium condition (see section 2.2.1) for times $t > t^*$ for all reversible compartments, and by rearranging the model equation (2.16). For irreversibly binding tracers Patlak *et al.* [26, 66] proposed the following linear equation for estimation of the net uptake rate K_i with **Patlak plot**:

$$\frac{C_T(t)}{C_P(t)} = K_i \cdot \frac{\int_0^t C_P(\tau)d\tau}{C_P(t)} + Int \ . \tag{2.32}$$

Logan *et al.* [28] introduced a method to estimate distribution volumes for reversible tracers with **Logan plot**:

$$\frac{\int_0^t C_T(\tau)d\tau}{C_T(t)} = V_T \cdot \frac{\int_0^t C_P(\tau)d\tau}{C_T(t)} + Int \ . \tag{2.33}$$

The Logan plot has the disadvantage that V_T estimates are sensitive to noise in $C_T(t)$ data, especially for high specific binding regions in which the pseudo-equilibrium condition can be violated. This results in an underestimation of V_T in regions with high specific binding [67, 68]. This issue was approached by several groups [29, 69, 70]. For example Zhou *et al.* [68, 70] validated the performance of a new linear equation termed **relative equilibrium-based (RE) plot**,

$$\frac{\int_0^t C_T(\tau)d\tau}{C_P(t)} = V_T \cdot \frac{\int_0^t C_P(\tau)d\tau}{C_P(t)} + Int \ , \tag{2.34}$$

and a combined application of RE plot and Patlak plot called RE-GP plot [68].

2.2.3   Reference tissue modelling

The GA methods described in section 2.2.2 still rely on the availability of an arterial plasma input function. In addition to alternative methods for the extraction of an IDIF (section 2.2.1), image-derived reference tissue TACs may be applied as an input function and surrogate for non-displaceable tracer uptake. The main requirements which an ideal reference tissue (RT) should fulfil are: (1) RT should be devoid of specific uptake (i. e. BP'$_{ND}$ = 0), (2) V'_{ND} in the RT should be similar to V_{ND} in the tissue of interest, and (3) uptake in the RT should not be influenced by the disease or treatment [71, 72]. By directly applying assumptions (1) and (2), tissue BP$_{ND}$ can be estimated for reversibly binding tracers (equation (2.25)) [73] with:

$$\begin{aligned} \mathrm{BP}_{apparent} &= \frac{V_T}{V'_T} - 1 \\ &= \frac{V_{ND} \cdot (1 + \mathrm{BP}_{ND})}{V'_{ND} \cdot (1 + \mathrm{BP}'_{ND})} - 1 \\ &\overset{(1),(2)}{\approx} \mathrm{BP}_{ND} \ . \end{aligned} \tag{2.35}$$

The ratio $\frac{V_T}{V'_T}$ is referred to as **distribution volume ratio (DVR)**. A comprehensive summary and comparison of several reference tissue methods including full reference tissue model, simplified, and multilinear approaches can be found in [74]. A discussion

on the influence of assumption violations for the simplified reference tissue model is provided by [75].

Macro-parameter estimation based on a reference tissue input function can be combined with graphical analysis as introduced in the previous section. The respective GA reference tissue model equations are [28, 65, 69, 76]:

$$\text{Patlak:} \qquad \frac{C_T(t)}{C_T'(t)} = \frac{K_i}{V_T'} \cdot \frac{\int_0^t C_T'(\tau)d\tau}{C_T'(t)} + Int \ ,$$

$$\text{Logan:} \qquad \frac{\int_0^t C_T(\tau)d\tau}{C_T(t)} = \text{DVR} \cdot \frac{\int_0^t C_T'(\tau)d\tau + C_T'(t)/\bar{k}_2'}{C_T(t)} + Int \ , \qquad (2.36)$$

$$\text{RE (Zhou):} \qquad \frac{\int_0^t C_T(\tau)d\tau}{C_T'(t)} = \text{DVR} \cdot \frac{\int_0^t C_T'(\tau)d\tau}{C_T'(t)} + Int \ ,$$

where k_2' in the Logan reference tissue model is approximated by the population average $\bar{k}_2'$, and is negligible in many cases [76].

2.2.4 Quantification based on heuristic parameters

Despite the huge amount of possible quantification methods estimating the macro-parameters described in section 2.2.1, extensive modelling is rarely applied in clinical routine. Due to obvious reasons such as patient comfort, clinical throughput and workload, it is desirable to assess disease status based on heuristic parameters derived from static images.

As delineated in section 2.2.1, concentration ratios derived under pseudo-equilibrium condition are quantitatively different from true V_T. Nevertheless, a (semi-) quantitative assessment with simple ratios (target tissue relative to an appropriate reference tissue) has shown relevance for various clinical applications. The goal of heuristic quantification is to provide sufficient and reliable information for disease assessment, with a high inter- and intra-patient comparability, without requiring an exact quantification of physiological and biochemical processes.

When no appropriate reference tissue is available, a normalisation of image values can also be based on known influences from confounding factors like injected activity and patient weight [77, 78]. The utilisation of (unitless) **standardised uptake values (SUV)** is still a widely used quantification procedure in clinical routine:

$$\text{SUV} = \frac{\text{activity concentration [kBq/mL]}}{\text{injected activity [MBq] / patient weight [kg]}} \ . \qquad (2.37)$$

For some clinical applications a heuristic description of time-activity curve (TAC) kinetics derived from dynamic PET data has been established [79]. This includes for example the time-to-peak (TTP), peak SUV (SUV_{peak}), area under the curve (AUC), and early or late TAC-slopes (figure 2.3). Furthermore, a normalisation of uptake values from static images to an appropriate reference tissue can be performed, yielding so-called SUV ratios (SUVR) or target-to-background ratios (TBR).
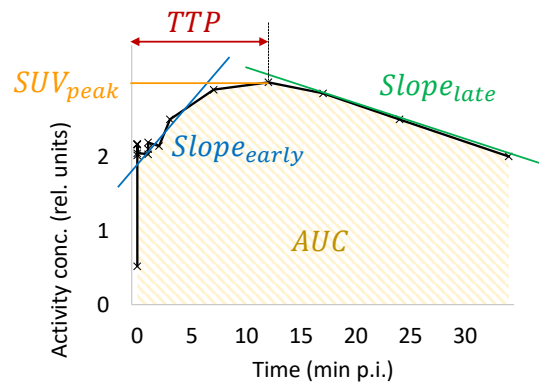
Figure 2.3: Illustration of some established heuristic parameters utilised for the characterisation of TAC kinetics.

2.3 Image processing and analysis

The goal of image processing is to enable and improve the correlation of PET information with disease classification, progression, and other clinically relevant parameters, or the identification of significant differences between groups. The most common methods for statistical analysis in functional brain imaging rely on the definition of a **volume of interest (VOI)**, from which average parameters can be derived. Segmentation of structures in medical images in general is of high interest resulting in a large number of publications trying to optimise methodology. In functional brain PET imaging either pronounced lesions with an elevated uptake can be segmented [80, 81], or certain brain regions of interest can be delineated based on additional information from e.g. morphological T_1-weighted magnetic resonance imaging (MRI) in combination with a pre-defined **probabilistic brain atlas** [82].

However, when imaging diffuse uptake variations in the brain without prior knowledge on the dissemination of disease, it can be helpful to perform statistical analysis on a **voxel basis**. This can be applied for the assessment of different kinds of central nervous system disorders, including e.g. epilepsy, infection, spinal cord injury, or neurodegenerative diseases such as Alzheimer's disease or multiple sclerosis.

In the following, several image processing methods, aiming to improve information content extracted from functional brain PET images, are presented. This includes methods optimising segmentation in functional brain images, probability atlas-based structural segmentation methods, voxel-wise analysis based on **statistical parametric maps (SPM)**, and a brief summary on methods for the characterisation of objects and intensity distributions with histogram analysis, texture analysis, and shape parameters.

2.3.1 Image segmentation methods

VOI-based quantification of lesions does not only depend on the quality of PET images (e.g. PVE), but also on the performance and reliability of the chosen segmentation algorithm. Besides volume-based quantification for diagnostic purposes, the estimation of 3-dimensional lesion extent is also essential for the definition of target volumes in radiation therapy. Hence, segmentation either aims to estimate true lesion volume (boundary reproducing), or to deliver real intensity estimates. In case of ideal images without noise, a delta-shaped space-invariant system PSF, and high resolution, a boundary reproducing volume segmentation would simultaneously deliver correct intensity values. However, the image degrading factors introduced in section 2.1.3 cannot be neglected. One approach to solve both tasks at once, is to either apply segmentation on images corrected for PVE, or to utilise boundary reproducing segments for a posteriori correction of PVE. For images reconstructed with PSF-based iterative algorithms, a threshold-based segmentation of volumes can be challenging due to uncontrolled amplification effects at object boundaries. This work will focus on the segmentation of realistic volumes, bearing in mind a possible application of techniques compensating the PVE.

Due to a high inter- and intra-operator variability, and dependency on the viewing conditions of colour bars etc., a manual segmentation in case of activity images is not advisable. Automatic segmentation of lesions in static activity concentration images can either be based on **fixed** or **iterative** [83–86] **thresholds**, or on **variational** techniques (e.g. level-sets, active contours, gradient-based watershed segmentation) [80, 81]. Strictly speaking, a purely threshold-based approach for segmentation in static PET

images is only valid under the following assumptions: (1) spherically shaped object, (2) homogeneous intensity distribution within the object, (3) isotropic and spatially constant system PSF. Consequently, for more complex shaped objects the application of variational methods might be favourable. Additionally, several advanced segmentation methods which are applicable to multi-parametric image datasets have been developed and partly applied on PET data, including data driven **clustering** [87] or **supervised classification** [88,89] methods algorithms.

2.3.2   Atlas-based segmentation with maximum probability maps

For a voxel-wise comparison of brain PET images, and for the application of anatomical atlas VOIs on functional PET data, a spatial transformation into a standard **template space** is useful. The two most common stereotactic template spaces for brain mapping are Talairach and MNI (Montreal Neurological Institute) space. For atlas-based segmentation the two following steps need to be performed: (1) deformable registration of the patient image to an image of the same modality in template space [90] and (2) segmentation based on atlas information. A summary on template spaces and brain atlases can be found in [82].

Due to a high inter-subject variability of anatomical brain structure, the concept of a **population-based probabilistic atlas** was developed, where a 3D brain structure is not represented by a single average atlas, but preserves information on inter-subject variability. Such a probabilistic map can be generated from a population of subjects, which are first mapped into a chosen stereotactic space and intensity normalised, then manually assigned to a tissue class. Finally, a probability map for each tissue class can be derived [91]. This probability maps can either be directly utilised by segmentation algorithms, or a so-called **maximum probability atlas** can be derived, where each voxel in template space is assigned to the most frequent label. Within the PMOD Neuro tool (PMOD Technologies, Zurich Switzerland), which was utilised in this work, the N30R83 maximum probability atlas for segmentation of T_1-weighted MRI images in MNI space is implemented and provides 83 brain structures [92,93].

2.3.3   Statistical parametric mapping

For the 3-dimensional characterisation of activation or deactivation in functional images in neurology, Friston *et al.* [94,95] introduced the concept of statistical parametric maps (SPMs), i.e. colour-coded distributions of statistical significance. The tests provided within the dedicated SPM software developed by the Wellcome Centre for Human Neuroimaging (University College London, UK) include for example **analysis of variance (ANOVA)**, correlation, or regression analysis. With the provided methodology images containing a disease related elevated or degraded uptake can be compared on a voxel basis to a set of healthy control images or to other patient images. Alternatively, e.g. a voxel-wise correlation with clinical parameters can be performed. Moreover, the possibility to incorporate **confounding nuisance variables** (frequently e.g. age and gender) is provided. Statistical tests assuming non-parametric variables are not incorporated in the SPM software, but have been addressed e.g. by Holmes *et al.* [96].

The frequently applied ANOVA either focuses on differences between subjects (only one image per subject, simple ANOVA), or on differences between **repeated measures** of the same subjects. This can include multiple experimental **factors** (different types of parameters, conditions) for each observed **level**. A level represents e.g. a patient or

healthy controls group, or different time points for repeated measures. For example a simple one-way (one factor) ANOVA with 2 levels is equivalent to the two-sample t-test, and a one-way within-subject ANOVA is equivalent to a paired t-test.

In the following section first the statistical methods relevant for SPM analysis are described at a single voxel level. Next a short introduction to cluster level inferences is given, incorporating spatial connectedness and the assumption of an expected cluster size.

Multivariate linear regression model

The **multivariate linear regression model (MLRM)** (also called general linear model) forms the basis of statistical analysis in SPM. Let $j = 1, ..., J$ be the scan number, and $l = 1, ..., L$ the number of covariates, confounding effects, or levels of ANOVA, then the **response variable** Y_j (dependent, regressand, or explained variable) can be expressed as a linear combination of **explanatory variables** x_{jl} (also called regressors, covariates, or independent variables forming a design matrix X), and an additive **error term** (disturbance, or noise) consisting of independent identically distributed random variables $\epsilon_j \overset{iid}{\propto} \mathcal{N}(0, \sigma^2)$ (Gaussian with zero mean and variance σ^2):

$$Y_j = \sum_{l=1}^{L} x_{jl} \cdot \beta_l + \epsilon_j \ . \tag{2.38}$$

For example the MLRM of linear regression can be formulated as $Y_j = \mu + x_j \cdot \beta + \epsilon_j$, where β is the regression slope and μ is a constant term.

Equation (2.38) has no explicit solution, due to the unknown error terms. Consequently, the parameters β_l need to be estimated, aiming to provide an optimal fit to the measured data. This can be achieved e. g. by minimising the sum of squared errors, i. e. the difference between experimentally determined observables Y_j and fitted values $\tilde{Y}_j = \sum_{l=1}^{L} x_{jl} \cdot \tilde{\beta}_l$:

$$S = \sum_{j=1}^{J} (Y_j - \sum_{l=1}^{L} x_{jl} \cdot \tilde{\beta}_l)^2 \ . \tag{2.39}$$

By solving $\frac{\partial S}{\partial \tilde{\beta}_l} = 0$, and assuming that $(X^T X)$ is invertible, the following ordinary least squares estimates $\hat{\beta}$ can be obtained:

$$\hat{\beta}_l = \left(\sum_{j=1}^{J} x_{lj} \cdot x_{jl} \right)^{-1} \sum_{j=1}^{J} x_{lj} \cdot Y_j \tag{2.40}$$

$$\text{or } \hat{\beta} = (X^T \cdot X)^{-1} \cdot X^T \cdot Y \ .$$

For the normally distributed parameter estimates $\hat{\beta} \propto \mathcal{N}(\beta, \sigma^2 \cdot (X^T \cdot X)^{-1})$ applies. Multiplication with a **contrast vector c** ($\sum_{l=1}^{L} c_l = 0$) yields $c^T \cdot \hat{\beta} \propto \mathcal{N}(c^T \cdot \beta, \sigma^2 \cdot c^T \cdot (X^T \cdot X)^{-1} \cdot c)$. Consequently, the test statistic T (**t-score**, Student's t-distribution) can be expressed as

$$T = \frac{c^T \cdot \hat{\beta} - c^T \cdot \beta}{\sqrt{\hat{\sigma}^2 \cdot c^T \cdot (X^T \cdot X)^{-1} \cdot c}} \ , \tag{2.41}$$

where the difference between estimated and measured data is normalised by the standard deviation $\hat{\sigma}$, resulting in a reduction of t-scores for high standard deviations.

Two-sample t-test

As an example, here the MLRM terminology is applied on a simple two-sample t-test between two independent groups (Y_{1j} and Y_{2j}), where the individual group effects are represented by the mean values μ_1 and μ_2. This can be expressed as a MLRM:

$$Y_{q,j} = x_{q,j1} \cdot \mu_1 + x_{q,j2} \cdot \mu_2 + \epsilon_{1,j} \ , \tag{2.42}$$

with $x_{q,jl} = \begin{cases} 1 \text{ if } q = 1 \\ 0 \text{ if } q = 2 \end{cases}$, $x_{2,j2} = \begin{cases} 0 \text{ if } q = 1 \\ 1 \text{ if } q = 2 \end{cases}$, and $\beta = [\mu_1, \mu_2]^T$. This yields $(X^T \cdot X) = \begin{pmatrix} n_1 & 0 \\ 0 & n_2 \end{pmatrix}$ and $(X^T \cdot X)^{-1} = \begin{pmatrix} 1/n_1 & 0 \\ 0 & 1/n_2 \end{pmatrix}$ with the number of measurements n_q in group q. The null hypothesis states that both groups have equal mean values $H_0 : \mu_1 = \mu_2$, which can be rewritten by means of a contrast vector $c = [1, -1]^T$ as $c^T \cdot \beta = 0$. Thus, we receive the formulation of the test statistic (equation (2.41)) of the two-sample t-test:

$$T = \frac{\hat{\mu}_1 - \hat{\mu}_2}{\sqrt{\hat{\sigma}^2 \cdot (1/n_1 + 1/n_2)}} \ . \tag{2.43}$$

Global normalisation

One major issue addressed by SPMs is the extraction of significant local changes independent of the global activity level. The global activity can be biased either due to instrumentation variability (such as injected activity or general scanner properties), or due to a subject specific biological and physiological body composition (e. g. patient weight).

The reduction of variability caused by a multiplicative effect can be achieved by normalisation (**proportional scaling**) of the image data. The global activity level is often estimated by the mean signal g_j within the entire brain (global mean),

$$g_j = \sum_{k=1}^{K} Y_j^k / K \ , \tag{2.44}$$

where $k = 1, ..., K$ enumerates the cerebral voxels, and Y_j^k is the intensity of voxel k in scan j. This is only adequate, if effect-related activity changes are negligible. Alternatively an appropriately chosen reference tissue fulfilling the criteria described in section 2.2.3 can be utilised, including the requirement that g_j needs to be independent of the process of interest. The adapted MLRM is:

$$Y_j^k = g_j \sum_{l=1}^{L} x_{jl} \cdot \beta_l^k + \epsilon_j'^k \ . \tag{2.45}$$

Alternatively, as proposed by Friston *et al.* [97], **analysis of covariance (AN-COVA)** can be utilised. Where a mean corrected global activity ($g_j - \bar{g}$) is incorporated as an additional regression term (**additive effect**) within the MLRM:

$$Y_j^k = \sum_{l=1}^{L} x_{jl} \cdot \beta_l^k + \xi^k \cdot (g_j - \bar{g}) + \epsilon_j^k \ . \tag{2.46}$$

Depending on the observed physiological process, the sensitivity of each voxel k to a global change can vary across the brain. This is incorporated in the MLRM by the subject-independent parameter ξ^k.

Classical inference

After calculating the test statistic of each voxel, a decision rule needs to be specified, i.e. a probability level below which the null hypothesis (H_0) can be discarded. The threshold is defined based on the null distribution of the test statistic, i.e. the probability distribution in case of a true null hypothesis. A threshold u then leads to a **false positive rate (FPR)** of $\alpha = p(t > u | H_0)$. In the case of e.g. $K = 100\,000$ voxels, an α-level of 0.05 leads to a large number (5 000) of false positive voxels (multi comparisons problem). A simple Bonferroni correction for a family-wise error ($\alpha_{\mathrm{corr}} = \frac{\alpha_{\mathrm{FWE}}}{K}$) is very conservative in case of spatially correlated voxels. Spatial correlation can be parametrised by **topological features** in the test statistic image, such as peak height u (voxel level), spatial extent k (cluster level), and the number of clusters c (set level) [98, 99]. In order to incorporate topological constraints, a continuous description of the discrete test statistic image can be implemented by applying (Gaussian) random field theory based on expected Euler characteristics and image smoothness. While the regional sensitivity is the highest for uncorrected data (i.e. application of height threshold $t > u_\alpha$), the specificity (reduction of FPR) is enhanced when additionally restricting the cluster level extent ($> k_\alpha$) or the number of clusters (c_α).

2.3.4 Basic principles of object recognition and characterisation of parametric 3D distributions

A simple VOI-based and a direct voxel-based quantification as described in the previous sections can be complemented by the extraction of quantitative parameters characterising intensity **histograms**, intensity (grey level) changes within a VOI (**texture**), and VOI **shape**. In the recent years such properties have gained growing popularity especially in the field of **radiomics**, which aims to reduce the need for invasive biopsies by a non-invasive characterisation of tumour heterogeneity [100–102].

Histogram and texture parameters rely on a prior discretisation of intensity values (binning), and depend on an overall intensity scaling. Discretisation of intensities within a defined VOI can either be performed for a fixed number of bins per VOI or a fixed bin width [103]. While a fixed bin width maintains the interpretation of intensities as physiologic properties (e.g. functional images such as PET), a fixed bin number per VOI focusses on normalised grey level changes within the VOI. Therefore, a fixed number of bins might be preferred in case of arbitrary intensity units (e.g. morphological MRI images). In contrast, a fixed bin size was found to be superior for e.g. PET derived data [104, 105].

Intensity- and histogram-based parameters

Common VOI statistics directly derived from intensities I_k of each voxel ($k = 1, ...K$) enclosed within the VOI include e.g. mean value, standard deviation, minimal and maximal intensity, parameter range, and coefficient of variation (COV). Less frequently applied

parameters characterising the intensity distribution include e. g.:

$$\text{Skewness} = \frac{\frac{1}{N} \cdot \sum_{k=1}^{N}(I_k - \mu)^3}{\left(\frac{1}{N} \cdot \sum_{k=1}^{N}(I_k - \mu)^2\right)^{3/2}} \quad \text{and}$$

$$\text{Kurtosis} = \frac{\frac{1}{N} \cdot \sum_{k=1}^{N}(I_k - \mu)^4}{\left(\frac{1}{N} \cdot \sum_{k=1}^{N}(I_k - \mu)^2\right)^2} - 3 \ .$$

(2.47)

The skewness is an asymmetry measure, which can be negative or positive, and the kurtosis quantifies whether the majority of values is concentrated (peaked) around the mean or distributed towards the tails of the intensity distribution. In equation (2.47) the correction -3 is inserted in order to yield 0 for a normal distribution.
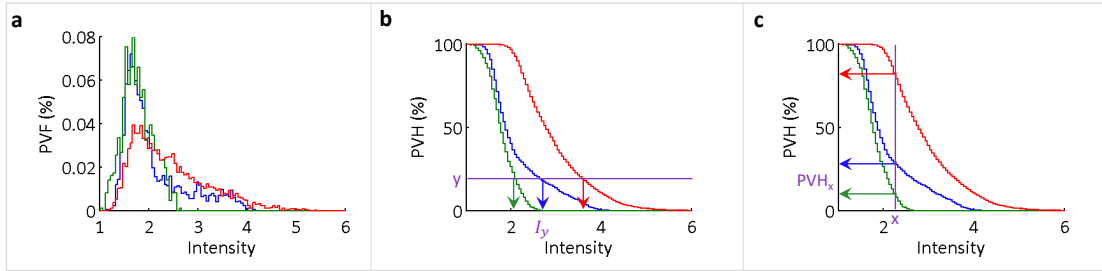

Figure 2.4: Visualisation of **a** percentage volume fractions, and **b, c** cumulative percentage volume histograms for three exemplary intensity distributions. **b** Three different I_y values for a fixed volume fraction PVH $= y\%$, and **c** different PVH$_x$ values for a fixed threshold $I = x$ are shown.

The quantification of intensities within a VOI not taking into account the spatial distribution of values can also be quantified with histogram data. The first order histogram can be normalised to the total number of voxels included in the VOI, yielding the percentage fraction of voxels within the VOI (bin content) with a certain intensity value (bin). This will be termed **percentage volume fraction (PVF)** in this thesis (figure 2.4a). For a robust quantification either a large histogram bin size can be chosen, or integration can be performed yielding a cumulated histogram (**cumulative percentage volume histogram, PVH**, figure 2.4b, c), where the volume fraction consisting of voxels with an intensity above (or below) a certain threshold is plotted against the threshold.

Quantification with cumulative histogram data can either focus on the intensity threshold (I_y, figure 2.4b) obtained for a fixed PVH value ($y\%$), or focus on a varying volume fraction (PVH$_x$, figure 2.4c) for a defined intensity threshold (x). The first is often referred to as percentile. For example I_{10} and I_{90} can be applied instead of minimal and maximal intensity, aiming to provide quantitative values which are more robust to outliers. Based on such percentiles e. g. interquartile ranges are defined ($R_{iq} = I_{75} - I_{25}$). For parametric images quantifying a physiologic process, the intensity values beyond a defined threshold (x) are assumed to be directly connected to a tissue property or disease status. In this case, it might be beneficial to quantify the volume fraction (PVH$_x$) consisting of voxels with the characteristic property. Further PVF-based histogram

parameters include e. g.:

$$\text{Entropy} = -\sum_{b=1}^{N_{\text{bins}}} \text{PVF}(b) \cdot \log_2 \text{PVF}(b) \quad \text{and}$$

$$\text{Uniformity} = \sum_{b=1}^{N_{\text{bins}}} \text{PVF}(b)^2 \ . \tag{2.48}$$

Quantification of texture by grey level changes

While a 1D intensity histogram gives the amount of voxels (bin content) with the same intensity (bin), the amount of neighbouring voxel-pairs – where one voxel has intensity i and the other intensity j – can be stored in a 2D histogram with matrix elements G_{ij}. The elements of the normalised **grey level co-occurrence matrix (GLCM)** are defined as [106]

$$g_{ij} = \frac{G_{ij}}{\sum G_{ij}}. \tag{2.49}$$

According to this definition, the GLCM is symmetric. The following exemplary texture parameters can be extracted:

$$\text{Energy}_{\text{GLCM}} = \sum_{i,j} g_{ij}^2 \ ,$$

$$\text{Entropy}_{\text{GLCM}} = -\sum_{i,j} g_{ij} \cdot log_2 g_{ij} \ ,$$

$$\text{Correlation}_{\text{GLCM}} = \sum_{i,j} \frac{(i - \mu) \cdot (j - \mu) \cdot g_{ij}}{\sigma^2} \ ,$$

$$\text{Inverse difference moment (Homogeneity)}_{\text{GLCM}} = \sum_{i,j} \frac{g_{ij}}{1 + (i - j)^2} \ ,$$

$$\text{Inertia (Contrast)}_{\text{GLCM}} = \sum_{i,j} (i - j)^2 \cdot g_{ij} \ ,$$

$$\text{Cluster shade}_{\text{GLCM}} = \sum_{i,j} ((i - \mu) + (j - \mu))^3 \cdot g_{ij} \ ,$$

$$\text{Cluster prominence}_{\text{GLCM}} = \sum_{i,j} ((i - \mu) + (j - \mu))^4 \cdot g_{ij} \ , \text{ and}$$

$$\text{Haralick's correlation}_{\text{GLCM}} = \frac{\sum_{i,j} i \cdot j \cdot g_{ij} - \mu_i \cdot \mu_j}{\sigma_i \cdot \sigma_j} \ , \tag{2.50}$$

with the weighted pixel average $\mu = \sum_{i,j} i \cdot g_{ij} = \sum_{i,j} j \cdot g_{ij}$, the weighted pixel variance $\sigma^2 = \sum_{i,j} (i - \mu)^2 \cdot g_{ij} = \sum_{i,j} (j - \mu)^2 \cdot g_{ij}$, and the means $(\mu_{i/j})$ and standard deviations $(\sigma_{i/j})$ of $g_i = \sum_j g_{ij}$ and $g_j = \sum_i g_{ij}$ [103, 106].

Shape parameters describing morphology

The quantification of VOI shape and morphology in three dimensions relies on several basic parameters, such as volume V, surface area A, maximum diameter, or smallest (λ_{least}), second largest (λ_{minor}), and largest (λ_{major}) principal component. The maximum diameter and principal components can be directly derived from voxel coordinates.

The volume can either be calculated as a sum of voxel volumes included in the VOI, or estimated from a triangle mesh representation of the VOI derived with a marching cubes algorithm [107]. This method approximates the surface of an object within a cubic voxel by a triangular mesh. The sum of tetrahedral volumes spanned by the triangles $i = 1, ..., N_f$ (with vertices a_i, b_i, and c_i) and an arbitrarily defined image origin (O) yields the total object volume

$$V_{\text{mesh}} = \sum_{i=1}^{N_f} Oa_i \cdot (Ob_i \times Oc_i)/6, \qquad (2.51)$$

where the sign is different for outward and inward facing tetrahedrons. The surface area can be approximated from the mesh with

$$A_{\text{mesh}} = \sum_{i=1}^{N_f} |a_i \cdot b_i \times a_i \cdot c_i|/2. \qquad (2.52)$$

From those basic parameters the following exemplary shape parameters can be derived (assuming 3D images):

$$\begin{aligned}
\text{Surface to volume ratio} &= A/V \ , \\
\text{Sphericity or roundness} &= \frac{\sqrt[3]{36 \cdot \pi \cdot V^2}}{A} \ , \\
\text{Compactness} &= \frac{V}{\sqrt{\pi \cdot A^3}} \ , \\
\text{Elongation} &= \sqrt{\frac{\lambda_{minor}}{\lambda_{major}}} \ , \text{ and} \\
\text{Flatness} &= \sqrt{\frac{\lambda_{least}}{\lambda_{major}}} \ .
\end{aligned} \qquad (2.53)$$

2.4   Imaging of brain pathology

For imaging of **central nervous system (CNS)** diseases, a deeper understanding on the structure and function of the **blood-brain barrier (BBB)** is required. Firstly, the prerequisite of functional brain imaging is a sufficient tracer availability, i.e. the ability to cross the BBB. Secondly, BBB disruption plays a major role in the pathophysiology of CNS diseases, where BBB breakdown can occur as a primary process, or as an secondary side effect of the disease [108]. This chapter gives a brief overview on BBB function, pathophysiologic BBB changes, and on optimal properties for BBB penetration of radio-pharmaceuticals.
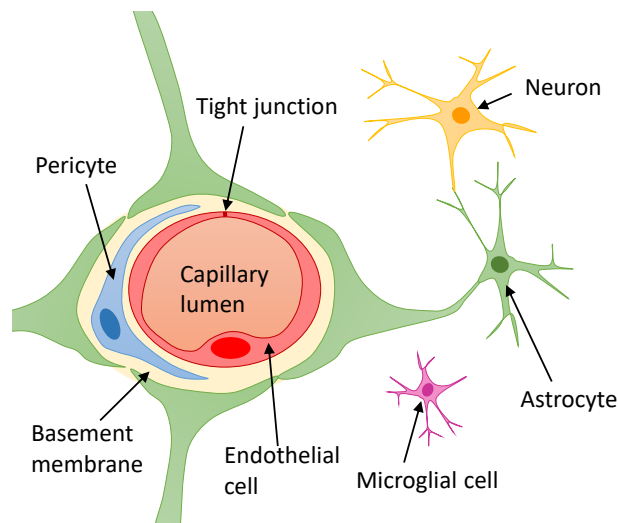
2.4.1   The blood-brain barrier

Figure 2.5: A schematic illustration of the structure of brain capillaries and the interacting components of the **neurovascular unit** responsible for the regulation of local blood flow [109, 110]. The capillary lumen is enclosed by endothelial cells (continuous) which are connected by tight junctions, and surrounded by basement membranes, pericytes, and astrocytes. Among others, pericytes support nutrition and maturation of endothelial cells, and astrocytes are involved in e.g. inflammation control, repair processes after CNS injury, and glial scar creation [111]. Furthermore, interacting neurons and microglial cells are depicted.

Endothelium in the human organism can be separated into three different types: continuous, fenestrated, and discontinuous endothelium [112,113]. In contrast to discontinuous, or fenestrated endothelium, which exhibit holes between cells (about 60 to 175 nm diameter [114]), the **continuous endothelium** consists of cells with a continuous cytoplasm and **tight junctions** between cells, ensuring a low passive permeability of ions and small hydrophilic solutes. Each organ can exhibit different types of endothelium, depending on the specification within an organ. Whereas e.g. glomerular capillaries need to be permeable for water and all small solutes of the blood plasma, tubular capillaries are only partly permeable for water, ions, or polar molecules (reabsorption of vital nutrients, and secretion of waste products via carrier proteins) [114,115].

Within the brain only capillaries of the circumventricular organs are composed of fenestrated endothelium. Among others this property enables the assessment and regulation of body fluid composition. The remaining CNS is infiltrated by capillaries with continuous endothelium, forming the so-called **blood-brain barrier (BBB)**, which is a member of the neurovascular unit (illustrated in figure 2.5). It exhibits a very high specification level, strictly regularising influx and efflux of substrates. It hence prevents permeation of neurotoxic substrates, which is especially important in the CNS, since neurogenesis in adults is limited and low [116]. Moreover, the BBB plays a role in ion homeostasis, limitation of protein availability, proliferation, and enables immune surveillance and response [117].

2.4.2   Transport mechanisms across the BBB

Different transport mechanisms across the BBB are summarised in [110, 117, 118]. Only small, lipophilic, and neutral solutes can diffuse passively into the CNS. Due to active removal from the CNS compartment by carrier-mediated efflux transporters, passive diffusion can be regulated and limited. Carrier-mediated influx or bidirectional transport enables a controlled exchange of important polar molecules, such as glucose (GLUT), amino acids (LAT), small peptides, and others. Macromolecules such as insulin, cytokines and other peptides or proteins can be transported via receptor-mediated transcytosis. Non-specific transport of positively charged macromolecules can take place via adsorptive-mediated transcytosis. Moreover a modulation of tight junctions may lead to diffusion of polar solutes or to migration of leukocytes.

2.4.3   Pathophysiology of BBB breakdown

BBB disintegration can e.g. manifest as a mutation of tight junctions, an increased expression of receptors, or as an activation of transporting cells in the endothelium. Moreover, endothelial cells in general can loose their specification if the organ environment changes, as it can be the case e.g. for brain-tumour capillaries [108, 119–121].

Different brain pathologies have shown to influence the BBB permeability [117]. For patients with e.g. brain cancer [122–125], stroke [126], or acute lesions of multiple sclerosis (MS) [127–129], a significant opening of the BBB can be observed, enabling the passage of large molecules. As a result e.g. gadolinium- (Gd^{3+}) based MRI contrast agents (CA) can leak into the CNS, and thus visualise large scale BBB disruption [130]. Age related changes [131] and chronic diseases such as e.g. Alzheimer's, cerebral small vessel disease, diabetes, or MS (chronic active lesions) lead to more subtle BBB alterations. Such less severe, yet pathological small-scale BBB changes are not visible in conventional contrast-enhanced (CE) MRI. Alternative methods have been proposed, such as the utilisation of time dependency of CA accumulation in dynamic CE (DCE) MRI [132–135], imaging of ultrasmall, superparamagnetic iron oxide particles (USPIO) [136], or imaging with PET tracers [137–139].

2.4.4   Optimal radio-pharmaceutical properties for brain imaging with PET

Optimal tracer properties for brain imaging include the following: high specific and low non-specific binding affinity, high metabolic stability, no toxicity, and the ability to cross the BBB. The latter mainly depends on tracer lipophilicity, molecular weight ($<$

$450g/mol$, i. e. small molecules with small cross-sectional area), and on the susceptibility to active efflux transport into the blood. BBB penetration of tracer metabolites is undesirable and is usually low, since radio-metabolites tend to be less lipophilic than the parent compound. Further relevant properties as summarised in [140–142] are listed below.

- **Selectivity**: Ideally, a tracer should be specific only for one target. In case of multiple targets, the relative contribution within tissue, and the tracer affinity for each target type needs to be known.

- **Affinity**: A high specific binding affinity compared to the amount of non-specific binding is desirable. Moreover a high concentration of binding sites of the target region is essential.

- **Scan duration**: The choice of an optimal scan window highly depends on the kinetics of tracer uptake in tissue. After the initial uptake phase, equilibrium between tracer concentration in tissue and in blood is reached [143]. This is followed by a washout phase, where free plasma concentration decreases. The time after which equilibrium is reached decreases for an elevated plasma clearance in the periphery and local blood flow (equation (2.23)), and increases with affinity and receptor density, but does not necessarily depend on the protein bound fraction.

- **Occupancy**: For diagnostic use the injected amount of radio-pharmaceutical compound should be low, i. e. the occupancy of binding sites should be negligible in order to preserve linearity.

- **Delivery**: Tracer delivery at the tissue of interest is described by the (plasma) input function and the respective plasma clearance. A high clearance results in a reduced brain uptake and an early onset of washout phase. If tracer affinity and BBB permeability are high enough a high clearance is preferred due to the reduced measurement time-window.

- **Lipophilicity** (logP 1.5-4): A high tracer lipophilicity leads to an increased brain penetration, but also to an elevated level of non-specific binding, and a higher fraction of tracer bound to plasma proteins (lower free fraction, i. e. reduced tracer availability). Since these effects might be contradictory, a reliable prediction of BBB penetration and levels of non-specific binding is challenging [108, 144, 145]. Also, *in vitro* properties of radio-tracers need not to be predictive of *in vivo* characteristics [146].

Chapter 3

Studies

3.1 Objectives of this thesis

For the non-invasive assessment of central nervous system diseases, imaging of morphological and functional tissue properties is of major interest. The provided information on CNS pathophysiology is highly relevant for diagnosis, treatment planning, and prediction of treatment response, disease progression, or recurrence. The objective of this work was the evaluation of methodological aspects relevant for quantification in brain PET imaging, the development of advanced image processing techniques, and an application for non-invasive characterisation of lesions in multiple sclerosis and glioma patients.

For the evaluation of lesion segmentation methods and PET signal within lesions, preliminary phantom experiments were conducted with a NEMA NU 2-2001 spheres phantom (section 3.2). This included an assessment of mean and maximal recovery coefficients for true sphere volumes depending on volume, signal-to-background ratio, and on the reconstruction algorithm. Various threshold-based segmentation strategies were investigated, aiming to yield true object boundaries. For this, the boundary-reproducing thresholds were expressed in terms of different segmentation approaches. Moreover, image noise properties were evaluated and described with a noise model.

The first study (publication attached in chapter 4) is described in section 3.3 and deals with quantification approaches for TSPO imaging with ^{18}F-GE-180 in patients with multiple sclerosis. The main methodological challenges include the definition of a pseudo-reference region in order to provide inter- and intra-subject comparable quantitative parameters and to avoid invasive arterial blood sampling. This was established by first choosing an anatomically defined region which is least affected by disease and minimises variability among healthy controls, and then excluding voxels from this region suspected to be affected by disease. Segmentation based on maximal and background activity as established in phantom experiments was applied for lesion segmentation, enabling a quantification based on mean and maximal parameters. Anatomically defined tissue and lesion quantification based on static SUV ratios (section 2.2.4) was compared to results from pharmacokinetic modelling.

In the second study (publication attached in chapter 5) with dynamic ^{18}F-FET PET data voxel-wise parametric information was employed for non-invasive glioma characterisation. In addition to the published results evaluating the diagnostic accuracy of percentage volume histograms derived from heuristic parameters (section 2.2.4), additional results are presented in section 3.4. Intensity, histogram, and texture parameters were derived from parametric images, and pharmacokinetic modelling parameters from

average VOI TACs were related to the established heuristic parameters. The capability to distinguish molecular genetic and histologic glioma grades was assessed for all extracted features.

3.2 Preliminary phantom studies: evaluation of image quality and comparison of threshold-based segmentation methods

3.2.1 Background

In order to evaluate the quality of PET data, i. e. the signal recovery and noise properties, and to assess the reliability of volume segmentation methods, several measurements were performed with the NEMA NU 2-2001 spheres phantom. A summary on different segmentation methods is given in section 2.3.1. The aim of this investigation was to characterise and identify the most suitable segmentation method for each processing task being performed in the subsequent studies.

3.2.2 Material and methods

Imaging

All scans were acquired in list-mode on a Biograph 64 PET/CT device (Siemens Healthineers, Erlangen, Germany) [147] with a scan duration of 20 minutes. Image reconstruction was performed with FBP, OSEM2D, OSEM3D, and PSF-based OSEM3D (TrueX). Sinograms for FBP and OSEM2D reconstruction were calculated by Fourier rebinning [148]. Reconstruction with FBP included a 4.9 mm Hann filter. OSEM2D and OSEM3D reconstructions were performed with a Gaussian post-reconstruction filter (4 mm FWHM). Iterative reconstruction included 4 iterations with 8, 16, and 21 subsets (equivalent number of iterations: 32, 64, and 84).

SBR	BG (kBq/mL)	Spheres (kBq/mL)
30	1.4	42
15	1.4	21
8	1.4	10
8	2.9	24
6	3.0	18
4	3.7	15
2	6.4	13

Table 3.1: Signal-to-background ratios (SBR) for the used background (BG) and sphere concentrations.

Evaluation of recovery coefficients and volume segmentation methods

Recovery coefficients (RC) of mean and maximum activity were calculated for true sphere volumes as the ratio between image-derived and true activity concentration. The sphere diameters of the NEMA NU 2-2001 phantom are: 37, 28, 22, 17, 13, and 10 mm. Background and spheres were filled homogeneously with the activity concentrations listed in table 3.1. A reconstruction-specific calibration was applied in order to obtain 100% recovery for activities measured in the BG VOI.

Different threshold-based segmentation methods were evaluated, aiming to delineate true volumes. In the following such thresholds will be referred to as **boundary reproducing thresholds (BRT)**. The optimal BRTs were extracted automatically from

phantom data with an iterative algorithm, which compares the current volume with the given true volumes at each iteration step.

Segmentation strategies included (1) simple thresholds relying only on maximal or mean signal within the volume (BRT $\approx F_{max/mean} \cdot I_{max/mean}$), or (2) on background signal of the surrounding tissue (BRT $\approx F_{BG} \cdot I_{BG}$), and (3) thresholds taking both properties into account:

$$\text{BRT} \approx (I_{max/mean} - I_{BG}) \cdot F_{BG,max/mean} + I_{BG}. \tag{3.1}$$

By applying iterative algorithms, a threshold dependency on the lesion volume can be taken into account (assuming sphericity). This will be exemplarily incorporated for evaluation of segmentation results obtained with $F_{BG,mean}$.

Noise properties in terms of coefficient of variation

Coefficients of variation (COV) were measured in homogeneous background for varying activity concentrations (table 3.1), and described by a theoretical noise model. For this, it was assumed that the image statistics can be described by a Gaussian distribution $\mathcal{N}(\mu = \tilde{A}, \sigma = \sqrt{\tilde{A}})$ (see sections 2.1.2 and 2.1.3), where $\tilde{A}$ is the total number of counts (accumulated activity) within a time frame $[t_1, t_2]$ (with equation (2.5)):

$$\begin{aligned} \tilde{A} &= \int_{t_1}^{t_2} A_0 \cdot e^{-\lambda t} dt \\ &= \frac{A_0}{\lambda} \cdot (e^{-\lambda t_1} - e^{-\lambda t_2}). \end{aligned} \tag{3.2}$$

The measured image statistics can be estimated based on the above assumptions and a constant scaling factor a with the following equation:

$$\text{COV} = a \cdot \frac{\sqrt{\tilde{A}}}{\tilde{A}} = a \cdot \frac{1}{\sqrt{\tilde{A}}}. \tag{3.3}$$

3.2.3   Results

Evaluation of signal recovery and volume segmentation methods

Figure 3.1 shows the measured RC and BRT data depending on sphere volume (1st column), number of equivalent iterations (2nd column) and SBR (last column). Recovery was comparable for FBP and OSEM2D/3D reconstruction: RCs were not sensitive to the number of equivalent iterations, and RC_{max} values were approximately equal to 1 for larger spheres (figure 3.1a). PSF-based reconstruction (TrueX) yielded slightly higher RC_{mean}, and RC_{max} values were above 1, with discontinuous behaviour for small spheres. In general RC_{mean} increased slightly for SBR values below 8, while RC_{max} showed non-linear behaviour in case of OSEM reconstruction, and decreased in case of TrueX reconstruction.
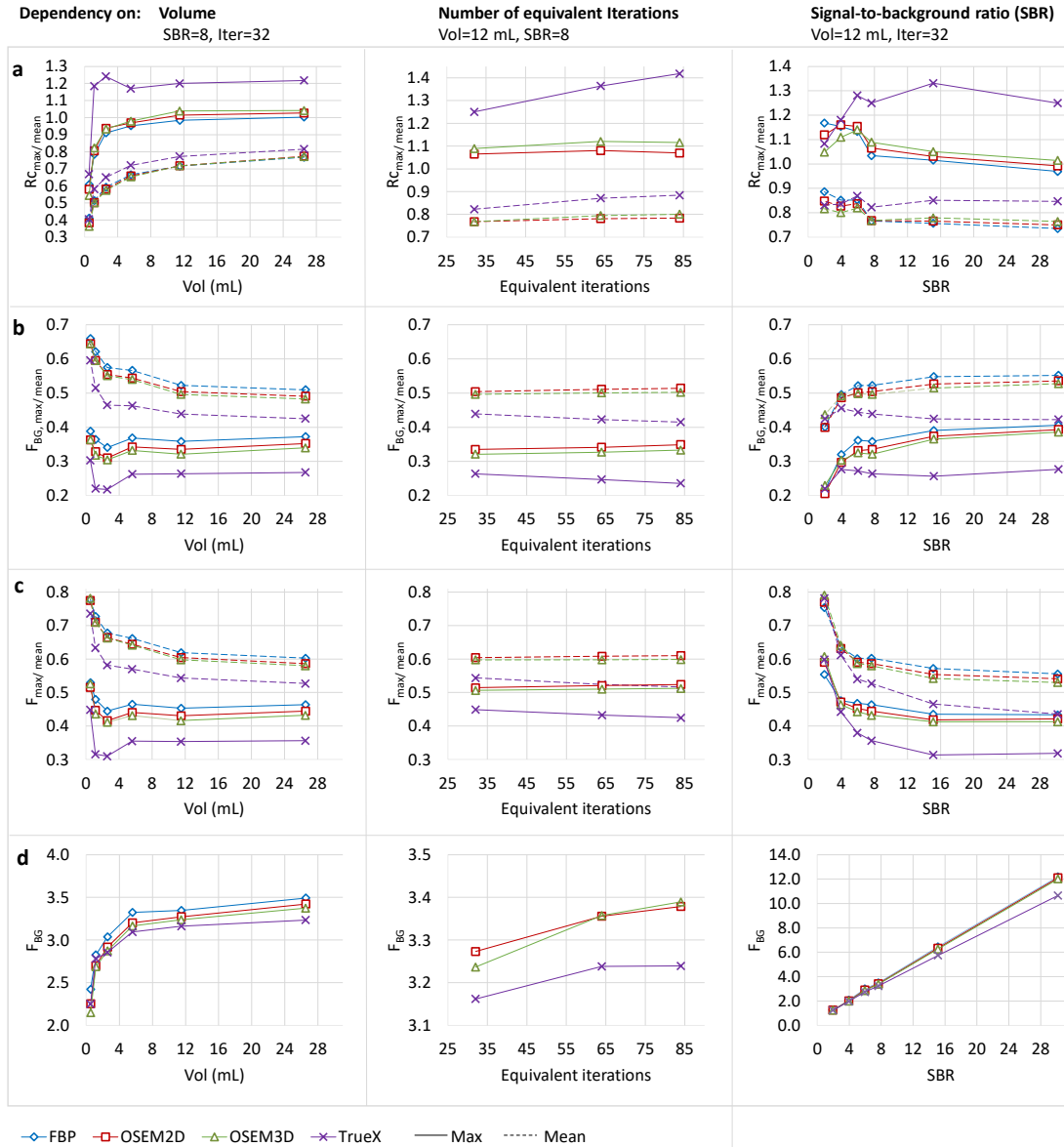
Figure 3.1: **a** Recovery coefficients (RC) obtained from mean (dashed lines) and maximum (solid lines) activities, and optimal thresholds reproducing true sphere volumes expressed in terms of: **b** $F_{BG,max/mean}$ (equation (3.1)), **c** fraction $F_{max/mean}$ of maximal/ mean signal, and **d** fraction F_{BG} of background signal. Dependency of recovery coefficients and representations of boundary reproducing thresholds on sphere volume (1st column), number of equivalent iterations during reconstruction (2nd column), and signal-to-background ratio (3rd column). Results are presented for FBP, OSEM2D, OSEM3D, and TrueX reconstructions.

The optimal threshold showed a dependency on sphere volume for all included segmentation methods (figure 3.1b–d), which was most pronounced for small volumes. $F_{BG,mean}$, and F_{mean} decreased with increasing volume. $F_{BG,max}$, and F_{max} were approximately constant for larger spheres, and presented with non-linear behaviour for spheres smaller than 3 mL. F_{BG} showed a continuous increase with sphere volume, saturating

for larger spheres. While $F_{BG,max/mean}$ and $F_{max/mean}$ were approximately independent of the number of equivalent iterations, F_{BG} showed an increasing behaviour. The lowest dependency on SBR was found for $F_{BG,max/mean}$ values. $F_{max/mean}$ was decreasing with increasing SBR values, which was most pronounced for PSF-based reconstruction (TrueX). However, the strongest dependency on SBR values was found for F_{BG}.
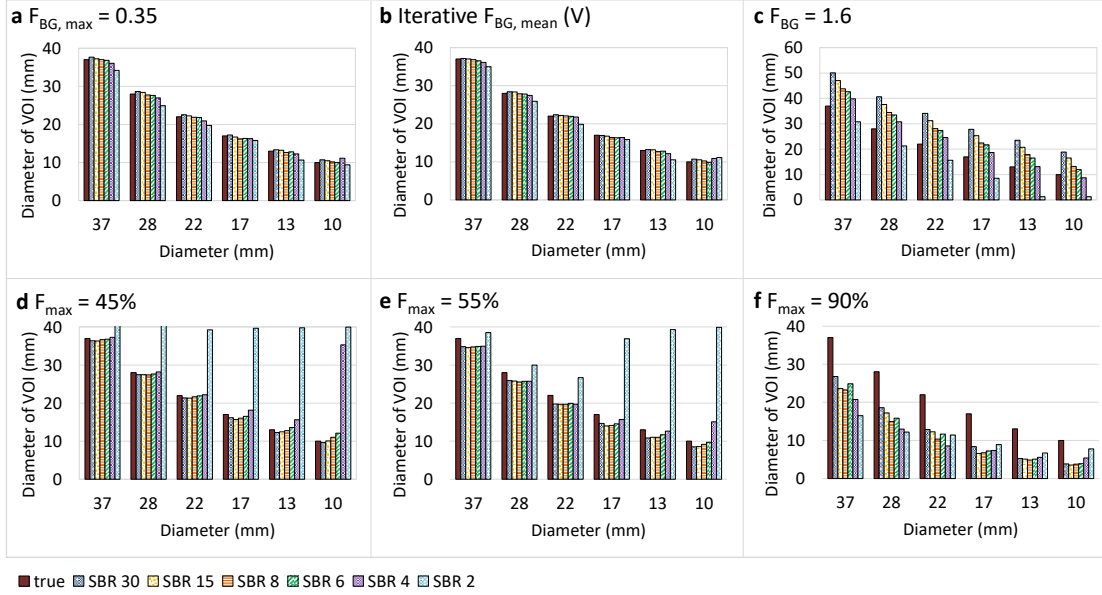

Figure 3.2: Comparison of different volume segmentation methods, exemplarily shown for OSEM2D reconstructed images with 4 mm Gaussian filter and 32 equivalent iterations. Estimated diameters of segmented VOIs in comparison to true sphere diameters: **a** $F_{BG,max} = 0.35$, **b** iterative $F_{BG,mean}(V)$, **c** $F_{BG} = 1.6$, **d** $F_{max} = 45\%$, **e** $F_{max} = 55\%$, and **e** $F_{max} = 90\%$.

The estimated VOI diameters obtained by applying the different segmentation methods are exemplarily shown in figure 3.2 for OSEM2D reconstruction with a 4 mm Gaussian filter and 32 equivalent iterations. An average fixed $F_{BG,max}$ threshold was calculated for the three largest spheres, and all SBRs except the lowest SBR of 2. For iterative segmentation the dependency of $F_{BG,mean}$ on the sphere volume (V) was estimated by fitting the following equation to the measured phantom data: $F_{BG,mean}(V) = a \cdot e^{-b \cdot V} + c$. A theoretical curve might also be obtained by convolving the activity distribution within spheres of varying size with the PSF [83] (see section 2.1.5). Both $F_{BG,max/mean}$ methods yielded reliable volume estimates for all sphere sizes and SBRs (figures 3.3a and b). As expected, the volume estimation with F_{BG} showed a strong SBR dependency (figure 3.2c). A good correspondence between volumes segmented with $F_{max} = 45\%$ and true volumes was found for SBR > 6 (figure 3.2d). However, for SBR values below 5 the threshold defined by $45\% \cdot I_{max}$ seemed to approach the background level, which resulted in a strong overestimation for all segmented volumes. In case of $F_{max} = 55\%$ this issue was still relevant, however only for the three smallest spheres with SBR = 2 (figure 3.2e). VOI diameters obtained with $F_{max} = 90\%$ underestimated true diameters, and showed a dependency on SBR (figure 3.2f).

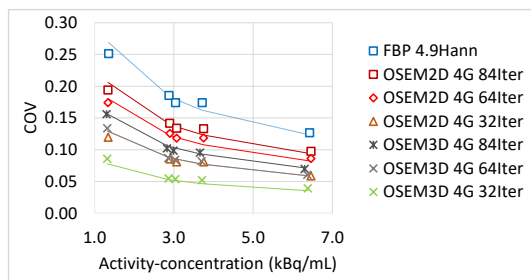**Noise properties in terms of coefficient of variation**

Figure 3.3: Coefficient of variation (COV) measured for varying background concentrations and different image reconstruction methods (markers), and model representation according to equation (3.3) (lines).

As can be seen in figure 3.3, the noise model described by equation (3.3) fits the measured COV values well. The highest noise could be found in images reconstructed with FBP, followed by OSEM2D images. The best noise properties were found for OSEM3D data [149, 150]. As expected noise increased with the number of iterations. Not shown are COV data for PSF-based reconstruction (TrueX) without additional filtering ("allpass"), which were comparable to data from OSEM3D reconstruction with a Gaussian filter with 4 mm FWHM (i. e. lower noise level with PSF-based reconstruction).

3.2.4   Discussion

Contrast-based segmentation methods yielded the most robust and accurate results for the estimation of true boundaries in case of spherical and homogeneously filled lesions. Hence, this was applied for the delineation of focal MS lesions in the first publication (chapter 4). For the definition of glioma volumes, a threshold based on $F_{BG} = 1.6$ has been previously established and validated with stereotactic biopsies [151]. The presented phantom measurement results indicate, that the segmented lesion volumes exhibit a SBR dependency. This results in an overestimation of lesion volumes for SBR larger than 4, and an underestimation for smaller SBR values. For an encompassing 3D definition of tumour tissue additional simulation experiments or studies incorporating stereotactic biopsies should be performed.

   The validated noise model might be utilised e. g. for analytical simulation of PET data by taking into account the imaging PSF [17] and the described noise properties with $A_{0,noise} = A_0(1 + COV \cdot \mathcal{N}(0,1))$ (sections 2.1.3 and 2.1.5). The simulation of PET data either with analytical, or Monte Carlo-based methods is an important tool for the validation of various image processing and quantification steps, such as e. g. the segmentation of non-spherical objects. Logan *et al.* [69] applied a similar model for validation of a method aiming to reduce noise influence in graphical analysis with Logan plots.

   PSF-based OSEM3D reconstruction appeared to enhance lesion detectability, however at the cost of a higher risk of false positives. In line with previous studies [152, 153], a non-linear behaviour for sub-centimetre lesions could be observed (figure 3.4) [20]. To overcome the non-linear behaviour of maximal values within small lesions, an additional smoothing filter might be applied during PSF-based OSEM3D reconstruction. A sys-

tematic comparison of lesion detection and quantification properties for reconstruction with and without PSF inclusion is desirable. Future studies should include phantom or simulation data of sub-centimetre lesions.
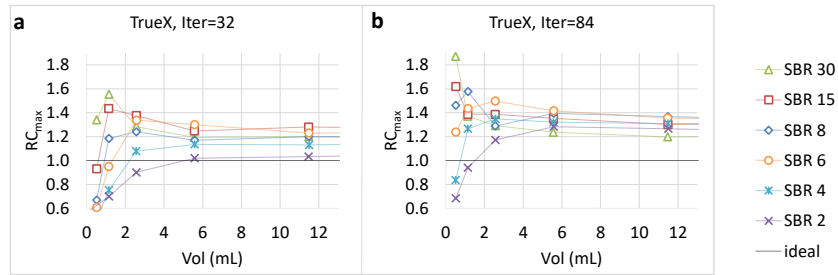

Figure 3.4: Discontinuous behaviour of RC_{max} for small spheres in case of PSF-based reconstruction (TrueX) shown exemplarily for varying SBR values and reconstruction with **a** 32, and **b** 84 equivalent iterations.

3.3 Evaluation of quantification issues of TSPO PET imaging with ^{18}F-GE-180 in patients with relapsing-remitting multiple sclerosis

3.3.1 Background

The chronic autoimmune disorder multiple sclerosis (MS) is characterised by CNS inflammation, demyelination, and neurodegeneration. The mean age at diagnosis is about 38 years, and incidence is higher for women, and increases with latitude [154,155]. Several genetic and environmental aspects were identified as risk factors, while e. g. vitamin D is suspected to be protective [156].

It is hypothesised, that the peripheral immune system (activation by extrinsic antigens) is most relevant in the early phase of relapsing-remitting MS (RRMS), causing acute focal MS lesions, detectable with CE MRI. Acute active MS lesions are comprised of activated T and B lymphocytes, macrophages, and microglia. In early stages the disease is characterised by demyelination, followed by repair processes (remyelination) and scar creation. In progressive MS (PMS) the local (innate) immune system of the CNS becomes more important, resulting in an widespread global CNS inflammation, and an increased degeneration of neuronal axons promoted by the pro-inflammatory reaction (production of neurotoxic factors) of activated microglia together with blood-borne macrophages. Chronic active lesions of progressive disease expand slowly, whereby microglia and macrophages build a ring around the lesions.

Diagnosis and staging of MS

Diagnosis and staging of MS predominantly relies on a precise documentation of clinical and paraclinical information, and of spatio-temporal development as assessed by different MR protocols [130]. A summary on diagnostic strategies based on MR-imaging can be found in [157]. As previously discussed by Absinta *et al.* [129], the correlation of MRI findings with clinical phenotype or course of disease remains poor. For a more direct visualisation of disease activity, specific molecular imaging (PET) tracers were developed. This includes e. g. tracers targeting the 18-kDa translocator protein (TSPO), which is up-regulated in activated microglia. TSPO expression can also be found on the outer mitochondrial membrane of astrocytes, endothelial cells, infiltrating macrophages, and tumour cells. A summary on different TSPO tracers and applications for imaging of MS is given in [158,159].

Methodological challenges of TSPO PET

Encompassing reviews on the methodological challenges of TSPO quantification were published e. g. by Hinz and Boellaard [160] and Turkheimer *et al.* [161]. The main aspects and approaches thereof are listed below.

- The first generation TSPO tracer [11]C-(R)-PK11195 was extensively investigated for a large variety of disease conditions [159,162]. The main drawback of this tracer was the low signal-to-background ratio and the low BBB penetration, which lead to the development of various second generation tracers targeting TSPO.

- The second generation TSPO tracers aiming to enhance binding affinity, have shown to be sensitive to a single nucleotide polymorphism in the TSPO gene

(rs6971), which causes differences in binding affinities. As described in chapter 4, individuals can be labelled as low-, medium-, or high-affinity binders (LAB, MAB, HAB) [163–165].

- Another aspect is the high protein binding, which may cause variability among subjects. Also, an increased signal from TSPO at the BBB is observed, limiting the availability in tissue, and the detectability of increased activation in tissue [166].

- In order to avoid continuous blood sampling and an elaborate – and yet error prone – analysis of metabolite fraction and fraction bound to proteins, it is desirable to perform quantification based on information from reference tissue data. However, an anatomically defined reference region without TSPO binding sites but similar non-specific binding (section 2.2.3) does not exist in the CNS. Yet, if a brain region exists, in which TSPO expression in not affected by disease, such a reference region may potentially yield $BP_{apparent}$ estimates, which correlate with true BP_{ND} (if other confounding effects such as age, gender etc. are neglected). Several data-driven, and supervised clustering approaches have been proposed, aiming to extract unaffected cortical voxels [73,89,167–169]. However, those methods rely on dynamic PET data, and in some applications affected voxels could not be excluded sufficiently [170,171].

Outline

The first publication attached in this thesis (chapter 4) aimed to evaluate quantification methodology for the third generation TSPO tracer ^{18}F-GE-180 in RRMS patients. This included (1) the extraction of a pseudo-reference region, (2) the segmentation of small lesions based on preliminary phantom measurements (section 3.2), and (3) the validation of a quantification approach utilising late summation images. Here, supplementary results on pharmacokinetic modelling are presented, which were obtained with an IDIF rescaled and corrected based on a limited number of discrete blood samples.

3.3.2 Material and methods

Patients and imaging

The details on patient characteristics and imaging properties can be found in the methods section of the first publication attached in this thesis (chapter 4) [172]. Supplementary results obtained with pharmacokinetic modelling with blood input function will be presented for a sub-group of 7 RRMS patients. For the extraction of a continuous whole blood IF a previously described method was applied, which relies on an image-derived activity concentration within the carotid arteries and a scaling based on manual blood samples [53] (section 2.2.1). The method utilises dynamic scans reconstructed with OSEM3D taking into account the imaging system PSF (PSF3D: 4 iterations, 16 subsets, no filter, TrueX, Siemens Medical Solutions, Erlangen, Germany).

Anatomical brain regions, reference tissue extraction, and segmentation of lesions

Anatomical brain regions were defined as described in chapter 4 and section 2.3.2. The methodological details for the extraction of a **pseudo-reference region (PRR)** and

for lesion segmentation are presented in the methods and results sections of the first publication (chapter 4) [172]. In brief, we aimed to identify the anatomically defined region which exhibits the lowest fraction affected by disease and which minimises variability among healthy subjects. Assessment of voxel-wise differences was performed with statistical parametric mapping (section 2.3.3).

Lesions were assumed to be spherical, and segmented with a threshold based on maximal and background uptake as established and validated in the phantom study presented in section 3.2.

Blood sampling

Manual arterialised venous blood samples were taken at 5, 15, 30, 60, and 85 min p.i. for 7 RRMS patients (BS-subgroup) [173]. Separation of plasma from blood cells was achieved by centrifugation of the whole blood samples (3000g). The determination of plasma-to-blood ratio and metabolite analysis were performed on blood samples taken at 5, 15, and 30 min p.i.. Activity concentration of whole blood and plasma was measured with a gamma counter (Cobra Quantum 5002, Packard), which was cross-calibrated with the PET device via dose calibrator (Veenstra Instruments, Netherlands), and decay corrected to time of injection. For protein precipitation, plasma samples were diluted with ice cold acetonitrile (1:4) and centrifuged (16000g) for 3 min. Blood sample activity concentrations were below our calculated HPLC detection limit of 33 kBq/mL. Therefore, the fraction of metabolised tracer in supernatant was evaluated with thin layer chromatography (silica gel TLC plate, EtOAc/EtOH 4:1; Macherey-Nagel, Düren, Germany) [174, 175].

Input function

The arterial input function for modelling was obtained with manual blood samples in combination with an IDIF from PSF3D images as validated by Mourik for ^{11}C-(R)PK11195 [53]. The first frames during which arterial influx into the brain is visible were used for VOI definition in carotid arteries ("4 hottest pixels per plane" method [53]). A bi-exponential fit was performed on the IDIF and the resulting function was then scaled to the activity of the five whole blood samples.

This was followed by a correction for plasma-to-blood ratio and metabolites. The plasma-to-blood ratio was approximated to be constant over time [176, 177], and the following model function (adapted from [178]) was fitted to the measured parent fractions in plasma:

$$f_p(t) = (1 - q_2) \cdot e^{q_1 \cdot t} + q_2. \tag{3.4}$$

Pharmacokinetic modelling

For each anatomical brain region of the BS-subgroup and for lesions visible in PET, mean TACs were generated, and analysed with PMOD Kinetic Modelling tool (v3.4, PMOD Technologies, Zurich, Switzerland). Corrected Akaike information criterion (equation (2.19)) was applied for model comparison.

Volumes of distribution V_T were determined with 1TC-V_B model, reversible 2TC4k-V_B model, and Logan GA (fixed $t^* = 20$ min p.i.) using metabolite corrected plasma input function and whole blood fraction V_B (equation (2.18)). With this, the distribution volume ratios (DVR) were calculated (section 2.2.3) and compared to simple SUV ratios

from static 60-90 min p.i. images ($SUVR_{60-90}$, section 2.2.4). The 2TC4k-V_B model also provided binding potential estimates $BP_{ND,2TC}$. The applicability of Logan graphical analysis for ^{18}F-GE-180 has been validated previously for healthy controls [176,179]. In order to assess which compartmental model provides the best description of anatomical VOI- and lesion-TACs, also an irreversible 2TC3k-V_B compartment model was included.

Kropholler et al. [180] found compartment modelling with K_1/k_2 fixed to a whole cortex value to be optimal for improved convergence in ^{11}C-(R)PK11195 brain studies. In this study, for each patient, K_1/k_2 and blood volume fraction V_B were set by coupled fitting of all anatomical brain regions [181].

Correlation of modelling parameters

BP_{ND} relative to non-displaceable uptake was derived directly from 2TC4k-V_B model parameters for the BS-subgroup ($BP_{ND,2TC} = k_3/k_4$). Since there is no reference tissue available for ^{18}F-GE-180, which is devoid of specific binding, the quantity of interest was specific binding relative to healthy tissue PRR (equation (2.35)):

$$\text{DVR} = \frac{V_T}{V_{T,PRR}} = \text{BP}_{apparent} + 1, \tag{3.5}$$

which is smaller than $BP_{ND} + 1$ if $BP_{ND,PRR} > 0$.

The applicability of a simplified ratio-based quantification was assessed by comparing $SUVR_{60-90}$ values to $BP_{ND,2TC}$, $DVR_{1/2TC}$, and DVR_{Logan}. Pearson's correlation coefficients were determined for all brain tissue regions and lesions of the BS-subgroup.

3.3.3 Results

Input function

A mean plasma-to-blood ratio of 1.53±0.08 was measured. Two separable radio-labelled metabolite clusters were identified by TLC. The averaged parent fraction of tracer in plasma depending on time p.i. is shown in figure 3.5a. The results are consistent with previous publications for ^{18}F-GE-180 in human controls [176,177]. However, we observed a higher variability between subjects and only two separable instead of three metabolite clusters, most probably due to a lower resolution of TLC compared to HPLC. The respective averaged parent in plasma and whole blood TACs are given figure 3.5b.
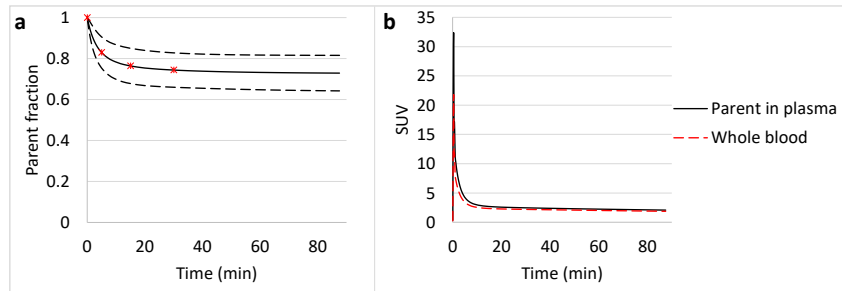

Figure 3.5: Results from metabolite analysis, whole blood and parent in plasma time activity curves averaged over 7 patients from BS-subgroup. **a** Parent fraction: measured data (red *), fit results (mean: solid line, mean ± standard deviation: dashed lines). **b** Whole blood TAC (dashed line) and parent in plasma TAC (solid line).

Pharmacokinetic modelling

Reversible 2TC4k-V_B model was preferred (lowest AIC$_C$) in 79% of anatomical VOI-TACs, and 54% of lesion-TACs. An irreversible 2T3k-V_B model was selected in 21% of anatomical VOI-TACs, and 37% of lesion-TACs. In 9% of lesion TACs the 1TC-V_B model was preferred. Average AIC$_C$ values were higher for lesion-TACs (95) compared to anatomical VOI-TACs (66), additionally indicating that lesions are less well described by the 2TC4k-V_B model. Kinetic analysis with 2TC4k-V_B model and with linearising Logan plot yielded low volumes of distribution V_T, and a non-negligible amount of specific binding BP$_{ND,2TC}$ in anatomical brain regions (tables 3.2 and 3.3). Average transfer rates K_1, k_2, k_3, and k_4 (2TC4k-V_B model) were 0.07 mL/cm^3, 1.6, 0.20, and 0.08 for anatomical VOI-TACs, and 0.05 mL/cm^3, 1.1, 0.29, and 0.07 for lesion-TACs.

Mean $\pm$ SD	$V_{T,1TC}$	$V_{T,2TC}$	$V_{T,Logan}$
PRR	0.12 $\pm$ 0.02	0.14 $\pm$ 0.03	0.17 $\pm$ 0.04
Brainstem	0.13 $\pm$ 0.04	0.19 $\pm$ 0.04	0.21 $\pm$ 0.05
Cortical GM	0.13 $\pm$ 0.03	0.16 $\pm$ 0.03	0.19 $\pm$ 0.04
Thalamus	0.14 $\pm$ 0.05	0.19 $\pm$ 0.03	0.22 $\pm$ 0.04
Cerebellar GM	0.13 $\pm$ 0.04	0.16 $\pm$ 0.04	0.20 $\pm$ 0.05
White matter	0.11 $\pm$ 0.03	0.15 $\pm$ 0.03	0.18 $\pm$ 0.03
Lesions	0.21 $\pm$ 0.07	0.26 $\pm$ 0.07	0.26 $\pm$ 0.06

Table 3.2: Volumes of distribution V_T in mL/cm^3 from 1TC-V_B, and 2TC4k-V_B model, and linearising Logan GA for anatomical brain regions and lesions of BS-subgroup.

Mean $\pm$ SD	BP$_{ND,2TC}$	DVR$_{1TC}$	DVR$_{2TC}$	DVR$_{Logan}$	SUVR
PRR	2.1 $\pm$ 0.4	1.00 $\pm$ 0.00	1.00 $\pm$ 0.00	1.00 $\pm$ 0.00	1.00 $\pm$ 0.00
Brainstem	3.2 $\pm$ 0.8	1.15 $\pm$ 0.23	1.38 $\pm$ 0.29	1.27 $\pm$ 0.14	1.29 $\pm$ 0.15
Cortical GM	2.5 $\pm$ 0.4	1.13 $\pm$ 0.09	1.16 $\pm$ 0.09	1.13 $\pm$ 0.07	1.14 $\pm$ 0.07
Thalamus	3.2 $\pm$ 0.6	1.22 $\pm$ 0.22	1.36 $\pm$ 0.16	1.29 $\pm$ 0.07	1.31 $\pm$ 0.08
Cerebellar GM	2.6 $\pm$ 0.6	1.14 $\pm$ 0.12	1.17 $\pm$ 0.13	1.15 $\pm$ 0.10	1.16 $\pm$ 0.09
White matter	2.4 $\pm$ 0.3	0.99 $\pm$ 0.12	1.11 $\pm$ 0.07	1.05 $\pm$ 0.04	1.07 $\pm$ 0.04
Lesions	4.7 $\pm$ 1.5	1.73 $\pm$ 0.37	1.83 $\pm$ 0.40	1.52 $\pm$ 0.17	1.59 $\pm$ 0.12

Table 3.3: Binding potentials BP$_{ND,2TC}$ from 2TC4k-V_B model, and distribution volume ratios (DVR) from 1TC-V_B, and 2TC4k-V_B model, and linearising Logan GA for anatomical brain regions and lesions of BS-subgroup.
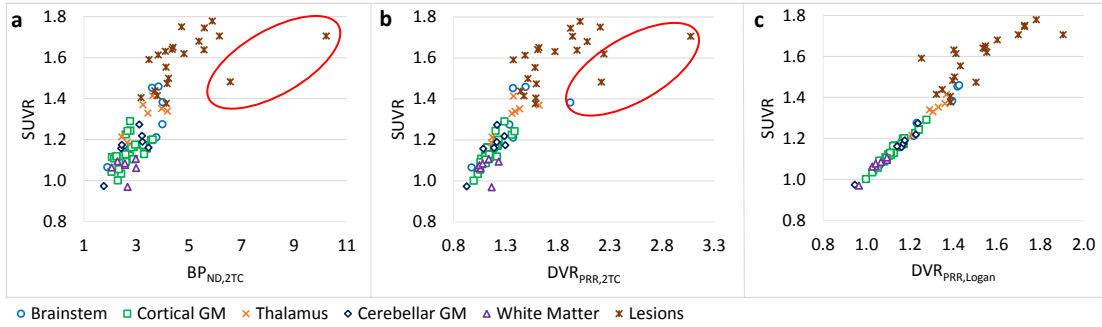
Correlation of modelling parameters

Figure 3.6: Scatter plots for BS-subgroup. SUVR plotted against **a** $BP_{ND,2TC}$, **b** DVR_{2TC}, and **c** DVR_{Logan}. For lesions with a continuously increasing kinetic (red in a and b), the 2TC4k-V_B model was less robust in particular for lesions with a continuously increasing kinetic (red in a and b).

Correlation with $SUVR_{60-90}$ was highly significant ($p < 0.001$) for all parameters presented in table 3.3. The strongest correlation was found for DVR_{Logan} ($\rho = 0.96$, figure 3.6c). Lower correlation coefficients were found for $BP_{ND,2TC}$ from 2TC4k-V_B ($\rho = 0.80$, figure 3.6a), DVR_{1TC} ($\rho = 0.87$), and DVR_{2TC} ($\rho = 0.86$, figure 3.6b).

The outliers visible in Figures 6a and 6b are lesions. This is due to the continuously increasing kinetics of these lesions (within the 90 min scan time window), which is not properly dealt with by the reversible 2TC4k-V_B model. In contrast, linear Logan GA with only two fit parameters, and static $SUVR_{60-90}$ yielded more robust parameter estimates (figure 3.6c).

3.3.4 Discussion

The results obtained for V_T were consistent with previously published healthy control data [176, 177, 179]. In concordance with these previous studies, we found that the reversible 2TC4k-V_B model was optimal for the quantification of brain tissue. In this study, for lesion quantification also the reversible 2TC4k-V_B model was predominantly selected. However, in some cases an irreversible 2TC3k-V_B model yielded lower AIC_C values. This might be caused by the fact, that a reversible 2TC4k-V_B model does not converge well for continuously increasing TACs, as it was observed in focal MS lesions (90 min time window). Static 60-90 min imaging with a PRR-based SUVR quantification correlated well with DVR results from full kinetic modelling.

Feeney *et al.* [177], and Zanotti-Fregonara *et al.* [179] indicated that their modelling results failed to describe the initial sharp peak of tissue TACs, and both also reported very low K_1 values. This might give rise to the assumption, that the optimisation algorithm provides a local minimum with an unfavourably low K_1. Since the average parent in plasma and whole blood TACs extracted in this study are in good correspondence to previously published data [176, 177, 179], it might be reasonably assumed, that the estimated micro-parameters should be in a similar range. Although the macro-parameters are in good correspondence to the previously published data, the micro-parameters estimated in this study were higher. Interestingly, e.g. the efflux rates k_2 were relatively high especially for anatomical VOI-TACs. This might support the hypothesis, that

^{18}F-GE-180 is a substrate to efflux pumps or transporters, which causes an overall low uptake (V_T) [176, 177, 182]. In that case, the elevated uptake observed for MS lesions might either be caused by alterations of the BBB such as a reduced expression of active efflux pumps or transporters, or due to an increase in specific binding to TSPO. However, all modelling results need to be interpreted with caution, since model selection criterion scores (independent of data scaling) were low in both, previously published studies, and results presented here. Further attempts to explain the low uptake in the CNS include an influence from a high fraction bound to plasma proteins, which however does not necessarily affect brain penetration and was comparable to other TSPO tracers (section 2.4.4) [179]. Moreover, ^{18}F-GE-180 presents with favourable properties such as a high plasma fraction, low metabolite fraction, high lipophilicity (logD at pH 7.4: 2.95 [183]), high affinity for TSPO (0.87 nM [183]), and a constantly high availability in blood. In summary, the most likely explanation seems to be a high efflux rate rather than a low BBB penetration.

It is currently controversially discussed, whether the observed elevated ^{18}F-GE-180 signal in lesions of human glioma and RRMS patients is predominantly an effect arising due to a disruption of the BBB, or due to specific binding to TSPO independent of a BBB disruption [172, 177, 179, 184]. Although an increased uptake could be observed even in regions without CE in T_1-weighted MRI images of gliomas [184], focal MS lesions [185], and in wide-spread lesions of progressive multifocal leukoencephalopathy (PML) [?], this might still be caused by subtle BBB changes resulting in a higher availability within the CNS (section 2.4.3). Another issue discussed in literature is, that differences between genotypes (LAB, MAB, HAB) cannot be observed in some studies and only very weakly effects are measured by others. However, it has been reported, that in vitro measurements by D. Owen (unpublished) revealed significant binding affinity differences between MABs and HABs (displacement of ^{3}H-PK11195 by cold GE-180). The low or vanishing differences observed for ^{18}F-GE-180 might be interpreted as evidence for the hypothesis, that the low brain uptake is not dominated by specific TSPO binding. However, a highly probable disagreement between in vitro and in vivo studies was reported previously [146, 186, 187]. One further conspicuous observation is, that both tracers (^{11}C-(R)-PK11195 and ^{18}F-GE-180) without striking differences between genotypes show a higher plasma fraction (approx. 1.5) compared to other 2nd generation tracers [179, 180]. Since, it could be shown recently, that ^{18}F-GE-180 uptake is significantly reduced by blocking with XBD173 [?], it is highly likely, that the observed signal in lesions is related to specific TSPO binding. The contribution of a BBB disintegration to maximal uptake in lesions needs to be further analysed in future studies using perfusion weighted imaging. Also, a comparison of uptake in inflammatory lesions measured with ^{18}F-GE-180 and with other TSPO tracers would be desirable.

Another matter of current debate is the applicability of reference tissue methods for TSPO tracers. Relevant objections have been raised [188, 189]. It is highly probable, that reference tissue requirements as listed in section 2.2.3 are violated in case of a disrupted BBB. Folkersma *et al.* [188] observed an increased variability of K_1/k_2 across the brain in early phase after traumatic brain injury, which is suspected to reflect BBB disruption. Depending on the severity of BBB disintegration, and the specific tracer properties it might be recommended to validate the applicability of reference tissue quantification with arterial sampling, in order to avoid biased BP (or DVR) estimates. Yet, under the assumption that the reference region is not affected by disease, one advantage of reference tissue utilisation is the inherent normalisation which has the potential to reduce

the variability caused e. g. by patient age, gender, or genotype.

3.4 Non-invasive glioma characterisation with voxel-based features, shape, and pharmacokinetic modelling parameters using ^{18}F-FET PET

3.4.1 Background

Glioma classification

According to the updated (2016) WHO guideline on the classification of tumours of the CNS, tumour classification is no longer based only on histology (phenotype), but particularly emphasises the relevance of molecular genetic information (genotype) [190, 191]. Several studies showed that gliomas with a mutation of the **isocitrate dehydrogenase (IDH)** gene (*IDH*-mut) have a better prognosis than *IDH*-wildtype (*IDH*-wt) gliomas [190, 192, 193]. *IDH*-mut gliomas can be sub-divided into gliomas which present with a 1p/19q co-deletion, i. e. a loss of the chromosome arms 1p and 19q, or without. Histological grades differentiate between low-grade gliomas (LGG, WHO grade II), and high-grade gliomas (HGG) comprising WHO grades III, and IV (glioblastoma, GBM).

It could be shown, that *IDH*-wt gliomas are predominantly associated with an increased angiogenesis. This could be detected e. g. as an elevation of relative cerebral blood volume (rCBV) compared to healthy tissue derived with perfusion weighted MR imaging (PWI). On the contrary, *IDH*-mut gliomas presented with normal, or decreased rCBV when compared to healthy tissue [194, 195]. Similarly, relative tumour blood flow (rCBF) was found to be significantly elevated in *IDH*-wt compared to *IDH*-mut gliomas [196–198]. In aggressive gliomas the increased angiogenesis coincides with BBB disintegration as described in section 2.4.3. Due to the significantly reduced survival in gliomas with increased angiogenesis, several therapies have been developed, aiming to reduce endothelial growth factors [196].

Amino acid PET with ^{18}F-FET PET

As summarised by the response assessment in neuro-oncology (RANO) working group [199] amino acid PET with ^{18}F-FET is suspected to provide a superior diagnostic accuracy compared to MRI for glioma grading, detection of recurrence, assessment of treatment response, and prognosis. Up to now, several heuristic parameters (as presented in section 2.2.4) have shown clinical relevance [200–204].

While a clinical relevance has been proven, the underlying physiological processes and differences in tissue properties affecting dynamic ^{18}F-FET PET uptake in healthy and tumoural tissue are still under investigation. Until now, it could be shown that the fraction of ^{18}F-FET bound to plasma proteins is low, and that ^{18}F-FET has a high in-vivo stability and exhibits low uptake in inflammatory tissue [205, 206]. Since ^{18}F-FET is large, it is suspected to be transferred via specific amino acid transporters (AAT), such as the system L. The exact mechanisms are however still controversially discussed [207–211]. For rats with implanted human glioblastoma cells no significant difference in TBR and late slope could be found before and after a therapeutic reduction of BBB permeability [212] .

Outline

In addition to the published voxel-based percentage volume histogram data (chapter 5), here the results obtained for further histogram, shape, texture, and pharmacokinetic modelling parameters are presented (section 2.3.4). For all parameters the ability to differentiate *IDH*-wt from *IDH*-mut gliomas, and HGG from LGG gliomas was assessed. Additionally, a preliminary attempt was made to perform pharmacokinetic modelling, in order to improve the understanding of the established heuristic parameters.

3.4.2   Material and methods

Patients and imaging

Dynamic ^{18}F-FET PET scans of 162 newly diagnosed glioma patients were included in this study. The details on patient characteristics and imaging properties can be found in the methods section of the second publication attached in this thesis (chapter 5) [213].

VOI delineation

Although a delineation of biological tumour volumes (BTV) based only on activity concentration in surrounding tissue (BG) has proven to be unfavourable for the delineation of true object boundaries (section 3.2.3), this is the commonly applied and established method, which has been validated with stereotactic biopsies by Pauleit *et al.* [151]. In that study, a TBR threshold of 1.6 yielded optimal sensitivity and specificity for distinguishing tumoural from healthy tissue in static 15-40 min p.i. images. Albert *et al.* [203] showed that late 20-40 min p.i. scans are less suitable for glioma grading than early static scans. Hence, static 20-40 min p.i. scans were utilised for tumour delineation, assuming to yield reliable BTV estimates independent of glioma grade. For the VOI-based extraction of TTP and Slope$_{15-40}$, additionally a 90% isocontour was applied on static 10-30 min p.i. images [202].

Extraction of histogram, texture, and shape parameters

All parameters were extracted automatically with an in-house developed software which is written within the ROOT data analysis framework (version 6.09/01, Cern, Switzerland), and includes algorithms provided by the ITK segmentation and registration toolkit (version 4.11, National Library of Medicine). Histogram and texture analysis was performed on TTP, Slope$_{15-40}$, TBR$_{5-15}$, TBR$_{10-30}$, and TBR$_{20-40}$ images. For this, the intensity values were discretised with a fixed bin size. In contrast to a fixed number of bins per volume, this has shown to provide a superior inter- and intra-patient comparability of the extracted parameters [104,105]. The chosen fixed bin width for TBR data was 0.05, for TTP 1 min, and for Slope$_{15-40}$ the bin width was set to 0.12 SUV/h.

The definitions of the applied histogram, texture, and shape features can be found in section 2.3.4. In addition to the standard deviation of enclosed intensity values, the following parameters were extracted from histogram data (ROOT class TH1 [214]): PVH, skewness, kurtosis, uniformity, and entropy. Feature extraction based on the grey level co-occurrence matrix in ITK (class: "HistogramToTextureFeaturesFilter" [215]) provided the following parameters: energy, entropy, correlation, inverse difference moment, inertia, cluster shade, cluster prominence, and Haralick's correlation. The follow-

ing shape parameters were obtained (ITK class "ShapeLabelObject" [216]): elongation, roundness, equal sphere radius, flatness, mesh volume, and mesh area.

Pharmacokinetic modelling

Since no blood sampling was performed during dynamic ^{18}F-FET PET scans in this retrospective study, pharmacokinetic modelling had to rely on a whole blood IDIF without the application of re-scaling, or correction for plasma-to-blood ratio and metabolites. Previous studies indicate, that the plasma-to-whole blood ratio is constant and parent fraction decreases very slowly during the scan duration [205]. The influence of metabolite correction on reference tissue-based DVRs has shown to be negligible [217]. Average tissue TACs were extracted from the BTV. The FOV of the dynamic PET images acquired for this study was too small for a reliable IDIF extraction from the carotid arteries. Therefore, the VOI was placed in the sinus sagittalis superior. The "4 hottest pixels per plane method" [53] was applied for the definition of the blood VOI, and compared to an 55% iso-contour. 20 consecutive planes were included starting from the confluens sinuum.

The following compartmental models were included: 1- and 2-tissue compartment models (equations (2.28) to (2.30)) with and without the inclusion of a blood volume fraction V_b (equation (2.18)). In addition to the reversible 2TC model (2TC4k), also an irreversible (2TC3k) model, linear models with blood input (section 2.2.2), or reference tissue input (section 2.2.3) were evaluated.

Fitting of the model equations was performed by minimising the WRSS as defined in equation (2.20) within the ROOT framework (class "TGraphErrors" and Minuit minimizer). The frame weights in this study were set to $w_f = \frac{1}{\Delta t_f}$, enabling an equal weighting of each time point, i.e. independence from the frame lengths Δt_f. Compartmental models with blood input were compared using the corrected Akaike information criterion (equation (2.19)).

Statistical analysis

The ability to differentiate molecular genetic and histologic glioma grades was assessed using the areas under the curve (AUC) of receiver-operating characteristics (ROC) analysis, and the p-values and effect sizes derived from Mann-Whitney U-test. The effect size was defined as $r = |\text{test statistic}|/\text{sample size}$.

3.4.3 Results

Differentiation of glioma grades

Tables 3.4 to 3.7 summarise the results obtained with conventional heuristic VOI-based parameters (section 2.2.4), published voxel-based percentage volume histogram data, and additionally results obtained for further histogram, shape, texture, and pharmacokinetic modelling parameters. The highest AUCs for the identification of *IDH*-wt gliomas were found for PVH$_{\text{Slope},15-40<0}$, PVH$_{\text{TTP}<20}$, net influx rates (K_i, and $K_i/V_{T,Ref}$) from Patlak GA, and intercepts of GA. The highest AUC for distinguishing HGG from LGG was found for PVH$_{\text{TBR},5-15>2}$. Shape parameters yielded low AUC values, with best results for lesion size related parameters (equal sphere radius, volume and mesh surface area). Texture features derived from different parametric maps tended to provide the highest

AUC values for features from TTP and TBR_{5-15} maps. For example homogeneity of TBR_{5-15} values decreased with increasing aggressiveness.

		IDHwt from IDHmut			HGG from LGG			Median				
		AUC	U-test, p	effect	AUC	U-test, p	effect	BG	IDHmut	IDHwt	LGG	HGG
90% isocontour	TTP (min)	0.75	0.000	0.44	0.72	0.000	0.38	35	25	17	25	17
	$Slope_{15\text{-}40}$ (SUV/h)	0.75	0.000	0.44	0.71	0.000	0.35	0.25	-0.01	-1.04	0.02	-0.77
Conventional BTV data	TTP (min)	0.77	0.000	0.49	0.73	0.000	0.39	35	35	25	35	25
	$Slope_{15\text{-}40}$ (SUV/h)	0.82	0.000	0.55	0.77	0.000	0.45	0.24	0.56	-0.13	0.57	0.05
	$TBR_{5\text{-}15,max}$	0.71	0.000	0.37	0.77	0.000	0.44	1.53	2.78	4.03	2.65	3.90
	$TBR_{5\text{-}15}$	0.76	0.000	0.45	0.80	0.000	0.50	1.00	1.82	2.36	1.76	2.30
	$TBR_{20\text{-}40,max}$	0.61	0.016	0.19	0.71	0.000	0.34	1.39	2.70	3.28	2.56	3.36
	$TBR_{20\text{-}40}$	0.60	0.023	0.18	0.72	0.000	0.35	1.00	1.92	2.05	1.86	2.06
	$SUV_{20\text{-}40}$	0.59	0.052	0.15	0.62	0.010	0.20	1.02	1.91	2.09	1.96	2.15

Table 3.4: Results of conventional VOI-based parameters. Areas under the ROC curve (AUC), and U-test p-values and effect sizes are presented for distinguishing *IDH*wt from *IDH*mut gliomas, and HGG from LGG. AUC values are shown colour-coded (white-yellow-red continuously scaled from AUC= 0.5 to AUC= 0.8). Median parameter values of healthy background tissue (BG), and molecular genetic, and histologic glioma groups are given on the right.

		IDHwt from IDHmut			HGG from LGG			Median				
		AUC	U-test, p	effect	AUC	U-test, p	effect	BG	IDHmut	IDHwt	LGG	HGG
PVH	TTP < 20	0.83	0.000	0.58	0.79	0.000	0.47	0.43	0.21	0.59	0.19	0.50
	$Slope_{15\text{-}40}$ < 0	0.84	0.000	0.58	0.78	0.000	0.45	0.07	0.22	0.56	0.21	0.47
	$TBR_{5\text{-}15}$ > 2	0.80	0.000	0.52	0.82	0.000	0.53	0.00	0.28	0.69	0.19	0.66
	$TBR_{20\text{-}40}$ > 2	0.60	0.022	0.18	0.72	0.000	0.35	0.00	0.31	0.45	0.23	0.46
Skewness	TTP	0.83	0.000	0.58	0.75	0.000	0.42	-0.25	-0.69	0.27	-0.75	0.07
	$Slope_{15\text{-}40}$	0.47	0.551	0.05	0.62	0.012	0.20	0.00	-0.09	-0.04	0.02	-0.09
	$TBR_{5\text{-}15}$	0.56	0.176	0.11	0.59	0.067	0.14	-0.17	0.41	0.51	0.42	0.51
	$TBR_{10\text{-}30}$	0.58	0.077	0.14	0.60	0.038	0.16	-0.22	0.52	0.60	0.52	0.60
	$TBR_{20\text{-}40}$	0.54	0.435	0.06	0.46	0.355	0.07	-0.20	0.88	0.92	0.92	0.88
Kurtosis	TTP	0.56	0.214	0.10	0.58	0.080	0.14	-1.04	-0.57	-0.73	-0.48	-0.69
	$Slope_{15\text{-}40}$	0.45	0.300	0.08	0.57	0.172	0.11	0.04	0.09	0.00	0.07	0.05
	$TBR_{5\text{-}15}$	0.45	0.269	0.09	0.44	0.206	0.10	0.06	0.01	-0.19	-0.01	-0.16
	$TBR_{10\text{-}30}$	0.50	0.987	0.00	0.46	0.403	0.07	0.09	-0.09	-0.11	-0.11	-0.10
	$TBR_{20\text{-}40}$	0.54	0.373	0.07	0.46	0.411	0.06	0.15	-0.06	0.18	0.20	0.05
Standard deviation	TTP	0.59	0.047	0.16	0.66	0.001	0.26	9.80	8.02	8.44	7.80	8.43
	$Slope_{15\text{-}40}$	0.64	0.003	0.23	0.69	0.000	0.31	0.63	0.80	0.93	0.76	0.93
	$TBR_{5\text{-}15}$	0.70	0.000	0.34	0.76	0.000	0.43	0.17	0.32	0.55	0.25	0.53
	$TBR_{10\text{-}30}$	0.66	0.001	0.27	0.75	0.000	0.40	0.14	0.28	0.44	0.23	0.44
	$TBR_{20\text{-}40}$	0.61	0.019	0.18	0.71	0.000	0.35	0.13	0.24	0.36	0.21	0.39
Uniformity	TTP	0.79	0.000	0.51	0.77	0.000	0.44	0.23	0.36	0.24	0.36	0.25
	$Slope_{15\text{-}40}$	0.65	0.001	0.25	0.71	0.000	0.34	0.05	0.04	0.04	0.05	0.04
	$TBR_{5\text{-}15}$	0.71	0.000	0.36	0.78	0.000	0.46	0.08	0.04	0.03	0.06	0.03
	$TBR_{10\text{-}30}$	0.67	0.000	0.29	0.76	0.000	0.42	0.10	0.05	0.03	0.06	0.04
	$TBR_{20\text{-}40}$	0.60	0.023	0.18	0.71	0.000	0.35	0.11	0.07	0.05	0.09	0.05
Entropy	TTP	0.79	0.000	0.50	0.77	0.000	0.44	2.29	1.77	2.28	1.67	2.17
	$Slope_{15\text{-}40}$	0.64	0.002	0.25	0.71	0.000	0.34	4.43	4.73	4.97	4.67	4.95
	$TBR_{5\text{-}15}$	0.70	0.000	0.35	0.77	0.000	0.44	3.81	4.65	5.34	4.36	5.30
	$TBR_{10\text{-}30}$	0.66	0.000	0.28	0.75	0.000	0.41	3.52	4.45	5.05	4.21	5.02
	$TBR_{20\text{-}40}$	0.60	0.022	0.18	0.72	0.000	0.36	3.38	3.96	4.53	3.69	4.57

Table 3.5: Results of histogram-based parameters. Data are presented as described for table 3.4.

		IDHwt from IDHmut			HGG from LGG			Median				
		AUC	U-test, p	effect	AUC	U-test, p	effect	BG	IDHmut	IDHwt	LGG	HGG
GLCM Energy	TTP	0.79	0.000	0.50	0.76	0.000	0.43	0.076	0.178	0.087	0.199	0.097
	Slope$_{15-40}$	0.64	0.003	0.24	0.71	0.000	0.35	0.004	0.003	0.002	0.004	0.002
	TBR$_{5-15}$	0.71	0.000	0.36	0.79	0.000	0.47	0.014	0.006	0.002	0.007	0.002
	TBR$_{10-30}$	0.67	0.000	0.30	0.76	0.000	0.43	0.019	0.005	0.002	0.008	0.003
	TBR$_{20-40}$	0.62	0.007	0.21	0.73	0.000	0.37	0.020	0.007	0.003	0.011	0.004
GLCM Entropy	TTP	0.79	0.000	0.50	0.77	0.000	0.44	4.34	3.18	4.12	3.05	3.96
	Slope$_{15-40}$	0.63	0.004	0.23	0.70	0.000	0.33	8.41	8.59	9.06	8.49	9.01
	TBR$_{5-15}$	0.70	0.000	0.34	0.78	0.000	0.46	6.58	7.81	9.20	7.57	9.14
	TBR$_{10-30}$	0.67	0.000	0.29	0.76	0.000	0.42	6.20	7.79	9.01	7.38	8.86
	TBR$_{20-40}$	0.62	0.006	0.21	0.73	0.000	0.37	6.12	7.49	8.58	7.01	8.59
GLCM Correlation	TTP	0.53	0.548	0.05	0.53	0.469	0.06	0.003	0.006	0.006	0.006	0.006
	Slope$_{15-40}$	0.62	0.010	0.20	0.63	0.009	0.21	0.020	0.014	0.010	0.013	0.011
	TBR$_{5-15}$	0.72	0.000	0.38	0.77	0.000	0.43	0.083	0.024	0.008	0.033	0.009
	TBR$_{10-30}$	0.68	0.000	0.30	0.73	0.000	0.38	0.107	0.022	0.009	0.035	0.009
	TBR$_{20-40}$	0.59	0.040	0.16	0.68	0.000	0.29	0.114	0.021	0.011	0.036	0.011
GLCM inverse difference moment (Homogeneity)	TTP	0.77	0.000	0.46	0.74	0.000	0.39	0.47	0.58	0.50	0.59	0.52
	Slope$_{15-40}$	0.61	0.015	0.19	0.60	0.036	0.16	0.23	0.19	0.18	0.19	0.18
	TBR$_{5-15}$	0.76	0.000	0.44	0.78	0.000	0.45	0.41	0.27	0.18	0.30	0.19
	TBR$_{10-30}$	0.72	0.000	0.38	0.75	0.000	0.41	0.46	0.27	0.19	0.30	0.20
	TBR$_{20-40}$	0.65	0.001	0.26	0.71	0.000	0.35	0.47	0.29	0.22	0.31	0.22
GLCM inertia (Contrast)	TTP	0.57	0.114	0.12	0.60	0.030	0.17	128.2	70.9	77.6	67.2	77.1
	Slope$_{15-40}$	0.61	0.013	0.19	0.63	0.009	0.20	24.3	35.7	44.2	36.4	42.6
	TBR$_{5-15}$	0.74	0.000	0.42	0.77	0.000	0.45	5.3	18.1	46.2	11.7	40.7
	TBR$_{10-30}$	0.71	0.000	0.36	0.75	0.000	0.41	3.7	16.8	39.7	11.4	37.0
	TBR$_{20-40}$	0.65	0.001	0.27	0.72	0.000	0.36	3.5	16.1	32.7	11.7	32.4
GLCM cluster shade	TTP	0.82	0.000	0.56	0.70	0.000	0.33	-626	-950	769	-858	315
	Slope$_{15-40}$	0.51	0.896	0.01	0.37	0.009	0.21	-9	-111	-62	41	-219
	TBR$_{5-15}$	0.64	0.002	0.24	0.70	0.000	0.32	-23	343	1957	188	1779
	TBR$_{10-30}$	0.64	0.002	0.25	0.72	0.000	0.35	-19	312	1610	208	1596
	TBR$_{20-40}$	0.62	0.009	0.21	0.71	0.000	0.34	-14	424	1749	310	1929
GLCM cluster prominence	TTP	0.60	0.027	0.17	0.68	0.000	0.29	132917	74293	92995	62106	93387
	Slope$_{15-40}$	0.64	0.003	0.24	0.71	0.000	0.34	20674	58584	104737	49573	101977
	TBR$_{5-15}$	0.70	0.000	0.34	0.76	0.000	0.43	2218	24644	250270	17402	232688
	TBR$_{10-30}$	0.66	0.000	0.28	0.74	0.000	0.40	1516	24997	195578	12181	174613
	TBR$_{20-40}$	0.62	0.009	0.21	0.72	0.000	0.36	1432	16953	124661	8842	133449
GLCM Haralick correlation	TTP	0.56	0.158	0.11	0.43	0.135	0.12	55705	49454	42843	47459	48603
	Slope$_{15-40}$	0.63	0.004	0.23	0.71	0.000	0.35	432849	1023555	2183645	786412	1946540
	TBR$_{5-15}$	0.72	0.000	0.38	0.79	0.000	0.47	39758	298573	3036900	169246	2227860
	TBR$_{10-30}$	0.68	0.000	0.30	0.76	0.000	0.42	27776	242184	1640760	106531	1439010
	TBR$_{20-40}$	0.62	0.009	0.20	0.72	0.000	0.36	26574	85512	425472	31906	418567
Shape	Elongation	0.45	0.247	0.09	0.44	0.237	0.09	3.55	1.32	1.29	1.37	1.29
	Roundness	0.56	0.188	0.10	0.58	0.103	0.13	0.51	0.79	0.76	0.78	0.76
	Equal sphere radius	0.56	0.188	0.10	0.68	0.000	0.29	19.6	15.1	16.2	12.7	16.9
	Flatness	0.61	0.014	0.19	0.53	0.516	0.05	2.22	1.29	1.22	1.27	1.27
	Volume (mL)	0.56	0.188	0.10	0.68	0.000	0.29	31.8	14.3	17.7	8.5	20.0
	Mesh area (cm²)	0.57	0.104	0.13	0.68	0.000	0.29	91.7	38.3	48.7	24.5	49.4

Table 3.6: Results of GLCM-based texture features, and shape parameters. Data are presented as described for table 3.4.

		IDHwt from IDHmut			. HGG from LGG			. Median				.
		AUC	U-test, p	effect	AUC	U-test, p	effect	BG	IDHmut	IDHwt	LGG	HGG
V_T	1TC-V_B	0.49	0.786	0.02	0.55	0.344	0.07	0.58	1.38	1.38	1.36	1.44
	2TC4k-V_B	0.58	0.084	0.14	0.49	0.811	0.02	0.66	1.48	1.39	1.43	1.46
	Logan	0.47	0.475	0.06	0.53	0.570	0.04	0.63	1.31	1.27	1.29	1.31
	RE	0.58	0.090	0.13	0.64	0.004	0.23	0.57	1.11	1.21	1.09	1.22
DVR	1TC-V_B	0.49	0.867	0.01	0.63	0.007	0.21	1.00	2.31	2.33	2.24	2.39
	2TC4k-V_B	0.43	0.138	0.12	0.59	0.060	0.15	1.00	2.26	2.13	2.14	2.22
	Logan Reference	0.58	0.090	0.13	0.65	0.001	0.25	1.00	1.95	2.05	1.89	2.06
	RE Reference	0.63	0.004	0.23	0.73	0.000	0.38	1.00	1.91	2.08	1.86	2.08
Patlak	Blood input K_I	0.83	0.000	0.57	0.73	0.000	0.38	0.55	1.19	0.65	1.19	0.79
	Reference K_I/V_{TRef}	0.83	0.000	0.57	0.76	0.000	0.43	0.00	0.19	-1.14	0.40	-0.86
V_B	1TC-V_B	0.61	0.012	0.20	0.65	0.002	0.24	0.13	0.19	0.22	0.18	0.22
	2TC4k-V_B	0.63	0.005	0.22	0.70	0.000	0.32	0.09	0.13	0.16	0.12	0.16
1TC-V_B	K_1	0.73	0.000	0.40	0.75	0.000	0.40	0.04	0.09	0.15	0.08	0.14
	k_2	0.79	0.000	0.50	0.76	0.000	0.43	0.07	0.07	0.11	0.07	0.10
2TC4k-V_B	K_1	0.67	0.000	0.29	0.57	0.169	0.11	0.15	0.22	0.34	0.24	0.27
	k_2	0.59	0.043	0.16	0.42	0.095	0.13	0.96	0.54	0.65	0.67	0.55
	k_3	0.56	0.189	0.10	0.40	0.036	0.16	0.17	0.15	0.16	0.18	0.15
	k_4	0.75	0.000	0.43	0.74	0.000	0.39	0.06	0.06	0.10	0.06	0.09
	V_{ND}	0.58	0.070	0.14	0.71	0.000	0.35	0.18	0.45	0.55	0.41	0.56
	BP_{ND}	0.65	0.001	0.26	0.76	0.000	0.42	2.63	2.26	1.59	2.70	1.65
GA blood input intercepts	Logan	0.77	0.000	0.47	0.77	0.000	0.44	-11.13	-12.50	-7.75	-13.60	-9.06
	RE	0.66	0.000	0.27	0.61	0.022	0.18	-4.57	-10.08	-8.35	-10.15	-8.88
	Patlak	0.73	0.000	0.41	0.76	0.000	0.42	0.41	0.77	1.06	0.74	1.04
GA reference input intercepts	Logan	0.84	0.000	0.58	0.80	0.000	0.49	-6.67	-7.99	-4.81	-8.36	-5.45
	RE	0.86	0.000	0.62	0.79	0.000	0.47	0.00	-2.13	2.27	-2.56	1.49
	Patlak	0.76	0.000	0.45	0.79	0.000	0.48	1.00	1.85	2.43	1.78	2.38

Table 3.7: Results of pharmacokinetic modelling parameters. Data are presented as described for table 3.4.

Pharmacokinetic modelling

AIC_C values were comparable for the application of an IDIF derived from 4 hottest voxels per plane and the IDIF obtained with the $55\% \cdot I_{max}$ iso-contour, with slightly lower values for the "4 hottest voxels" method [53]. In 60% of tumour TACs, and 54% of BG TACs the 2TC4k-V_B model was preferred, followed by 2TC4k (20%, 23%), 1TC-V_B (8%, 6%), 2TC3k-V_B (7%, 6%), 2TC3k (4%, 11%), and 1TC (0%, 0%).

Modelling results and AUC values of average VOI TACs are given in table 3.7. For comparison, the data for conventional heuristic parameters are given in table 3.4. The distribution volumes V_T were significantly elevated in tumour tissue compared to BG ($p < 0.001$). However, V_T and V_T ratios (DVR, section 2.2.3) showed only partly significant differences between grades, and revealed low AUC values. The following parameters increased with glioma grade: K_1, V_B, V_{ND}, TBR_{5-15}, and TBR_{20-40}. A reduction with glioma grade was found for: $Slope_{15-40}$, and TTP. Moreover, k_2 form 1TC-V_B, and k_4 from 2TCk4-V_B allowed for an identification of *IDH*-wt, and HGG gliomas, and revealed comparable values in *IDH*-mut/ LGG gliomas and BG.

		TTP	Slope$_{15\text{-}40}$	TBR$_{5\text{-}15}$	TBR$_{20\text{-}40}$	SUV$_{20\text{-}40}$
V_T	1TC-V_B	0.00	-0.11	-0.01	-0.04	0.01
	1TC	-0.02	0.02	0.45	0.58	0.69
	2TC4k-V_B	0.00	-0.11	-0.01	-0.04	0.01
	2TC4k	0.20	0.26	0.11	0.31	0.50
	Logan	0.07	0.13	0.37	0.55	0.67
	RE	-0.18	-0.20	0.61	0.64	0.69
DVR	1TC-V_B	0.00	-0.11	-0.01	-0.04	0.01
	1TC	-0.11	-0.16	0.75	0.97	0.55
	2TC4k-V_B	0.00	-0.16	0.02	-0.06	-0.04
	2TC4k	0.07	0.12	0.33	0.60	0.28
	Logan Reference	-0.14	-0.19	0.61	0.75	0.46
	RE Reference	-0.21	-0.33	0.86	1.00	0.58
Patlak	Blood input K$_i$	0.73	0.87	-0.52	-0.06	0.03
	Reference K$_i$/V'$_{TRef}$	0.72	0.89	-0.73	-0.28	-0.26
V_B	1TC-V_B	-0.21	-0.24	0.22	0.13	0.11
	2TC4k-V_B	-0.28	-0.31	0.23	0.07	0.05
1TC-V_B	K$_1$	-0.56	-0.54	0.57	0.30	0.29
	k$_2$	-0.65	-0.65	0.49	0.09	0.08
2TC4k-V_B	K$_1$	-0.38	-0.34	0.33	0.17	0.18
	k$_2$	-0.16	-0.03	-0.06	-0.14	-0.10
	k$_3$	-0.20	-0.16	0.09	0.00	-0.01
	k$_4$	-0.47	-0.46	0.31	0.01	-0.01
	V$_{ND}$	0.00	-0.11	-0.01	-0.04	0.01
	BP$_{ND}$	0.00	-0.11	-0.02	-0.05	0.01
GA blood input intercepts	Logan	-0.58	-0.66	0.56	0.24	0.14
	RE	-0.43	-0.41	-0.04	-0.40	-0.44
	Patlak	-0.55	-0.65	0.79	0.58	-0.03
GA reference input intercepts	Logan	-0.58	-0.71	0.70	0.36	0.20
	RE	-0.78	-0.81	0.68	0.17	0.20
	Patlak	-0.56	-0.73	0.97	0.79	0.52

Table 3.8: Correlation of conventional heuristic parameters (table 3.4) with pharmacokinetic modelling parameters (table 3.7) using Pearson's correlation coefficients r. Values are shown colour-coded (white-yellow-red continuously scaled from $|r| = 0$ to $|r| = 0.9$).

Results obtained for the correlation of heuristic parameters with pharmacokinetic modelling parameters are presented in table 3.8. Parameters from static images were mainly related to V_T or DVR. The correlation between SUV$_{20-40}$ and V_T, and between TBR$_{20-40}$ and DVR was most pronounced for 1TC model, Logan, and RE GA, however not for compartmental models with an inclusion of V_B. On the contrary, an early peak or negative Slope$_{15-40}$ were associated with an elevated K_1, k_2 from 1TC-V_B, k_4 from 2TC4k-V_B, and V_B. An increasing kinetic with late peak was associated with an elevated net uptake rate K_i.

For visual comparison parametric 3D distributions are exemplarily shown for three glioma patients (figures 3.7 and 3.8). The first patient (a) presented with a typical *IDH*-wt HGG, the second (b) with an *IDH*-mut LGG, and the last (c) with a glioma exhibiting a heterogeneous parameter distribution. As expected from VOI-TAC analysis, a comparison of parametric images from 1TC-V_B (figure 3.8) revealed high intensity differences between grades for K_1, k_2, and V_B, but not for V_T. Also, a high spatial correlation of Slope$_{15-40}$ and K_i/V'_T from Patlak reference tissue model was found.
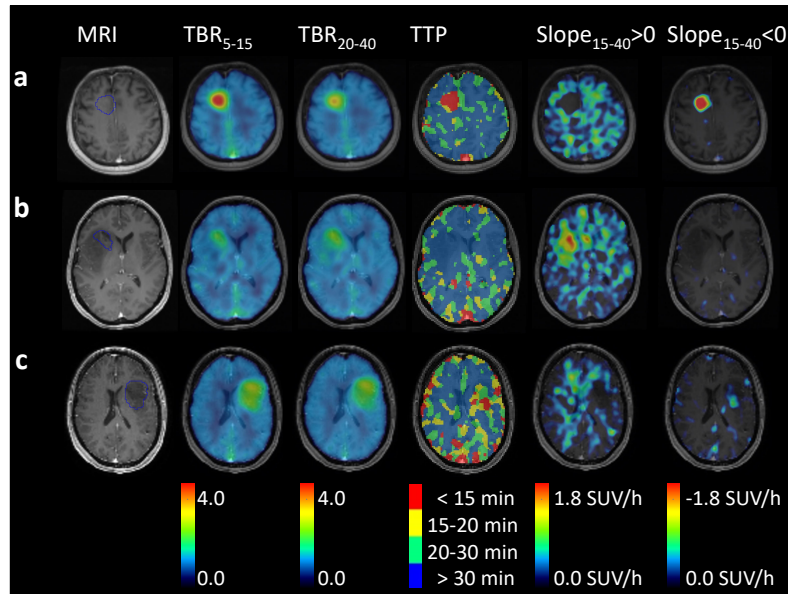
Figure 3.7: Heuristic parameter maps as applied for PVH-based analysis (chapter 5). Dynamic PET data were smoothed frame-wise with a spatial Gaussian filter (10 mm FWHM) before parameter estimation. From left to right: CE MRI, TBR_{5-15}, TBR_{20-40}, TTP, positive, and negative $Slope_{15-40}$. **a** Typical *IDH*-wt HGG, **b** typical *IDH*-mut LGG, and **c** exemplary IDH-mut codel LGG glioma with heterogeneous parameter distributions, where the hottest volume in static TBR images did not co-localise with the hot-spots in the TTP map and in the image with negative $Slope_{15-40}$.
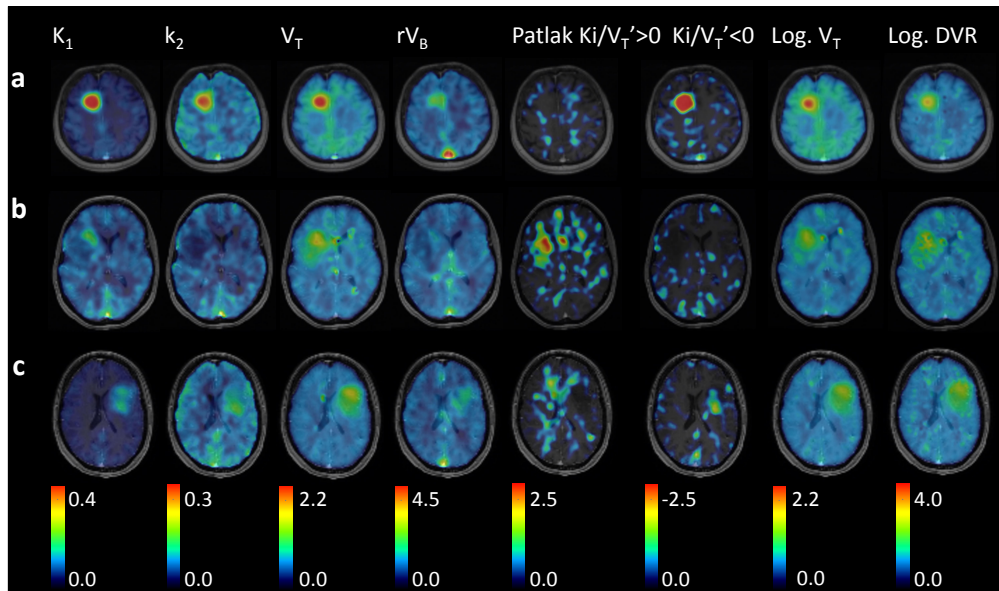
Figure 3.8: Parametric maps derived with pharmacokinetic modelling. Dynamic PET data were smoothed frame-wise with a spatial Gaussian filter (10 mm FWHM). From left to right: K_1, k_2, V_T, and V_B relative to background from 1TC-V_B model; Patlak K_i/V_T' (positive and negative); V_T and DVR from Logan GA. Patients **a, b, c** and images slices are the same as presented in figure 3.7.

3.4.4   Discussion

In general, TTP- and Slope$_{15-40}$-based parameters yielded the highest AUC values for distinguishing molecular genetic groups, and static TBR-based parameters for distinguishing histological groups. Best performance was observed for PVH values quantifying heuristic parameter fractions, and for parameters derived with GA. Within texture features, the best results were obtained from TTP and TBR$_{5-15}$ maps. Although the 2TC4k-V_B model was predominantly preferred in tumours and healthy tissue (Akaike), the derived modelling parameters revealed only a moderate relevance for glioma grading. The highest relevance for a differentiation of glioma grades with pharmacokinetic models was found for K_1, k_2 from 1TC-V_B model, k_4 from 2TC4k-V_B model, parameters from Patlak plots, and intercepts of graphical methods. Since V_T values were significantly elevated compared to healthy tissue, while glioma groups were indistinguishable, it might be preferable to perform tumour segmentation in DVR images or TBR images derived from later static scans [217]. In order to further improve the performance for distinguishing glioma grades, e. g. the micro-parameters from kinetic modelling might be normalised to healthy tissue values. Moreover, after a pre-selection of relevant VOI features (e. g. best results in univariate analysis and low correlation between parameters), machine learning might be employed for multivariate glioma classification.

A correlation of static SUV and TBR parameters with V_T and DVR was only found for compartmental models not taking into account an additional blood-volume fraction. TTP and Slope$_{15-40}$ were predominantly related to the transfer rate from blood to tissue K_1, efflux rate k_2 from 1TC-V_B, k_4 from 2TC-V_B, blood volume fraction V_B, and net influx rates K_i and K_i/V_T'. As visualised in figures 3.7 and 3.8, a high spatial correlation of positive and negative Slope$_{15-40}$ with K_i/V_T' from Patlak reference tissue model was found. When both parameters are extracted from the same time interval, Ki/V_T' derived from equation (2.36) can be interpreted as slope of the tissue TAC depending on the cumulated counts in reference tissue, thus most probably providing a higher inter- and intra-subject comparability. Interestingly, in case of the heterogeneous glioma the identified sub-volume with early peak and negative slope did co-localise with the hottest volumes in K_1 and k_2 images from 1TC-V_B model, but not with hot-spots in static and V_T images. Another interesting observation was, that a fraction of the area with decreased signal in CE T$_1$-weighted MRI of the *IDH*-mut LGG (figures 3.7 and 3.8b) could not be detected in static TBR images, but V_T values from 1TC-V_B revealed an elevated signal compared to BG. This might indicate, that later static images potentially provide a better correspondence to V_T images from compartmental modelling, as previously stated by Koopman *et al.* [217].

The observed differences in K_1 (equation (2.23)), and V_B might be partly related to the described different angiogenic properties of *IDH*-mut and *IDH*-wt gliomas. In line with our expectations, Göttler *et al.* [218] showed that the correlation with peak rCBV values from PWI was higher for Slope$_{10-30}$ and early ^{18}F-FET uptake (SUV$_{10-20}$) compared to late uptake (SUV$_{30-40}$). Moreover, a significant correlation of CBF with ^{18}F-FET uptake was found [217, 219]. In the next steps e. g. information on blood flow and PS from PWI might be linked to K_1 according to equation (2.23), and inserted in compartmental models using continuous blood sampling. Furthermore, the estimation of V_{ND} from blocking experiments would be desirable.

In summary, this study suggests, that the application of parametric images is of high relevance for the identification of aggressive sub-volumes and tumour heterogeneity. The

next steps will include parameter selection and model estimation for glioma grading or prediction of e. g. recurrence and survival. Moreover, multi-parametric (and multi-modal) data might be utilised for a voxel-wise generation of membership-maps for glioma classification or of probability maps for the prediction of e. g. tumour recurrence [220].

3.5 Conclusions and outlook

The investigated segmentation, feature extraction, and modelling approaches applied on dynamic brain PET images of specific tracers have the potential to significantly support the characterisation of brain pathology, and an application in clinical routine appears to be feasible. The next steps should aim to improve the understanding of the underlying physiologic properties and a validation of methodology. This might include the utilisation of pharmacokinetic models as an input for the simulation of activity distributions, and a subsequent validation of methodology by simulating dynamic PET images either with analytical, or Monte Carlo methods as implemented e.g. in the GATE simulation toolkit [221]. Such simulation studies may also be applied for an elaborate assessment of different voxel-based partial volume effect correction techniques (section 2.1.5) and reconstruction algorithms, e.g. evaluating the influence on parameter estimation. Also, the noise-properties of different reconstruction algorithms should be incorporated in order to assess the influence of TAC-noise on voxel-wise parameter estimation. With respect to this, it becomes highly desirable to implement and test strategies aiming to reduce noise influence, e.g. by taking into account a spatio-temporal connectedness of voxels [222]. This forms the basis for further elaborate analysis utilising machine learning for non-invasive assessment of heterogeneity, or a 3D prediction of lesion recurrence. Such information is of high clinical interest, supporting e.g. planning of glioma biopsy, surgery, or radiation therapy. Moreover, in case of diffuse neuroinflammation or neurodegeneration, a further evaluation of machine learning methods might refine the proposed method for the definition of voxels unaffected by disease.
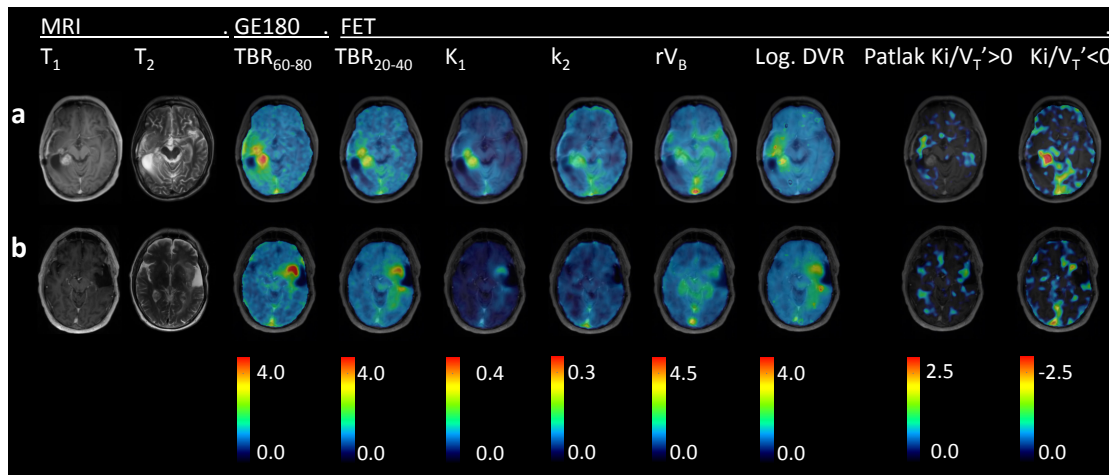
Figure 3.9: Two exemplary *IDH*-mut HGG gliomas (patient **a** and **b**) scanned with contrast-enhanced MRI, ^{18}F-GE-180 PET, and ^{18}F-FET PET. From left to right: CE T_1-weighted MRI, T_2-weighted MRI, static TBR_{60-90} from ^{18}F-GE-180 PET, and parametric images from ^{18}F-FET PET: static TBR_{20-40}, K_1 and k_2 from 1TC-V_B, DVR from Logan reference tissue model, and positive and negative K_i/V_T' from Patlak reference tissue model.

In order to provide a robust prediction model for glioma patients, our group currently combines information from multi-modal data, i.e. TSPO PET, amino acid PET, and contrast enhanced MRI. The three modalities have been found to provide complementary information [184, 223]. Two exemplary *IDH*-mut HGG patients, which were scanned

with all three modalities, are shown in figure 3.9. While static TBR_{20-40} from ^{18}F-FET PET revealed two hot-spots with similar uptake for patient (a), the lower hot-spot was more pronounced in ^{18}F-GE-180 PET and exhibited negative K_i/V'_T (Patlak reference tissue model) and contrast-enhancement in T_1-weighted MRI. The upper hot-spot revealed positive K_i/V'_T values and a lower signal in CE MRI. The second example glioma (b) revealed reduced signal in CE MRI, one hot-spot in ^{18}F-GE-180 PET, two hot-spots in static ^{18}F-FET PET, and a heterogeneous distribution of K_i/V'_T values. A further incorporation of parametric information from perfusion weighted imaging and a comparison to micro-parameters as measured with PET is desirable.

Publications

Chapter 4

Publication I

TSPO imaging using the novel PET ligand [^{18}F]GE-180: quantification approaches in patients with multiple sclerosis

Lena Vomacka[1*] , Nathalie Lisa Albert[1,5], Simon Lindner[1], Marcus Unterrainer[1], Christoph Mahler[2], Matthias Brendel[1], Larissa Ermoschkin[1], Astrid Gosewisch[1], Anika Brunegraf[1], Christopher Buckley[3], Tania Kümpfel[2], Rainer Rupprecht[4], Sibylle Ziegler[1], Martin Kerschensteiner[2,5], Peter Bartenstein[1,5] and Guido Böning[1]

Abstract

Background: PET ligands targeting the translocator protein (TSPO) represent promising tools to visualise neuroinflammation. Here, we analysed parameters obtained in dynamic and static PET images using the novel TSPO ligand [^{18}F]GE-180 in patients with relapsing remitting multiple sclerosis (RRMS) and an approach for semi-quantitative assessment of this disease in clinical routine.

Seventeen dynamic [^{18}F]GE-180 PET scans of RRMS patients were evaluated (90 min). A pseudo-reference region (PRR) was defined after identification of the least disease-affected brain area by voxel-based comparison with six healthy controls (HC) and upon exclusion of voxels suspected of being affected in static 60–90 min p.i. images. Standardised uptake value ratios (SUVR) obtained from static images normalised to PRR were correlated to the distribution volume ratios (DVR) derived from dynamic data with Logan reference tissue model.

Results: Group comparison with HC revealed white matter and thalamus as most affected regions. Fewest differences were found in grey matter, and normalisation to frontal cortex (FC) yielded the greatest reduction in variability of healthy grey and white matter. Hence, FC corrected for affected voxels was chosen as PRR, leading to time-activity curves of FC which were congruent to HC data (SUV$_{60-90}$ 0.37, U test $P = 0.42$). SUVR showed a very strong correlation with DVR (Pearson $\rho > 0.9$). Focal MS lesions exhibited a high SUVR (range, 1.3–3.2).

Conclusions: This comparison with parameters from dynamic data suggests that SUVR normalised to corrected frontal cortex as PRR is suitable for the quantification of [^{18}F]GE-180 uptake in lesions and different brain regions of RRMS patients. This efficient diagnostic protocol based on static [^{18}F]GE-180 PET scans acquired 60–90 min p.i. allows the semi-quantitative assessment of neuroinflammation in RRMS patients in clinical routine.

Keywords: PET, [^{18}F]GE-180, Multiple sclerosis, TSPO, Quantification

---

* Correspondence: Lena.Vomacka@med.uni-muenchen.de
[1]Department of Nuclear Medicine, University Hospital, LMU Munich, Marchioninistr. 15, 81377 Munich, Germany
Full list of author information is available at the end of the article

Vomacka *et al. EJNMMI Research* (2017) 7:89

Page 2 of 9

Background

The classic diagnosis of multiple sclerosis (MS) is based on clinical and paraclinical documentation of the dissemination of CNS lesions in time and space. Such lesions and their evolution over time are commonly detected by magnetic resonance imaging (MRI). This forms not only the basis of the diagnosis but is also used to monitor disease activity and inform the decision on appropriate therapeutic strategies. While in MRI, the disruption of the blood-brain barrier (BBB) is used as proxy of disease activity, positron emission tomography (PET) imaging of activated microglia or macrophages with the 18-kDa translocator protein (TSPO) visualises one of the hallmarks of neuroinflammation and thus might provide a more direct approach to assess disease activity in MS. TSPO is primarily expressed in activated microglia, astrocytes, endothelial cells, and infiltrating macrophages [1] and is therefore associated with nervous system inflammation [2]. The prototypic TSPO radioligand $[^{11}C](R)$-PK11195 has been frequently investigated in various PET imaging studies [3]. However, quantification with $[^{11}C](R)$-PK11195 has been shown to be challenging due to a low free fraction in plasma, a significant binding to plasma proteins, and a low extraction fraction in brain with a limited signal-to-background ratio [4, 5]. This led to the development of second-generation TSPO radioligands with lower non-specific binding and higher affinity and specificity.

Preclinical data of the third-generation TSPO radioligand $[^{18}F]GE$-180 have demonstrated a higher specific signal in affected brain regions and a lower non-specific binding in healthy tissue than $[^{11}C](R)$-PK11195 in models of stroke [6] and neuroinflammation [7, 8]. Our own preclinical experience with this tracer indicated a very good applicability for monitoring neuroinflammatory disease as well [9]. First-in-human studies with healthy controls (HC) found a low first-pass extraction resulting in low uptake of $[^{18}F]GE$-180 in healthy tissue [10, 11]. Various compartmental models with and without an extravascular component that takes into account tracer binding to endothelial cells were investigated and the authors suggested a two-tissue compartment model without an extravascular component as the preferred method for $[^{18}F]GE$-180 quantification in healthy controls and 90 min as the optimal scan length for reliable estimation of volumes of distribution (V_T) [10, 11]. Distribution volumes from Logan plot and semi-quantitative SUVs (60–90 min p.i.) correlated well with V_T from 2TC model [10, 11]. Although the so far available pre-clinical data are promising, the performance of $[^{18}F]GE$-180 as a tracer for neuroinflammatory diseases in human patients still needs to be verified.

This is the first study investigating relapsing-remitting MS (RRMS) patients with $[^{18}F]GE$-180 PET with the aim of quantifying the uptake in various anatomical brain regions and in focal lesions. In particular, we focused (1) on the identification of a pseudo-reference region (PRR), which is challenging in diseases with widespread inflammation within the brain [12], and (2) on the comparison of parameters obtained from dynamic and static data, the latter one avoiding long scan times and demanding data processing steps, with the goal of providing a quantification procedure which is suitable for routine clinical use.

Methods

Radiochemistry

As described previously [13], $[^{18}F]GE$-180 production was performed on a FASTLab synthesiser with single-use disposable cassettes manufactured by GE Healthcare (The Grove Centre Amersham, UK). Radiochemical purity exceeded 95% and a high-specific activity was reached, ranging between 2423 and 3293 GBq/μmol.

DNA extraction and polymorphism genotyping

Due to the reported dependency of binding properties of the second-generation TSPO ligands on a genetic polymorphism of the TSPO gene, all individuals were genotyped and classified as low-, medium-, or high-affinity binder (LAB, MAB, and HAB) [14–17]. Genotyping for TSPO polymorphism was performed at the Department of Psychiatry of the University Hospital Regensburg on 4 mL whole blood samples. Genomic DNA was extracted with QIAmp DNA blood maxi kit (Qiagen, Hilden, Germany) following the manufacturer's protocol. DNA quality assessment was performed with optical absorbance and gel electrophoresis. Exon 4 of the TSPO gene containing the polymorphism rs6971 (Ala or Thr at position 147) as well as exon/intron junctions were PCR amplified and sequenced using Sanger method with the primers ex4-F-AGTTGGGCAGTGGGACAG and ex4-R-GCAGATCCTGCAGAGACGA. Sequencing data were analysed using SnapGene software (GSL Biotech; available at snapgene.com). The identified rs6971 genotypes (C/C, C/T, or T/T) code for the amino acids Ala/Ala, Ala/Thr, or Thr/Thr at position 147 of the TSPO protein and were considered to generate a high-, medium-, or low-affinity binding phenotype, respectively [17].

Patient data and human subjects

Seventeen dynamic PET scans were performed in 14 RRMS patients (7 female and 7 male; mean age 39 ± 9 years; 5 MAB and 9 HAB). At the time of the PET scan, 4 patients were without treatment, 5 patients were receiving

Vomacka et al. EJNMMI Research (2017) 7:89

Page 3 of 9

rituximab, 3 patients were receiving glatirameracetate, 2 were receiving natalizumab, and 1 patient each was treated with alemtuzumab, interferon-beta, and teriflunomide, respectively. The study with patients was approved by the local ethics committee (IRB no. 601–16) and the German radiation protection committee. All patients gave written informed consent.

To determine the most affected brain regions and for a reproducible definition of reference tissue in MS patients, a database of 6 healthy controls (HC, 3 female and 3 male; mean age 23 ± 6 years; 1 MAB and 5 HAB) was provided by GE Healthcare (The Grove Centre Amersham, UK). The underlying study of healthy subjects was approved by the McMaster University Research Ethics Board. Research was conducted in accordance with the principles of the Declaration of Helsinki and all subjects gave written informed consent.

Imaging
Dynamic HC PET studies (4×30, 3×60, 10×150, 12×300 s) were acquired after injection of 269 ± 7 MBq [18F]GE-180 on a Biograph 6 PET/CT (Siemens Healthineers, Erlangen, Germany) and reconstructed with OSEM2D algorithm (8 iterations, 4 subsets, 4 mm Gauss). Standard corrections for CT-based attenuation, scatter, decay, and random counts were applied.

Seventeen dynamic PET studies of 14 RRMS patients were performed on a Biograph 64 PET/CT device (Siemens Healthineers, Erlangen, Germany). Based on previously published experience with HC, a 90-min emission scan was acquired in list mode, starting with injection of 189 ± 11 MBq [18F]GE-180. Reconstruction with a $256 \times 256 \times 109$ matrix, voxel size of $1.336 \times 1.336 \times 2.027$ mm^3 (framing 12×10, 4×30, 2×60, 2×120, 16×300 s) was performed using the same reconstruction settings as for HC data. PET data were corrected for subject motion within the PMOD Fusion tool (v3.5, PMOD Technologies, Zurich, Switzerland).

For each subject, a T_1-weighted MRI scan with a slice thickness of at least 3 mm was performed on a Magnetom 3T scanner (Siemens Healthineers, Erlangen, Germany) with intravenous injection of 0.1 mmol/kg contrast agent (Gd-BOPTA, MultiHance; Bracco Imaging, Milan, Italy). Contrast-enhanced (CE) MRI images were co-registered to the corresponding PET data.

Anatomical brain regions
For VOI-based analysis, anatomical brain regions were defined with the workflow provided within the PMOD Neuro tool (v3.5). First, each PET image was mapped to the corresponding T_1-weighted CE MRI image by rigid matching using the default settings. Then, each MRI image was normalised to the T_1-weighted MRI template in Montreal Neurological Institute (MNI) space. This was followed by the application of a maximum

probability atlas (Hammers N30R83 [18]) for VOI definition. Grey matter was masked by application of the default threshold of 0.3 on the grey matter probability atlas. Anatomical brain VOIs were then transformed into PET space.

Reference tissue extraction
SUV was determined at 60 to 90 min p.i. (SUV_{60-90}) [11]. For the extraction of brain tissue which is least affected by disease, a voxel-wise comparison of SUV_{60-90} (two sample t test) between HC and all MS patient scans was conducted with statistical parametric mapping (SPM8; Wellcome Trust Centre for Neuroimaging, UK) assuming unequal variance. Smoothing of images was not performed. For this purpose, PET data were mapped into MNI space using the corresponding MRI images with the PMOD Neuro tool as described in the previous section. Anatomically defined brain volumes exhibiting a low fraction of significant voxels in SPM were identified by determination of the fraction of voxels with a t score above 2.52 ($P < 0.01$) for each volume. Within these volumes, the volume best suited for reduction of variability of healthy tissue uptake was selected by calculating the coefficients of variation of grey matter (GM) and white matter (WM) uptake in HC after normalisation to each eligible brain region.

This was followed by an exclusion of voxels suspected of being affected by disease relying on mean SUV_{60-90} and standard deviation (SD) from HC data in this region. The optimal upper threshold $T_{PRR} = \text{mean} + a \times SD$ was iteratively adapted by minimising the difference between the average PRR time-activity curve (TAC) of RRMS patients and the average FC TAC of HC.

Quantification with DVR and SUVR
Specific binding relative to non-displaceable uptake can be derived directly from compartmental model parameters (binding potential $BP_{ND} = k_3/k_4$). Alternatively, it can be calculated from distribution volume ratios ($BP_{ND} = V_T/V_{ND} - 1$) [19]. Since there is no reference tissue available for [18F]GE-180, which is devoid of specific binding, the quantity of interest was specific binding relative to healthy tissue PRR ($BP = V_T/V_{PRR} - 1 = DVR - 1$), which is smaller than $BP_{ND} = DVR(1 + BP_{ND,PRR}) - 1$ [20]. The Logan reference tissue model [21] was used to determine DVR with PMOD Kinetic Modelling tool (v3.4) from dynamic 20–90 min p.i. data [10]. The population average rate $k_2'^{REF}$ of the reference tissue was set to 0.027 1/min according to the previously published average value for frontal cortex k_2 estimated with one-tissue compartment model [11]. For one exemplary patient, a parametric DVR map was generated from dynamic data reconstructed with a 10-mm Gauss filter. Due to high statistical

Vomacka *et al. EJNMMI Research* (2017) 7:89

Page 4 of 9

fluctuations, the coarse filter had to be applied for voxel-wise fitting with Logan reference tissue model.

To assess whether modelling based on dynamic 20–90 min p.i. data can be replaced by values obtained from shorter static scans, a simple quantification based on standardised uptake value ratios (SUVR = SUV_{60-90}/$SUV_{PRR,60-90}$) was carried out by comparison with DVR obtained from Logan reference tissue model. Correlation was determined for all brain tissue regions and lesions.

Segmentation of MS lesions

VOIs of 67 focal MS lesions visible in PET were defined on SUVR images. A delineation method, which aims to find the boundary reproducing threshold T_{SUVR} based on the mean signal from 32 hottest voxels of each lesion ($SUVR_{32Vox}$, total volume of 0.116 mL) and affected white matter background (BG) value, was applied [22]:

$$T_{SUVR} = (SUVR_{32Vox} - SUVR_{BG}) \times F + SUVR_{BG} \quad (1)$$

The fraction $F = 0.35$ was derived from a Nema-NU2-2001 phantom measurement consisting of six hot spheres in BG (1:8) with different volumes (0.5–26.5 mL). The affected WM uptake normalised to PRR averaged over all patients served as BG for the delineation of locally elevated uptake within WM without being influenced by a patient-specific lesion load. Alternatively, background volumes surrounding the focal lesions can be delineated manually for each patient.

Statistical analysis

Results are presented as mean ± SD. Analysis of group-wise differences between different binding affinity groups and VOI parameters of HC and MS patient data was calculated with Mann-Whitney U test (U test) using MATLAB (MathWorks, USA), where $P < 0.05$ was

considered as a significant difference. Linear correlation of quantitative parameters was performed (Pearson, MATLAB, MathWorks, USA).

Results

[^{18}F]GE-180 uptake in MS patients

TAC averaged over all RRMS patient scans are shown in Fig. 1a. [^{18}F]GE-180 uptake in brain tissue peaked at about 35 s p.i. with the lowest mean peak-SUV in white matter (0.88 ± 0.3) and the highest mean peak SUV in the thalamus (1.24 ± 0.4) and brainstem (1.16 ± 0.4). Mean peak SUV in cortical and cerebellar grey matter was similar (1.06 ± 0.4, 1.13 ± 0.4). While cortical and cerebellar GM reached a plateau after about 60 min p.i, the brainstem, WM, and also the thalamus of the MS patients exhibited a slowly increasing TAC after the fast wash-out. SUV_{60-90} was lowest in white matter (0.41 ± 0.05), and highest in brainstem (0.49 ± 0.06) and thalamus (0.48 ± 0.05). SUV_{60-90} in cortical GM was 0.43 ± 0.05 and in cerebellar GM 0.44 ± 0.06. In contrast to the uptake kinetics of apparently not affected tissue, MS lesions exhibited a constant increase or saturation of uptake (Fig. 1b) with a mean SUV_{60-90} of 0.7 ± 0.2.

No significant differences (U test $P > 0.05$) in SUV_{60-90} were found between MAB and HAB in all anatomical brain regions (e.g. combined frontal, temporal, and parietal cortex SUV: MAB = 0.41 ± 0.04, HAB = 0.41 ± 0.05).

Reference tissue extraction

Results from SPM group analysis on static 60 to 90 min p.i. images are given in Fig. 2. The t score images are given for a cut-off threshold of $P < 0.01$. White matter (average t score 2.7 and $P = 0.03$) and the thalamus (average t score 2.6 and $P = 0.06$) exhibited the highest fraction of voxels with $P < 0.01$ (> 55%). The fraction with $P < 0.01$ was below 25% in the frontal lobe,


Fig. 1 [^{18}F]GE-180 time-activity curves in SUV averaged over all MS patient studies. **a** Mean TAC of brainstem (circle), cortical GM (square), thalamus (cross), cerebellar GM (diamond), and white matter (triangle). **b** Mean ± SD TAC averaged over 67 lesions

Vomacka *et al. EJNMMI Research* (2017) 7:89

Page 5 of 9
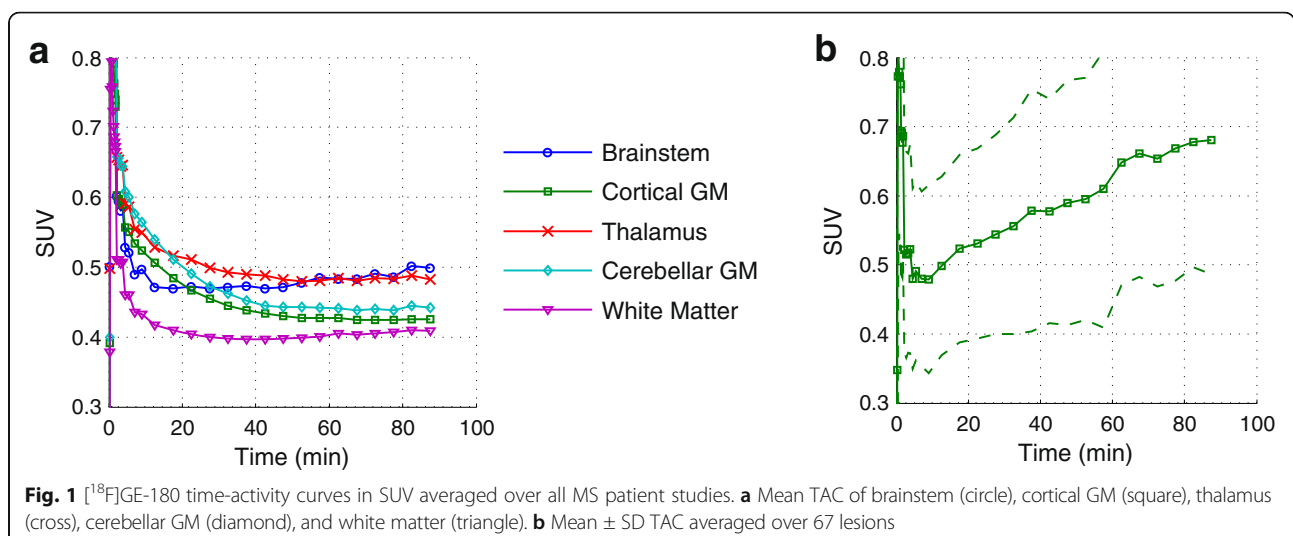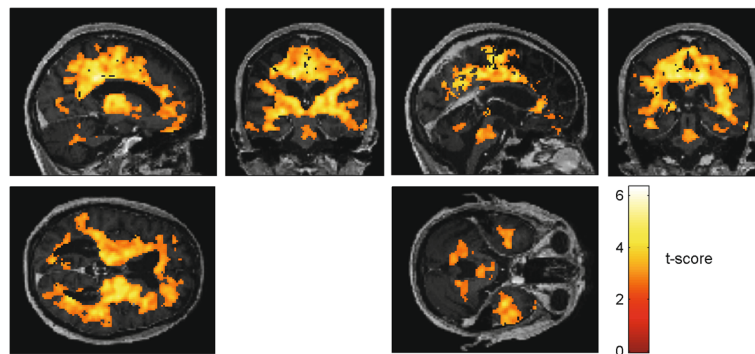
Fig. 2 Statistical parametric maps from two sample *t* test with an extent threshold of 60 voxels with *t* score values showing differences in [^{18}F]GE-180 uptake in static 60 to 90 min p.i. images between healthy controls and all MS patient scans with a cut-off threshold of *P* < 0.01 in triangular views

temporal lobe, and in cerebellar grey matter (average *t* score < 1.8 and *P* > 0.10). Normalisation to frontal cortex (FC) led to the lowest variability of grey and white matter uptake (GM decreased from 12 to 6%, WM remained at 7%) in HC. Therefore, FC was chosen as the anatomically defined primary reference tissue.

Mean frontal cortex SUV_{60-90} in HC was 0.37 ± 0.04. The optimal upper threshold for unaffected FC voxels obtained by iterative adoption was:

$$T_{PRR} = mean_{HC} + 1.7 \times SD_{HC} \qquad (2)$$

This corresponds to a SUV_{60-90} threshold of 0.433. The resulting corrected FC volume applied in the following as pseudo-reference region yielded a SUV_{60-90} of 0.37 ± 0.03 averaged over all MS patient studies. No significant difference was found between the corrected frontal cortex SUV_{60-90} in MS patients and the corresponding values in HC (Fig. 3, *U* test *P* = 0.42). Based on this pseudo-reference region, SUVR images were generated as visualised in Fig. 4. Variability in uptake values in patients reduced with PRR normalisation for GM from 11 to 7%, and for WM from 13 to 10%.
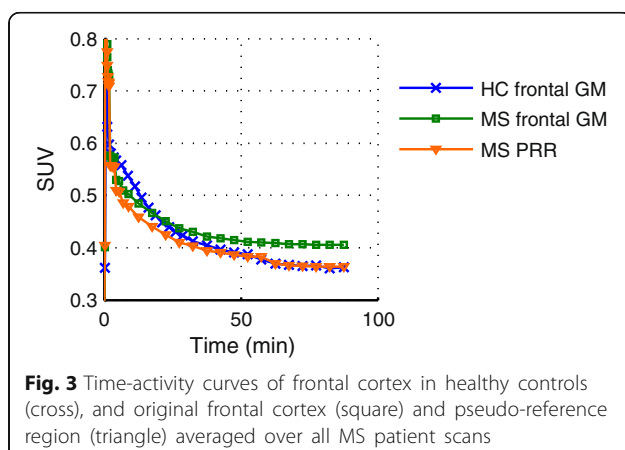
Fig. 3 Time-activity curves of frontal cortex in healthy controls (cross), and original frontal cortex (square) and pseudo-reference region (triangle) averaged over all MS patient scans

Quantification with DVR and SUVR

The linear part of the Logan plot started earlier for brain tissue data than for lesion data and both reached linearity (Fig. 5). DVR derived from Logan reference tissue model showed a very strong correlation with SUVR (Fig. 6: anatomical brain regions ρ = 0.97, *P* < 0.001, and lesions ρ = 0.93, *P* < 0.001). In RRMS patients, thalamus and brainstem exhibited the highest values (SUVR 1.33 ± 0.11 and 1.35 ± 0.17, DVR 1.35 ± 0.14 and 1.45 ± 0.24) and WM and cortical GM the lowest (SUVR 1.11 ± 0.11 and 1.16 ± 0.09, DVR 1.19 ± 0.13 and 1.18 ± 0.10).

For observer-independent assessment of inflammation activity in focal lesions, a SUVR of 1.3 was assumed as affected WM background. This value was derived from SUVR images normalised to PRR by adoption of Eq. (2): $T_{Lesion,BG} = mean_{HC,WM} + 1.7 \times SD_{HC}$, where $T_{Lesion,BG}$ served as lower threshold for the definition of affected white matter voxels in MS patients. For all RRMS patients studied, the average SUVR of lesions delineated by this method was between 1.3 and 3.2 (mean 1.9 ± 0.5). Maximum SUVR within lesions ranged between 1.5 and 4.9 (2.4 ± 0.9). All MS lesions exhibited an increasing or saturating TAC (Fig. 1b).

Discussion

This study aimed to provide a robust, clinically suitable quantification approach for the third-generation TSPO ligand [^{18}F]GE-180 in MS patients. The investigated static 60–90 min imaging containing a PRR-based SUVR quantification correlated well with DVR from modelling by application of the Logan reference tissue model on dynamic 90 min and thus proved suitability for clinical TSPO PET application, when patient compliance and economic aspects have to be considered. The presence of non-saturated lesion TACs suggests that a prolongation of the scan duration, at the cost of a lower count statistic, might allow for an improved assessment of equilibrium and tracer wash-out.
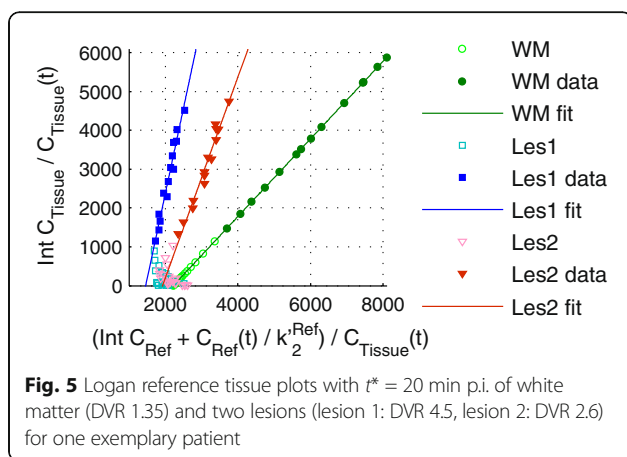
Vomacka et al. EJNMMI Research (2017) 7:89

Page 6 of 9
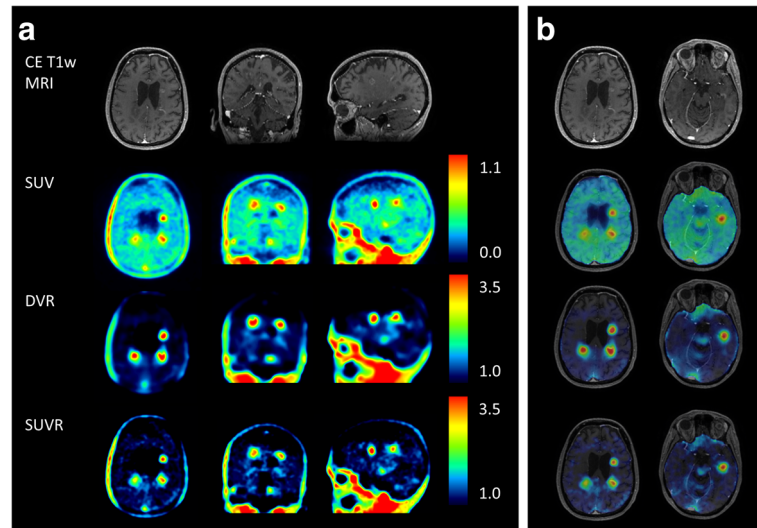
Fig. 4 Images of an MS patient in native [^{18}F]GE-180 PET space. Top row: T_1-weighted contrast-enhanced MRI. Second row: SUV image (60–90 min p.i.). Third and bottom row: DVR (from dynamic data reconstructed with 10-mm Gauss filter) and SUVR with lower threshold set to 1.0 for the depiction of specific binding relative to the PRR. **a** Whole head in triangular views. **b** Application of brain mask onto parametric maps for two different transaxial planes with MRI overlay

Binding potentials derived with reference modelling (BP = DVR – 1) reported previously for the prototypic TSPO ligand [^{11}C](R)-PK11195 in healthy controls, and MS patients were in a similar range as results presented here for [^{18}F]GE-180: the lowest BP was found in normal-appearing white matter and the highest BP in the thalamus and the brainstem [23–25]. In agreement with our SPM analysis results, PET signal was significantly elevated compared to HC in contrast-enhancing lesions, thalamus, parts of the brainstem, and in white matter frequently following white matter fibre tracts [23, 25–27].

MS lesions exhibited a high [^{18}F]GE-180 uptake and contrast, enabling a visual detection of focally elevated tracer accumulations (Fig. 4). The lesion-to-WM-background ratio (up to a threefold increase in mean lesion

Fig. 5 Logan reference tissue plots with $t^* = 20$ min p.i. of white matter (DVR 1.35) and two lesions (lesion 1: DVR 4.5, lesion 2: DVR 2.6) for one exemplary patient

SUVR) appears to be high for [^{18}F]GE-180 compared to other TSPO radioligands previously used in MS patients [23–30]. [^{11}C]PK11195 signal in static images normalised to cortical grey matter was significantly higher in lesions with CE in MRI compared to normal white matter (up to a factor of 1.4) [26]. For [^{18}F]FEDAA1106, lesions with CE in MRI were not detectable in SUV and Logan V_T images, probably due to a high non-specific uptake [30]. Both [^{18}F]PBR111 and [^{11}C]PBR28 showed an increased V_T in some lesions with CE in MRI [24, 28, 29]. However, for [^{11}C]PBR28, static SUV$_{90–120}$ images were too noisy for visual detection of MS lesions, most probably due to the short half-life of ^{11}C in combination with a high-resolution PET tomograph [29].

The critical aspect for robust and reliable lesion quantification is the choice of the reference region. It is difficult to propose a standard reference region for all neurological diseases since patterns of affection vary widely. In MS, immune cell infiltration is predominantly localised in focal white matter lesions. However, as the disease progresses, inflammatory changes spread throughout the CNS and no region can be assumed to be unaffected. The corrected frontal cortex seems to be a suitable pseudo-reference region, at least for RRMS patients, since grey matter was reported to be less affected than white matter in early stages of MS [24–26, 28]. In order to identify the least affected regions in RRMS patients, we compared our patients with a group of young HC, in which no CNS inflammation should be present. Although the SPM analysis revealed a non-negligible fraction (24%) affected by disease in the frontal cortex, time activity curves were not significantly different for HC and RRMS patients in this

Vomacka *et al. EJNMMI Research* (2017) 7:89

Page 7 of 9

Fig. 6 Pearson correlation of SUVR obtained from static 60–90 min p.i. images with DVR from Logan reference tissue model applied to dynamic 20–90 min p.i. PET data. **a** Anatomical brain regions: $\rho = 0.97$, $P < 0.001$, $y = 0.79x + 0.22$. **b** Lesions: $\rho = 0.93$, $P < 0.001$, $y = 0.35x + 1.12$
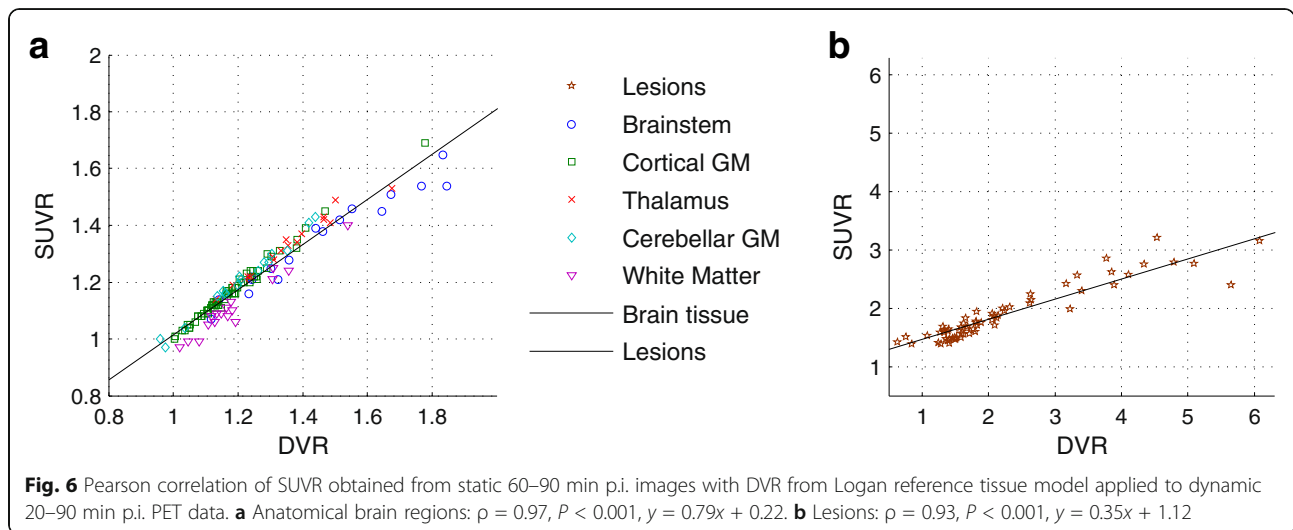
region, and it was feasible to exclude suspicious voxels in this relatively large and well-defined region. The VOI-based comparison of PRR SUVs with HC data showed good concordance. Normalisation of PET data by the corrected frontal cortex uptake reduced inter-patient variability in grey (from 11 to 7%) and white matter (from 13 to 10%) signals.

Alternative methods recommended for reference tissue TAC generation of TSPO tracers are data-driven clustering (DC) [31, 32] or supervised clustering (SC) on dynamic data preselected with a brain mask [33, 34]. SC has been validated for $[^{11}C](R)$-PK11195 and also tested for $[^{18}F]$GE-180 [8]. However, DC and SC require dynamic PET studies and previous publications show that SC might not sufficiently exclude affected voxels in some cases and that other methods might be superior for the exclusion of affected voxels [8, 35]. A promising approach using fixed thresholds for the definition of affected voxels was applied to BP images derived with SC reference tissue [23] but also needs dynamic imaging.

The reported high inter- and intra-subject variability found for second-generation radioligands in other studies was attributed to differences in binding affinity status and in plasma protein binding [5, 36, 37]. For $[^{11}C](R)$-PK11195, in vitro and in vivo data show no significant differences between binding affinity groups. Unpublished in vitro work by D. Owen with cold GE-180 displacing $[^3H]$PK11195 has shown a binding affinity ratio of 15:1 between HABs and MABs [11]. However, Feeney et al. [11] found no significant differences between MABs and HABs similar to $[^{11}C](R)$-PK11195 in healthy brain tissue of human subjects [16]. This is in line with the results of our current study in which we found no differences between MAB and HAB. Although in vitro prediction of differences in specific binding can differ from the relation observed for in vivo data [15, 38], it is

questionable whether this can explain the results. Such a discrepancy may be explained by the high dependency of the in vitro studies on experimental conditions like temperature, fluid composition, and presence of intact mitochondria [15]. Furthermore, brain microvascular endothelial cells change BBB properties in vitro [39]. Fan et al. [10] suggest that the finding that no differences could be observed in vivo may be caused by a lower TSPO affinity of $[^{18}F]$GE-180 compared to other second-generation TSPO tracers. Another explanation proposed by both previous studies is the low brain tissue uptake [10, 11]. The high fraction of ligand bound to plasma proteins, probably resulting from a relatively high lipophilicity (logD at pH 7.4 is 2.95 [40]), may be the reason for the slow propagation into tissue and the constantly high activity concentration in blood vessels dominating signal in healthy tissue (suggesting similarities to $[^{11}C](R)$-PK11195 in vivo) [41, 42]. Another reason for low uptake in brain may be a fast clearance by efflux pumps.

Yet, we observe a high contrast in MS lesions and also in gliomas as published recently [43]. The important question is what are the underlying processes leading to this contrast. Does it reflect specific binding to TSPO or rather other processes like a BBB breakdown? For gliomas, we could demonstrate that $[^{18}F]$GE-180 uptake patterns do not correlate with contrast enhancement in T_1-weighted MRI images and that even for some gliomas, the highest $[^{18}F]$GE-180 uptake can be found in non-contrast-enhancing tumour areas [43]. Still one might hypothesise that those areas exhibit micro BBB breakdown without apparent enhancement of contrast agent in MRI [44], which may allow the passage of $[^{18}F]$GE-180 through the leaky BBB. However, we also observe areas with CE in T_1-weighted MRI, i.e. with BBB breakdown, but without elevated $[^{18}F]$GE-180

Vomacka *et al. EJNMMI Research* (2017) 7:89

Page 8 of 9

uptake [43]. Even if micro BBB breakdown might ease the supply of [^{18}F]GE-180, the [^{18}F]GE-180 signal intensity does not correlate with severity of BBB breakdown, leading to the assumption that the dominant process resulting in the observed high range of [^{18}F]GE-180 binding should be attributed to TSPO expression levels rather than mere BBB breakdown. Nevertheless, the lack of micro BBB breakdown in some regions may lead to an underestimation of TSPO expression.

One limitation of this study may be the usage of data from two different PET/CT devices in which the PET part is identical, but the CT data may yield a slightly different attenuation correction. Also, for future clinical studies, it would be beneficial to gather a larger database of HC with varying age to account for age-related changes. Furthermore, for an encompassing and comprehensive interpretation of the underlying processes, it is indispensable to perform in vivo blocking studies in combination with pharmacokinetic modelling with a metabolite corrected arterial input function and a longer scan duration.

The possibility of static PET imaging provided by the proposed method in contrast to dynamic PET imaging will greatly increase the acceptance by patients, as 30-min scans are usually well-tolerated and the imaging protocol does not include blood sampling, which is often perceived as an invasive, displeasing method by patients and is therefore often avoided in clinical settings. With these tools, TSPO PET with [^{18}F]GE-180 may enable straightforward clinical assessment of neuroinflammatory activity in MS beyond the scope of structural MRI and seems to be a highly promising imaging method to assess disease activity and therapy response in RRMS patients.

Conclusions

In patients suffering from RRMS, the new TSPO ligand [^{18}F]GE-180 presented a highly elevated signal up to a threefold increase in SUVR of focal lesions compared to surrounding background. Our data demonstrate a high correlation between parameters obtained from dynamic PET imaging with simple SUV ratios extracted from static 60–90 min [^{18}F]GE-180 PET scans using the corrected frontal cortex as pseudo-reference region.

Abbreviations

BBB: Blood-brain barrier; BP: Binding potential; CE: Contrast-enhanced; DC: Data-driven clustering; DVR: Distribution volume ratio; FC: Frontal cortex; GM: Grey matter; HAB: High-affinity binder; HC: Healthy controls; MAB: Medium-affinity binder; MNI: Montreal Neurological Institute; MRI: Magnetic resonance imaging; MS: Multiple sclerosis; PET: Positron emission tomography; PRR: Pseudo-reference region; RRMS: Relapsing remitting multiple sclerosis; SC: Supervised clustering; SD: Standard deviation; SUV: Standardised uptake value; SUVR: Standardised uptake value ratio; TAC: Time-activity curve; TSPO: Translocator protein; V_{T}: Volume of distribution; WM: White matter

Authors' contributions
LV, NA, MB, SZ, MK, PB, and GB contributed to the concept and design of the study. CM and TK recruited RRMS patients. RR carried out polymorphism genotyping. CB provided dynamic PET data and MRI images of healthy controls. LV, MU, LE, AG, and AB helped with data collection and analysis. SL was responsible for radiopharmaceutical production. LV performed data analysis. All authors contributed to the drafting of the manuscript, and all authors read and approved the final manuscript.

Ethics approval and consent to participate
The study with patients was approved by the local ethics committee (IRB no. 601–16) and the German radiation protection committee. The study of healthy subjects was approved by the McMaster University Research Ethics Board. All individual participants gave written informed consent.

Consent for publication
Not applicable.

Competing interests
The authors declare that they have no competing interests.

Publisher's Note
Springer Nature remains neutral with regard to jurisdictional claims in published maps and institutional affiliations.

Author details
[1]Department of Nuclear Medicine, University Hospital, LMU Munich, Marchioninistr. 15, 81377 Munich, Germany. [2]Institute of Clinical Neuroimmunology, University Hospital, LMU Munich, Munich, Germany. [3]GE Healthcare, Grove Centre, Amersham, UK. [4]Department of Psychiatry and Psychotherapy, University of Regensburg, Regensburg, Germany. [5]Munich Cluster for Systems Neurology (SyNergy), Munich, Germany.

References
1. Papadopoulos V, Baraldi M, Guilarte TR, Knudsen TB, Lacapère J-J, Lindemann P, et al. Translocator protein (18kDa): new nomenclature for the peripheral-type benzodiazepine receptor based on its structure and molecular function. Trends Pharmacol Sci. 2006;27:402–9.
2. Rupprecht R, Papadopoulos V, Rammes G, Baghai TC, Fan J, Akula N, et al. Translocator protein (18 kDa)(TSPO) as a therapeutic target for neurological and psychiatric disorders. Nat Rev Drug Discov. 2010;9:971–88.
3. Schweitzer PJ, Fallon BA, Mann JJ, Kumar JS. PET tracers for the peripheral benzodiazepine receptor and uses thereof. Drug Discov Today. 2010;15:933–42.
4. Lockhart A, Davis B, Matthews JC, Rahmoune H, Hong G, Gee A, et al. The peripheral benzodiazepine receptor ligand PK11195 binds with high affinity to the acute phase reactant α1-acid glycoprotein: implications for the use of the ligand as a CNS inflammatory marker. Nucl Med Biol. 2003;30:199–206.
5. Turkheimer FE, Rizzo G, Bloomfield PS, Howes O, Zanotti-Fregonara P, Bertoldo A, et al. The methodology of TSPO imaging with positron emission tomography. Biochem Soc Trans. 2015;43:586–92.
6. Boutin H, Murray K, Pradillo J, Maroy R, Smigova A, Gerhard A, et al. 18F-GE-180: a novel TSPO radiotracer compared to 11C-R-PK11195 in a preclinical model of stroke. Eur J Nucl Med Mol Imaging. 2015;42:503–11.
7. Dickens AM, Vainio S, Marjamäki P, Johansson J, Lehtiniemi P, Rokka J, et al. Detection of microglial activation in an acute model of neuroinflammation using PET and radiotracers 11C-(R)-PK11195 and 18F-GE-180. J Nucl Med. 2014;55:466–72.
8. Sridharan S, Lepelletier FX, Trigg W, Banister S, Reekie T, Kassiou M, et al. Comparative evaluation of three TSPO PET radiotracers in a LPS-induced model of mild Neuroinflammation in rats. Mol Imaging Biol. 2017;19:77–89.

Vomacka *et al. EJNMMI Research* (2017) 7:89

Page 9 of 9

9. Brendel M, Probst F, Jaworska A, Overhoff F, Korzhova V, Albert NL, et al. Glial activation and glucose metabolism in a transgenic amyloid mouse model: a triple-tracer PET study. J Nucl Med. 2016;57:954–60.
10. Fan Z, Calsolaro V, Atkinson RÁ, Femminella GD, Waldman A, Buckley C, et al. Flutriciclamide (18F-GE180) PET: first in human PET study of novel 3rd generation in vivo marker of human translator protein. J Nucl Med. 2016;57:1753–9.
11. Feeney C, Scott G, Raffel J, Roberts S, Coello C, Jolly A, et al. Kinetic analysis of the translocator protein positron emission tomography ligand [18F]GE-180 in the human brain. Eur J Nucl Med Mol Imaging. 2016;43:2201–10.
12. Hinz R, Boellaard R. Challenges of quantification of TSPO in the human brain. Clin Transl Imaging. 2015;3:403–16.
13. Wickstrøm T, Clarke A, Gausemel I, Horn E, Jørgensen K, Khan I, et al. The development of an automated and GMP compliant FASTlab™ synthesis of [18F] GE-180; a radiotracer for imaging translocator protein (TSPO). J Labelled Comp Radiopharm. 2014;57:42–8.
14. Guo Q, Owen DR, Rabiner EA, Turkheimer FE, Gunn RN. Identifying improved TSPO PET imaging probes through biomathematics: the impact of multiple TSPO binding sites in vivo. NeuroImage. 2012;60:902–10.
15. Kreisl WC, Fujita M, Fujimura Y, Kimura N, Jenko KJ, Kannan P, et al. Comparison of [11 C]-(R)-PK 11195 and [11 C] PBR28, two radioligands for translocator protein (18 kDa) in human and monkey: implications for positron emission tomographic imaging of this inflammation biomarker. NeuroImage. 2010;49:2924–32.
16. Owen DR, Gunn RN, Rabiner EA, Bennacef I, Fujita M, Kreisl WC, et al. Mixed-affinity binding in humans with 18-kDa translocator protein ligands. J Nucl Med. 2011;52:24–32.
17. Owen DR, Yeo AJ, Gunn RN, Song K, Wadsworth G, Lewis A, et al. An 18-kDa translocator protein (TSPO) polymorphism explains differences in binding affinity of the PET radioligand PBR28. J Cereb Blood Flow Metab. 2012;32:1–5.
18. Hammers A, Allom R, Koepp MJ, Free SL, Myers R, Lemieux L, et al. Three-dimensional maximum probability atlas of the human brain, with particular reference to the temporal lobe. Hum Brain Mapp. 2003;19:224–47.
19. Logan J, Fowler JS, Volkow ND, Wang GJ, Ding YS, Alexoff DL. Distribution volume ratios without blood sampling from graphical analysis of PET data. J Cereb Blood Flow Metab. 1996;16:834–40.
20. Gunn RN, Lammertsma AA, Hume SP, Cunningham VJ. Parametric imaging of ligand-receptor binding in PET using a simplified reference region model. NeuroImage. 1997;6:279–87.
21. Logan J. A review of graphical methods for tracer studies and strategies to reduce bias. Nucl Med Biol. 2003;30:833–44.
22. Drever L, Robinson DM, McEwan A, Roa W. A local contrast based approach to threshold segmentation for PET target volume delineation. Med Phys. 2006;33:1583–94.
23. Banati RB, Newcombe J, Gunn RN, Cagnin A, Turkheimer F, Heppner F, et al. The peripheral benzodiazepine binding site in the brain in multiple sclerosis: quantitative in vivo imaging of microglia as a measure of disease activity. Brain. 2000;123(Pt 11):2321–37.
24. Colasanti A, Guo Q, Muhlert N, Giannetti P, Onega M, Newbould RD, et al. In vivo assessment of brain white matter inflammation in multiple sclerosis with 18F-PBR111 PET. J Nucl Med. 2014;55:1112–8.
25. Rissanen E, Tuisku J, Rokka J, Paavilainen T, Parkkola R, Rinne JO, et al. In vivo detection of diffuse inflammation in secondary progressive multiple sclerosis using PET imaging and the radioligand 11C-PK11195. J Nucl Med. 2014;55:939–44.
26. Debruyne J, Versijpt J, Van Laere K, De Vos F, Keppens J, Strijckmans K, et al. PET visualization of microglia in multiple sclerosis patients using [11C] PK11195. Eur J Neurol. 2003;10:257–64.
27. Vowinckel E, Reutens D, Becher B, Verge G, Evans A, Owens T, et al. PK11195 binding to the peripheral benzodiazepine receptor as a marker of microglia activation in multiple sclerosis and experimental autoimmune encephalomyelitis. J Neurosci Res. 1997;50:345–53.
28. Oh U, Fujita M, Ikonomidou VN, Evangelou IE, Matsuura E, Harberts E, et al. Translocator protein PET imaging for glial activation in multiple sclerosis. J Neuroimmune Pharmacol. 2011;6:354–61.
29. Park E, Gallezot JD, Delgadillo A, Liu S, Planeta B, Lin SF, et al. 11C-PBR28 imaging in multiple sclerosis patients and healthy controls: test-retest reproducibility and focal visualization of active white matter areas. Eur J Nucl Med Mol Imaging. 2015;42:1081–92.
30. Takano A, Piehl F, Hillert J, Varrone A, Nag S, Gulyas B, et al. In vivo TSPO imaging in patients with multiple sclerosis: a brain PET study with [18F]FEDAA1106. EJNMMI Res. 2013;3:30.

31. Ashburner J, Haslam J, Taylor C, Cunningham V, Jones T. A cluster analysis approach for the characterisation of dynamic PET data. Quantification of brain function using PET: Academic Press; 1996. p. 301-306. https://doi.org/10.1016/B978-012389760-2/50061-X.
32. Gunn RN, Lammertsma AA, Cunningham VJ. Parametric imaging of ligand-receptor interactions using a reference tissue model and cluster analysis. Quantitative functional brain imaging with positron emission tomography: Academic Press; 1998. p. 401-406. https://doi.org/10.1016/B978-012161340-2/50062-7.
33. Turkheimer FE, Edison P, Pavese N, Roncaroli F, Anderson AN, Hammers A, et al. Reference and target region modeling of [11C]-(R)-PK11195 brain studies. J Nucl Med. 2007;48:158–67.
34. Yaqub M, Van B, Bart NM, Schuitemaker A, Hinz R, Turkheimer FE, et al. Optimization of supervised cluster analysis for extracting reference tissue input curves in (R)-[11C] PK11195 brain PET studies. J Cereb Blood Flow Metab. 2012;32:1600–8.
35. Su Z, Herholz K, Gerhard A, Roncaroli F, Du Plessis D, Jackson A, et al. [11C]-(R)PK11195 tracer kinetics in the brain of glioma patients and a comparison of two referencing approaches. Eur J Nucl Med Mol Imaging. 2013;40:1406–19.
36. Kanegawa N, Collste K, Forsberg A, Schain M, Arakawa R, Jucaite A, et al. In vivo evidence of a functional association between immune cells in blood and brain in healthy human subjects. Brain Behav Immun. 2016;54:149–57.
37. Rizzo G, Veronese M, Tonietto M, Zanotti-Fregonara P, Turkheimer FE, Bertoldo A. Kinetic modeling without accounting for the vascular component impairs the quantification of [11C] PBR28 brain PET data. J Cereb Blood Flow Metab. 2014;34:1060–9.
38. Ikawa M, Lohith TG, Shrestha S, Telu S, Zoghbi SS, Castellano S, et al. 11C-ER176, a radioligand for 18-kDa translocator protein, has adequate sensitivity to robustly image all three affinity genotypes in human brain. J Nucl Med. 2017;58:320–5.
39. Urich E, Lazic SE, Molnos J, Wells I, Freskgård PO. Transcriptional profiling of human brain endothelial cells reveals key properties crucial for predictive in vitro blood-brain barrier models. PLoS One. 2012;7:e38149.
40. Wadsworth H, Jones PA, Chau WF, Durrant C, Fouladi N, Passmore J, et al. [18 F] GE-180: a novel fluorine-18 labelled PET tracer for imaging translocator protein 18kDa (TSPO). Bioorg Med Chem Lett. 2012;22:1308–13.
41. Laruelle M, Slifstein M, Huang Y. Relationships between radiotracer properties and image quality in molecular imaging of the brain with positron emission tomography. Mol Imaging Biol. 2003;5(6):363–75. https://doi.org/10.1016/j.mibio.2003.09.009.
42. Pike VW. PET radiotracers: crossing the blood–brain barrier and surviving metabolism. Trends Pharmacol Sci. 2009;30:431–40.
43. Albert NL, Unterrainer M, Fleischmann D, Lindner S, Vettermann F, Brunegraf A, et al. TSPO PET for glioma imaging using the novel ligand 18F-GE-180: first results in patients with glioblastoma. Eur J Nucl Med Mol Imaging. 2017:1–9.
44. Israeli D, Tanne D, Daniels D, Last D, Shneor R, Guez D, et al. The application of MRI for depiction of subtle blood brain barrier disruption in stroke. Int J Biol Sci. 2011;7:1.

Chapter 5

Publication II

ORIGINAL RESEARCH

Open Access

Voxel-wise analysis of dynamic ^{18}F-FET PET: a novel approach for non-invasive glioma characterisation

Lena Vomacka[1], Marcus Unterrainer[1,2], Adrien Holzgreve[1,3], Erik Mille[1], Astrid Gosewisch[1], Julia Brosch[1], Sibylle Ziegler[1], Bogdana Suchorska[3], Friedrich-Wilhelm Kreth[3], Jörg-Christian Tonn[2,3], Peter Bartenstein[1,2], Nathalie Lisa Albert[1,2] and Guido Böning[1*]

Abstract

Background: Glioma grading with dynamic ^{18}F-FET PET (0–40 min p.i.) is typically performed by analysing the mean time-activity curve of the entire tumour or a suspicious area within a heterogeneous tumour. This work aimed to ensure a reader-independent glioma characterisation and identification of aggressive sub-volumes by performing a voxel-based analysis with diagnostically relevant kinetic and static ^{18}F-FET PET parameters. One hundred sixty-two patients with a newly diagnosed glioma classified according to histologic and molecular genetic properties were evaluated. The biological tumour volume (BTV) was segmented in static 20–40 min p.i. ^{18}F-FET PET images using the established threshold of $1.6 \times$ background activity. For each enclosed voxel, the time-to-peak (TTP), the late slope (Slope$_{15–40}$), and the tumour-to-background ratios (TBR$_{5–15}$, TBR$_{20–40}$) obtained from 5 to 15 min p.i. and 20 to 40 min p.i. images were determined. The percentage portion of these values within the BTV was evaluated with percentage volume fractions (PVFs) and cumulated percentage volume histograms (PVHs). The ability to differentiate histologic and molecular genetic classes was assessed and compared to volume-of-interest (VOI)-based parameters.

Results: Aggressive WHO grades III and IV and *IDH*-wildtype gliomas were dominated by a high proportion of voxels with an early peak, negative slope, and high TBR, whereby the PVHs with TTP < 20 min p.i., Slope$_{15–40}$ < 0 SUV/h, and TBR$_{5–15}$ and TBR$_{20–40}$ > 2 yielded the most significant differences between glioma grades. We found significant differences of the parameters between WHO grades and *IDH* mutation status, where the effect size was predominantly higher for voxel-based PVHs compared to the corresponding VOI-based parameters. A low overlap of BTV sub-volumes defined by TTP < 20 min p.i. and negative Slope$_{15–40}$ with TBR$_{5–15 > 2}$- and TBR$_{20–40 > 2}$-defined hotspots was observed.

Conclusions: The presented approach applying voxel-wise analysis of dynamic ^{18}F-FET PET enables an enhanced characterisation of gliomas and might potentially provide a fast identification of aggressive sub-volumes within the BTV. Parametric 3D ^{18}F-FET PET information as investigated in this study has the potential to guide individual therapy instrumentation and may be included in future biopsy studies.

Keywords: FET PET, Glioma, Histogram analysis, *IDH* mutation

---

* Correspondence: Guido.Boening@med.uni-muenchen.de
[1]Department of Nuclear Medicine, University Hospital, LMU Munich,
Marchioninistr. 15, 81377 Munich, Germany
Full list of author information is available at the end of the article

Vomacka *et al. EJNMMI Research* (2018) 8:91

Page 2 of 13

Background

Structural imaging with T_1-weighted magnetic resonance imaging (MRI) [1], which is the gold standard in clinical glioma assessment, is restricted to the interpretation of properties like tumour contour, localisation, and enhancement pattern [1]. Besides, several functional MRI techniques have shown relevance for prediction of malignant transformation, involving, e.g. perfusion-weighted imaging (PWI) yielding information on relative cerebral blood volume and flow (rCBV, rCBF) [2–4]. In contrast, positron emission tomography (PET) with amino acids aims to directly image an elevated amino acid metabolism of rapidly proliferating tumour cells [5–7]. According to the report on response assessment in neuro-oncology (RANO), dynamic O-(2-^{18}F-fluoroethyl)-L-tyrosine (^{18}F-FET) PET has shown its usefulness in diagnosis, in prognosis of tumour progression, and in assessment of treatment response [8].

The current standard procedure for retrieving information from dynamic ^{18}F-FET PET consists of evaluating parameters such as the tumour-to-background ratio (TBR) at a certain time point, the late slope, the time-activity curve (TAC) pattern, and the time-to-peak (TTP) [9–16]. In particular, the TTP and the TAC pattern have proven to be suitable for identification of tumour recurrence or progression [12, 13, 17], and for glioma grading [14, 15, 18]. Pharmacokinetic modelling of ^{18}F-FET uptake has also been considered. However, to our knowledge, its clinical relevance could not be shown yet, and the requirement of (metabolite-corrected) plasma-input data impairs the clinical applicability [19, 20]. While a slowly increasing TAC is characteristic of low-grade gliomas, the TAC of high-grade gliomas tends to exhibit a short TTP and decreasing TAC [17, 21]. Those parameters are most frequently derived from a mean volume-of-interest (VOI)-TAC of the entire tumour or from the hot-spot of the tumour with a 90% isocontour [17, 22]. However, in case of heterogeneous tumours, it may occur that the hot-spot in summation images does not correspond to the tumour fraction defined as most suspicious regarding tumour aggressiveness according to TTP and TAC pattern. This may potentially lead to an underestimation of malignancy and might impair treatment planning. Recent approaches in current research aiming to improve the assessment of tumour characteristics include, e.g. a slice-by-slice TAC analysis or the extraction of texture parameters from static ^{18}F-FET PET images [23, 24].

The goal of this study was to investigate the intra-tumoural distribution of the abovementioned diagnostically relevant kinetic and static parameters derived from dynamic ^{18}F-FET PET data on a voxel basis. A comparison with VOI-based methods, as currently utilised for non-invasive glioma characterisation in clinical routine, is provided.

Methods

Patients

For this retrospective study we included 162 ^{18}F-FET PET positive patients with a newly diagnosed, untreated glioma who had undergone a dynamic 40 min ^{18}F-FET PET scan prior to diagnosis according to either biopsy or resection. Both stereotactic biopsy and tumour resection were performed using navigation software (Brainlab iPlan version 3.0, Brainlab, Feldkirchen, Germany). The choice of surgical procedure was based on tumour location, patient age, and performance status as well as patient preference; all treatment decisions have been approved by an interdisciplinary tumour board. Neuropathological diagnosis and grading have been performed by at least two neuropathologists as part of the clinical routine as described previously [18, 25]. Besides histology, mutation of *IDH*1/2 gene and, in case of *IDH*1 mutation, co-deletion of chromosomal material on 1p/19q were analysed in accordance with the recently revised version of the WHO grading system for central nervous tumours [26]. The study was approved by the local ethical review board and all patients gave written informed consent (IRB 606-16).

Imaging

Dynamic ^{18}F-FET PET scans were acquired on an ECAT EXACT HR+ scanner (Siemens Healthineers, Erlangen, Germany) after intravenous bolus injection of 176 ± 13 MBq ^{18}F-FET, according to the protocol described in [9, 11]. For patient comfort and minimization of motion during the scan, patients were carefully positioned and fixed. Dynamic 40-min emission data were recorded in 3D mode with 16 frames (7×10 s, 3×30 s, 1×2 min, 3×5 min, and 2×10 min). Standard corrections for random and scattered coincidences, dead time, decay, and attenuation were performed. Attenuation correction was based on transmission scans measured with three rotating ^{68}Ge line sources. Data were reconstructed with filtered back-projection and a 4.9-mm Hann filter. Matrix size was $128 \times 128 \times 63$, and voxel size $2.03 \times 2.03 \times 2.43$ mm^3. All dynamic PET scans were checked frame-by-frame for head movement. Motion correction was performed on affected time frames within PMOD Fusion tool (v3.5, PMOD Technologies, Zurich, Switzerland).

Delineation of tumour volume

Biological tumour volume (BTV) was defined by a TBR$_{20–40}$ above 1.6 in static 20–40 min p.i. summation images [15, 27]. Background (BG) values were derived from a crescent-shaped volume of interest (VOI) as described previously [28]. VOIs were defined within the PMOD View tool (version 3.5, PMOD Technologies, Zurich, Switzerland). Only tumour volumes consisting

of more than 18 voxels were included, approximating the volumetric PET image resolution.

Extraction of 'percentage volume fractions' and 'percentage volume histograms'

Voxel-wise analysis was performed with an in-house developed software (C++ with integration of the ROOT data analysis framework, version 6.09/01, Cern, Switzerland; and ITK segmentation and registration toolkit, version 4.11, National Library of Medicine). For each voxel within the BTV, the following kinetic and static parameters were determined: the TTP, the late slope (Slope$_{15-40}$, 15–40 min p.i.), and the tumour-to-background ratios TBR$_{5-15}$ and TBR$_{20-40}$ in early 5–15 min p.i. and late 20–40 min p.i. summation images, with the BG signal derived from the respective time frame. The Slope$_{15-40}$ was estimated by linear fitting of the last three time points, and the TTP was estimated as the time corresponding to the maximal TAC value starting from 2.7 min p.i. to avoid influence from early blood signal. Within the BTV, the sub-volume fractions consisting of voxels with a specific parameter value were determined and stored in histograms. For this, the histograms were plotted with the binned parameter values on the *x*-axis (histogram bin sizes: time frames of dynamic PET images for TTP, 0.6 SUV/h for Slope$_{15-40}$, and 0.25 for TBR) and the percentage fractions of the total BTV on the *y*-axis (percentage volume fractions, PVFs). Cumulated percentage volume histograms (PVHs) were obtained by cumulating these PVF histograms up to the specific bin, to improve the robustness of parameter effect quantification [29, 30]. For example PVF$_{TTP15-20}$ corresponds to the percentage portion of voxels within the BTV with peak value in time frame 14 (15–20 min p.i.), and PVH$_{TTP < 20}$ to the cumulated percentage portion of voxels with TTP < 20 min p.i.. In order to exemplarily illustrate the influence of noise in dynamic PET data onto the estimation of parametric TTP and Slope$_{15-40}$ images, a simple method for noise reduction, a spatial Gaussian filter with 10 mm full width half maximum (FWHM), was applied to the dynamic PET data prior to the estimation and analysis of alternative TTP and Slope$_{15-40}$ images.

Extraction of VOI-based parameters

For comparison, the following parameters were assessed: TBR$_{5-15,mean}$ and TBR$_{20-40,mean}$ from a mean VOI-TAC (TBR$_{20-40}$ > 1.6) and the maximal TBR$_{5-15,max}$ and TBR$_{20-40,max}$. The VOI for dynamic analysis with TTP and late Slope$_{15-40}$ was obtained with an isocontour set to 90% of maximum uptake in 10–30 min p.i. summation images, yielding a mean TAC characterising the tumour hot-spot [17, 22].

Statistical analysis

Results are presented as mean value and standard deviation. Statistical analysis was performed with IBM SPSS Statistics (version 24, IBM Corp., Armonk, NY, USA). The threshold for sub-volume fractions defined in the PVH of each derived parameter was optimised by evaluating the overall group differences using the Kruskal-Wallis *H* test. Differences between three groups (molecular genetic sub-groups or WHO grades) were assessed with the Kruskal-Wallis *H* test (effect size, *r* = $\sqrt{H^2/(N-1)}$, where *H* is the test statistic and *N* the sample size)). This was followed by Dunn-Bonferroni post-hoc analysis for the extraction of significant differences between two groups (effect size, *r* = |Z|/$\sqrt{N}$, where *Z* is the *Z* score and *N* the sample size). Receiver-operating characteristics (ROC) analysis was performed in order to determine the cut-off values for distinguishing *IDH*-wt from *IDH*-mut gliomas and WHO grade III/ IV from WHO grade II gliomas. For each test, the threshold (T) yielding the highest product of sensitivity (Se) and specificity (Sp) was chosen as optimal cut-off value. Additionally, *H* test and post hoc analysis were performed for sub-groups separated according to both molecular genetic and histologic features. Differences between WHO grades II and III of *IDH*-mut codel gliomas (i.e. no WHO grade IV) were assessed with Mann-Whitney *U* test.

The similarity between two sub-volume fractions was quantified with the Sørensen-Dice coefficient, i.e. two times the intersection volume divided by the sum of both volumes (2 × (volume$_1$ ∩ volume$_2$)/(volume$_1$ + volume$_2$)). Statistical significance was defined as two-tailed *p* value below 0.05.

Results

Patients

One hundred twelve patients had a biopsy, and 40 patients underwent a microsurgical tumour resection. In sum, 39 *IDH*1/2-mutant and 1p/19q-codeleted oligodendrogliomas (*IDH*-mut codel), 39 *IDH*1/2-mutant astrocytomas (*IDH*-mut non-codel), 39 *IDH*1/2-wildtype astrocytomas (*IDH*-wt), 6 *IDH*1/2-mutant glioblastomas (GBM *IDH*-mut), and 39 *IDH*1/2-wildtype glioblastomas (GBM *IDH*-wt) were included. Histologic evaluation revealed 55 WHO grade II gliomas, 62 WHO grade III gliomas, and 45 WHO grade IV gliomas. The patient characteristics are given in Table 1.

Statistical analysis

The VOI-based parameters and voxel-based PVHs are presented with respect to WHO grade differentiation (Table 2), molecular genetic differentiation (Table 3), and a combination of both (Table 4). All tables show mean and standard deviation of the parameters.

Vomacka *et al. EJNMMI Research* (2018) 8:91

Page 4 of 13

Table 1 Patient characteristics

Patients	162
Gender (f; m)	67; 95
Age (year)	49 ± 15
Procedure for diagnosis	
Biopsy	122
Surgery	40
WHO grade	
II	55
III	62
IV	45
Molecular genetic and histologic classification	
IDH-mut, non-codel (WHO II; III)	39 (19; 20)
IDH-mut, codel (WHO II; III)	39 (24; 15)
IDH-wt (WHO II; III)	39 (12; 27)
GBM *IDH*-mut	6
GBM *IDH*-wt	39

Significance of differences in parameters was predominantly higher for PVH data compared to VOI-based parameters especially in case of molecular genetic differentiation and for differences between WHO grade II and WHO grade III/ IV gliomas. In the following, the respective results for (1) VOI-based and (2) voxel-based analyses are presented. Mean values and results from Kruskal-Wallis H test are presented in Tables 2, 3, and 4 with post hoc results coded with upperscript signs (a

complete list of results is given in Additional file 1: Table S1, results from ROC analysis are illustrated in Additional file 1: Table S2).

VOI-based parameters

Figure 1 shows the mean TACs of tumour hotspots (90% isocontour) which were used for dynamic analysis separated according to molecular genetic and histologic features. The mean and standard deviation of the parameters are given in the upper parts of Tables 2, 3, and 4.

All considered VOI-based parameters yielded significant differences ($p < 0.001$) between WHO grades (Table 2), with the highest effect size for $TBR_{5-15,mean}$ ($r = 0.53$). $TBR_{20-40,max}$ was not able to differentiate between WHO grade II and III gliomas ($P = 0.053$, $r = 0.19$), and the effect size for $TBR_{20-40,mean}$ was low ($P = 0.023$, $r = 0.21$). The highest effect size for distinguishing WHO grade III from II was found for the TTP ($P < 0.001$, $r = 0.30$, AUC = 0.70, for $T = 21$ min p.i.: Se = 69%, Sp = 67%), and $TBR_{5-15,mean}$ ($P < 0.001$, $r = 0.37$, AUC = 0.76, for $T = 1.9$: Se = 77%, Sp = 67%). The differences between WHO grades II and IV were strongly significant for all parameters ($P < 0.001$) with highest effect size for $TBR_{5-15,max}$ ($r = 0.49$, AUC = 0.86, for $T = 3.4$: Se = 91%, Sp = 78%) and $TBR_{5-15,mean}$ ($r = 0.51$, AUC = 0.87 for $T = 2.1$: Se = 84%, Sp = 80%). TTP, $Slope_{15-40}$, and $TBR_{5-15,mean}$ were not able to differentiate between WHO grades III and IV ($P = 0.957$, $r = 0.08$; $P = 0.554$, $r = 0.10$; $P = 0.091$, $r = 0.17$), and the most significant differences were found for $TBR_{20-40,max}$ ($P = 0.002$, $r = 0.27$, AUC = 0.69, for $T = 3.0$: Se = 80%, Sp = 56%).

Table 2 TTP (units: min p.i.), $Slope_{15-40}$ (units: SUV/h), TBR (units: 1), and BTV_{20-40} (units: mL) from VOI-based analysis and voxel-wise PVH (units: %) separated according to histologic grading

Tumour VOI, post-filtering	Parameter	WHO II (55)	WHO III (62)	WHO IV (45)	H test P; r	Post hoc
90% isocontour	TTP	25 ± 8	19 ± 9	17 ± 8	< 0.001; 0.39	*°
	$Slope_{15-40}$	− 0.0 ± 0.9	− 0.9 ± 1.6	− 1.0 ± 1.2	< 0.001; 0.36	*°
$TBR_{20-40} > 1.6$	$TBR_{5-15,max}$	2.9 ± 1.1	3.9 ± 1.6	4.6 ± 1.2	< 0.001; 0.50	*°#
	$TBR_{5-15,mean}$	1.8 ± 0.3	2.2 ± 0.5	2.4 ± 0.4	< 0.001; 0.53	*°
	$TBR_{20-40,max}$	2.8 ± 0.9	3.4 ± 1.3	4.0 ± 1.0	< 0.001; 0.43	°#
	$TBR_{20-40,mean}$	1.9 ± 0.2	2.1 ± 0.4	2.2 ± 0.3	< 0.001; 0.43	*°#
	BTV_{20-40}	15 ± 16	26 ± 30	36 ± 25	< 0.001; 0.38	°#
	$PVH_{TBR,5-15 > 2}$	25 ± 24	53 ± 27	64 ± 18	< 0.001; 0.55	*°
	$PVH_{TBR,20-40 > 2}$	26 ± 21	37 ± 24	51 ± 17	< 0.001; 0.43	*°#
	$PVH_{TTP > 30}$	50 ± 23	32 ± 23	25 ± 15	< 0.001; 0.43	*°
	$PVH_{TTP < 15}$	11 ± 14	26 ± 25	31 ± 15	< 0.001; 0.47	*°
	$PVH_{TTP < 20}$	23 ± 20	45 ± 29	52 ± 18	< 0.001; 0.49	*°
	$PVH_{Slope < 0}$	25 ± 19	46 ± 27	50 ± 17	< 0.001; 0.47	*°
$TBR_{20-40} > 1.6$, 10 mm Gauss	$PVH_{GaussTTP > 30}$	67 ± 28	41 ± 34	32 ± 23	< 0.001; 0.44	*°
	$PVH_{Gauss\ TTP < 20}$	13 ± 20	39 ± 34	44 ± 24	< 0.001; 0.51	*°
	$PVH_{Gauss,Slope < 0}$	16 ± 23	45 ± 36	51 ± 26	< 0.001; 0.50	*°

Post hoc $P < 0.05$: WHO grade * II vs. III, ° II vs. IV, # III vs. IV

Vomacka *et al. EJNMMI Research* (2018) 8:91

Page 5 of 13

Table 3 Data shown as in Table 2, separated according to molecular genetic grading

Tumour VOI, post-filtering	Parameter	IDH-mut non-codel (45)	IDH-mut codel (39)	IDH-wt (78)	H-test P; r	Post hoc
90% isocontour	TTP	25 ± 8	23 ± 9	16 ± 8	< 0.001; 0.45	Δx
	Slope$_{15-40}$	-0.2 ± 1.5	-0.2 ± 1.0	-1.1 ± 1.3	< 0.001; 0.44	Δx
TBR$_{20-40}$ > 1.6	TBR$_{5-15,max}$	3.3 ± 1.5	3.5 ± 1.7	4.2 ± 1.3	< 0.001; 0.37	Δx
	TBR$_{5-15,mean}$	2.0 ± 0.5	2.0 ± 0.5	2.4 ± 0.4	< 0,001; 0.45	Δx
	TBR$_{20-40,max}$	3.2 ± 1.2	3.2 ± 1.4	3.5 ± 1.1	0.060; 0.19	
	TBR$_{20-40,mean}$	2.0 ± 0.3	2.1 ± 0.4	2.1 ± 0.3	0.074; 0.18	
	BTV$_{20-40}$	21 ± 22	28 ± 32	26 ± 24	0.347; 0.11	
	PVH$_{TBR,5-15 > 2}$	32 ± 27	32 ± 26	62 ± 23	< 0.001; 0.52	Δx
	PVH$_{TBR,20-40 > 2}$	33 ± 23	33 ± 25	41 ± 22	0.071; 0.18	
	PVH$_{TTP > 30}$	47 ± 21	50 ± 18	23 ± 20	< 0.001; 0.57	Δx
	PVH$_{TTP < 15}$	12 ± 13	10 ± 9	34 ± 22	< 0.001; 0.56	Δx
	PVH$_{TTP < 20}$	26 ± 20	24 ± 14	56 ± 25	< 0.001; 0.58	Δx
	PVH$_{Slope < 0}$	27 ± 20	25 ± 14	55 ± 23	< 0.001; 0.58	Δx
TBR$_{20-40}$ > 1.6, 10 mm Gauss	PVH$_{GaussTTP > 30}$	62 ± 30	67 ± 24	29 ± 28	< 0.001; 0.55	Δx
	PVH$_{Gauss\ TTP < 20}$	17 ± 22	12 ± 13	50 ± 31	< 0.001; 0.56	Δx
	PVH$_{Gauss,Slope < 0}$	21 ± 26	15 ± 16	56 ± 32	< 0.001; 0.57	Δx

Post hoc P < 0.05: [+]IDH-mut non-codel vs. IDH-mut codel, [Δ]IDH-mut non-codel vs. IDH-wt, [x]IDH-mut codel vs. IDH-wt

Molecular genetic differentiation (Table 3) was strongly significant ($P < 0.001$) for TTP ($r = 0.45$), Slope$_{15-40}$ ($r = 0.44$), TBR$_{5-15,max}$ ($r = 0.37$), and TBR$_{5-15,mean}$ ($r = 0.45$). Differences in TBR$_{20-40,max}$ and in TBR$_{20-40,mean}$ were not significant ($P = 0.056$, $r = 0.19$; $P = 0.075$, $r = 0.18$). None of the parameters differentiated IDH-mut non-codel and codel gliomas ($P > 0.846$, $r < 0.08$). Differences between IDH-mut non-codel or IDH-mut codel and IDH-wt gliomas exhibited the highest effect size (with $P < 0.001$) for Slope$_{15-40}$ ($r = 0.38$, AUC = 0.75, for $T = -0.4$ SUV/h: Se = 74%, Sp = 69%; $r = 0.34$, AUC = 0.75, for $T = -0.4$ SUV/h: Se = 73%. Sp = 74%) and TBR$_{5-15,mean}$ ($r = 0.39$, AUC = 0.77, for T = 2.1: Se = 78%, Sp = 71%; $r = 0.35$, AUC = 0.76, for $T = 2.1$: Se = 78%, Sp = 79%).

Percentage volume fractions and percentage volume histograms

Data from voxel-wise analysis of TTP, Slope$_{15-40}$, and TBR$_{5-15}$ are presented in Figs. 2, 3, and 4. The upper rows depict PVFs, and the middle rows the corresponding cumulated PVFs as PVHs. The red lines represent the PVH cut-offs optimised to yield most significant differences between all glioma entities (minimal P value with Kruskal-Wallis H test). This resulted in the definition of volume fractions considered to be suspicious of aggressive high-grade characteristics: voxels with TTP below 20 min p.i. (PVH$_{TTP < 20}$), negative Slope$_{15-40}$ (PVH$_{Slope < 0}$), TBR$_{5-15}$ above 2 (PVH$_{TBR,5-15 > 2}$), and TBR$_{20-40}$ above 2 (PVH$_{TBR,20-40 > 2}$) (Tables 2, 3, and 4 and lower rows of Figs. 2, 3, and 4. Additionally, the

PVH values for TTP above 30 min p.i. and below 15 min p.i. were included (PVH$_{TTP > 30}$, PVH$_{TTP < 15}$).

All PVH-based parameters showed strongly significant differences between the WHO grades ($P < 0.001$), with the highest effect size for PVH$_{TBR,5-15 > 2}$ ($r = 0.55$) (Table 2). The differentiation of WHO grades II and III and WHO grades II and IV remained strongly significant ($P < 0.001$) for all PVH-based parameters except for PVH$_{TBR,20-40 > 2}$ (WHO grade II vs. III: $P = 0.022$, $r = 0.21$). Effect size was again the highest for PVH$_{TBR,5-15 > 2}$ (distinguish WHO grade III from II: $r = 0.40$, AUC = 0.77, for $T = 39\%$: Se = 73%, Sp = 75%; WHO grade IV from II: $r = 0.53$, AUC = 0.89, for $T = 39\%$: Se = 91%, Sp = 75%). In contrast, differentiation of WHO grade IV from III was only significant for PVH$_{TBR,20-40 > 2}$ ($P = 0.007$, $r = 0.24$, AUC = 0.66, for $T = 44\%$, Se = 69%, Sp = 61%).

All PVH data except PVH$_{TBR,20-40 > 2}$ ($P = 0.072$, $r = 0.18$) yielded strongly significant ($P < 0.001$) differences between molecular genetic groups and remained strongly significant in post hoc analysis of differences between IDH-mut (non-codel; codel) and IDH-wt gliomas. The highest effect size in post hoc analysis was found for PVH$_{TTP < 20}$ ($r = 0.47$, AUC = 0.82, for $T = 38\%$: Se = 77%, Sp = 76%; $r = 0.47$, AUC = 0.86, for $T = 41\%$: Se = 74%, Sp = 90%) and PVH$_{Slope < 0}$ ($r = 0.47$, AUC = 0.81, for $T = 31\%$: Se = 86%, Sp = 71%; $r = 0.48$, AUC = 0.86, for $T = 40\%$: Se = 77%, Sp = 90%).
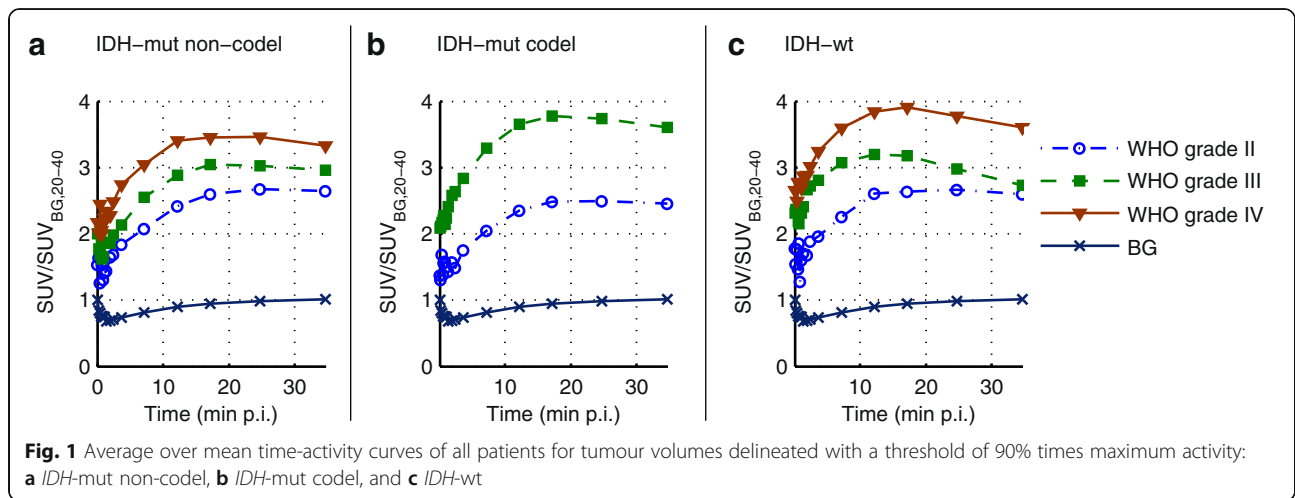
For a more precise interpretation of the results, glioma types were also separated according to both molecular genetic and histologic features (Table 4). As expected, the mean fraction with early peak (PVH$_{TTP < 20}$) and

Vomacka *et al. EJNMMI Research* (2018) 8:91

Page 6 of 13

Table 4 Data shown as in Table 2, separated according to molecular genetic and histologic grading

Tumour VOI, post-filtering	Parameter	IDH-mut non-codel			Post hoc	IDH-mut codel		U test	IDH-wt			Post hoc
		II (19)	III (20)	IV (6)		II (24)	III (15)		II (12)	III (27)	IV (39)	
90% isocontour	TTP	28 ± 7	$24 \pm 8^\Delta$	21 ± 11		24 ± 8	22 ± 10		22 ± 10	$14 \pm 5^\Delta$	17 ± 7	
	$Slope_{15-40}$	0.2 ± 1.0	$-0.4 \pm 1.9^\Delta$	-0.6 ± 1.3		-0.1 ± 0.6	-0.4 ± 1.5^x		-0.2 ± 1.3	$-1.5 \pm 1.2^{\Delta x}$	-1.1 ± 1.2	$*°$
$TBR_{20-40} > 1.6$	$TBR_{5-15,max}$	2.9 ± 1.2	3.4 ± 1.7	4.1 ± 1.2	°	2.9 ± 0.9	4.5 ± 2.1	*	3.2 ± 1.2	4.0 ± 1.2	4.7 ± 1.2	°
	$TBR_{5-15,mean}$	1.8 ± 0.4	$2.0 \pm 0.6^\Delta$	2.2 ± 0.4		1.8 ± 0.2	2.3 ± 0.6	*	2.0 ± 0.4	$2.4 \pm 0.4^\Delta$	2.4 ± 0.4	°
	$TBR_{20-40,max}$	2.9 ± 1.0	3.2 ± 1.4	3.7 ± 0.9		2.7 ± 0.8	4.0 ± 1.7	*	2.8 ± 1.0	3.1 ± 0.9	4.0 ± 1.0	$°\#$
	$TBR_{20-40,mean}$	1.9 ± 0.3	2.1 ± 0.4	2.1 ± 0.2		1.9 ± 0.2	2.3 ± 0.5	*	1.9 ± 0.2	2.0 ± 0.2	2.2 ± 0.3	$°\#$
	BTV_{20-40}	14 ± 14	22 ± 26	36 ± 21		16 ± 16	47 ± 42	*	17 ± 18	17 ± 19	35 ± 26	$°\#$
	$PVH_{TBR,5-15 > 2}$	21 ± 23	$37 \pm 26^\Delta$	52 ± 27	°	21 ± 20	49 ± 25	*	40 ± 30	$67 \pm 22^\Delta$	66 ± 16	$*°$
	$PVH_{TBR,20-40 > 2}$	26 ± 22	36 ± 26	44 ± 14		24 ± 20	48 ± 27	*	27 ± 20	32 ± 21	52 ± 18	$°\#$
	$PVH_{TTP > 30}$	57 ± 18	$42 \pm 20^\Delta$	34 ± 22		51 ± 19	48 ± 17^x		39 ± 32	$16 \pm 18^{\Delta x}$	24 ± 13	$*\#$
	$PVH_{TTP < 15}$	7 ± 8	$14 \pm 14^\Delta$	23 ± 14	°	10 ± 9	12 ± 9^x		21 ± 22	$44 \pm 26^{\Delta x}$	32 ± 15	*
	$PVH_{TTP < 20}$	17 ± 14	$30 \pm 20^\Delta$	43 ± 22	°	22 ± 14	27 ± 15^x		36 ± 32	$67 \pm 25^{\Delta x}$	54 ± 18	$*\#$
	$PVH_{Slope < 0}$	18 ± 15	$31 \pm 19^\Delta$	43 ± 24	°	23 ± 12	28 ± 15^x		39 ± 29	$66 \pm 23^{\Delta x}$	51 ± 16	$*\#$
$TBR_{20-40} > 1.6$, 10 mm Gauss	$PVH_{Gauss TTP > 30}$	76 ± 22	$55 \pm 30^\Delta$	44 ± 35		69 ± 23	64 ± 25^x		49 ± 39	$17 \pm 27^{\Delta x}$	31 ± 20	$*\#$
	$PVH_{Gauss TTP < 20}$	7 ± 13	$22 \pm 23^\Delta$	36 ± 26	$*°$	10 ± 12	17 ± 15^x		28 ± 33	$65 \pm 32^{\Delta x}$	46 ± 24	$*\#$
	$PVH_{Gauss,Slope < 0}$	9 ± 15	$26 \pm 28^\Delta$	42 ± 35	°	12 ± 14	21 ± 18^x		34 ± 37	$72 \pm 32^{\Delta x}$	52 ± 24	$*\#$

Post hoc $P < 0.05$: [+]IDH-mut non-codel vs. IDH-mut codel, [Δ]IDH-mut non-codel vs. IDH-wt, [x]IDH-mut codel vs. IDH-wt; WHO grade * II vs. III, ° II vs. IV, # III vs. IV

Vomacka *et al. EJNMMI Research* (2018) 8:91

Page 7 of 13

Fig. 1 Average over mean time-activity curves of all patients for tumour volumes delineated with a threshold of 90% times maximum activity:
a *IDH*-mut non-codel, **b** *IDH*-mut codel, and **c** *IDH*-wt

negative slope ($PVH_{Slope < 0}$) was slightly increased (not significant) in WHO grade IV compared to that in WHO grade III for *IDH*-mut non-codel gliomas. However, in the case of *IDH*-wt gliomas, the fraction of voxels with an early peak ($PVH_{TTP < 20}$: $P = 0.035$, $r = 0.29$)

and negative slope ($PVH_{Slope < 0}$: $P = 0.010$, $r = 0.33$) was significantly higher in WHO grade III compared to that in WHO grade IV gliomas. Simultaneously, $PVH_{TBR,20-40 > 2}$ was significantly higher in *IDH*-wt GBMs ($P = 0.001$, $r = 0.42$).

Fig. 2 The upper row shows the average percentage volume fractions of the TTP (PVF_{TTP}), i.e. the percentage portion of voxels with TTP in the respective time frame. In the middle row, the corresponding cumulated histograms (PVH_{TTP}) are presented, i.e. the percentage portion of voxels with TTP below a certain value. The most significant differences between groups were found for $PVH_{TTP < 20}$ (with the cut-off value TTP < 20 min p.i. marked with red lines). The lower row depicts the boxplots of $PVH_{TTP < 20}$. **a** *IDH*-mut non-codel. **b** *IDH*-mut codel. **c** *IDH*-wt

Vomacka *et al. EJNMMI Research* (2018) 8:91

Page 8 of 13

Fig. 3 Data presented as in Fig. 2, with average percentage volume fractions of the slope (PVF$_{Slope}$), the corresponding cumulated histograms (PVH$_{Slope}$), and the boxplots of PVH data with slope < 0 SUV/h (PVH$_{Slope < 0 \, SUV/h}$). **a** *IDH*-mut non-codel. **b** *IDH*-mut codel. **c** *IDH*-wt

The application of the exemplary Gaussian filter (10 mm FWHM) yielded a comparable ability to differentiate WHO grades and molecular genetic groups, as reported in Tables 2, 3, and 4 and Additional file 1: Tables S1 and S2. However, a tendency of this spatial filtering to reduce the fraction of voxels exhibiting an early peak or negative slope was observed (Additional file 1: Figure S1).

Spatial correlation of sub-volume fractions

The Sørensen-Dice coefficient, quantifying similarity of the sub-volume fractions, was 0.72 between volumes with TTP < 20 min p.i. and with negative Slope$_{15-40}$, indicating a high overlap of both properties. The Sørensen-Dice coefficients of sub-volumes derived from the static parameter TBR$_{5-15 > 2}$ with sub-volumes derived from kinetic parameters (TTP < 20 min p.i. or negative Slope$_{15-40}$) were 0.50 and 0.48. The corresponding coefficients for the later TBR (TBR$_{20-40 > 2}$) sub-volume were 0.33 and 0.35.

Figure 5 shows the T$_1$-weighted MRI images, TBR$_{5-15}$ and TBR$_{20-40}$ images, and parametric maps of TTP and

Slope$_{15-40}$ for two typical WHO grade II gliomas (non-codel and codel) and one *IDH*-wt WHO grade III glioma. Additionally, an exemplary tumour with heterogeneous pattern in parametric maps is displayed (classified by biopsy as *IDH*-mut codel WHO grade II glioma), where the maximum uptake in TBR images does not co-localise with the hot-spot in early TTP and negative Slope$_{15-40}$ images.

Discussion

In this study, we established an automated and reader-independent method for voxel-wise ^{18}F-FET PET glioma analysis, which enables a fast identification of sub-volumes consisting of voxels with aggressive high-grade kinetics. By quantifying the intra-tumoural parameter distribution with percentage volume histograms, we found significant differences between WHO grades and between molecular genetic groups. Both, association with WHO grade and *IDH* mutation status, were higher for PVH data compared to VOI-based parameters in most cases. Interestingly, sub-group analyses showed that in the special case of *IDH*-wt gliomas, the fraction with early peak or negative slope was significantly higher

Vomacka *et al. EJNMMI Research* (2018) 8:91

Page 9 of 13

Fig. 4 Data presented as in Fig. 2, with average percentage volume fractions of the TBR (PVF$_{TBR,5-15}$), the corresponding cumulated histograms (PVH$_{TBR,5-15}$), and the boxplots of PVH data with TBR$_{5-15}$ > 2 (PVH$_{TBR,5-15 > 2}$). **a** *IDH*-mut non-codel. **b** *IDH*-mut codel. **c** *IDH*-wt
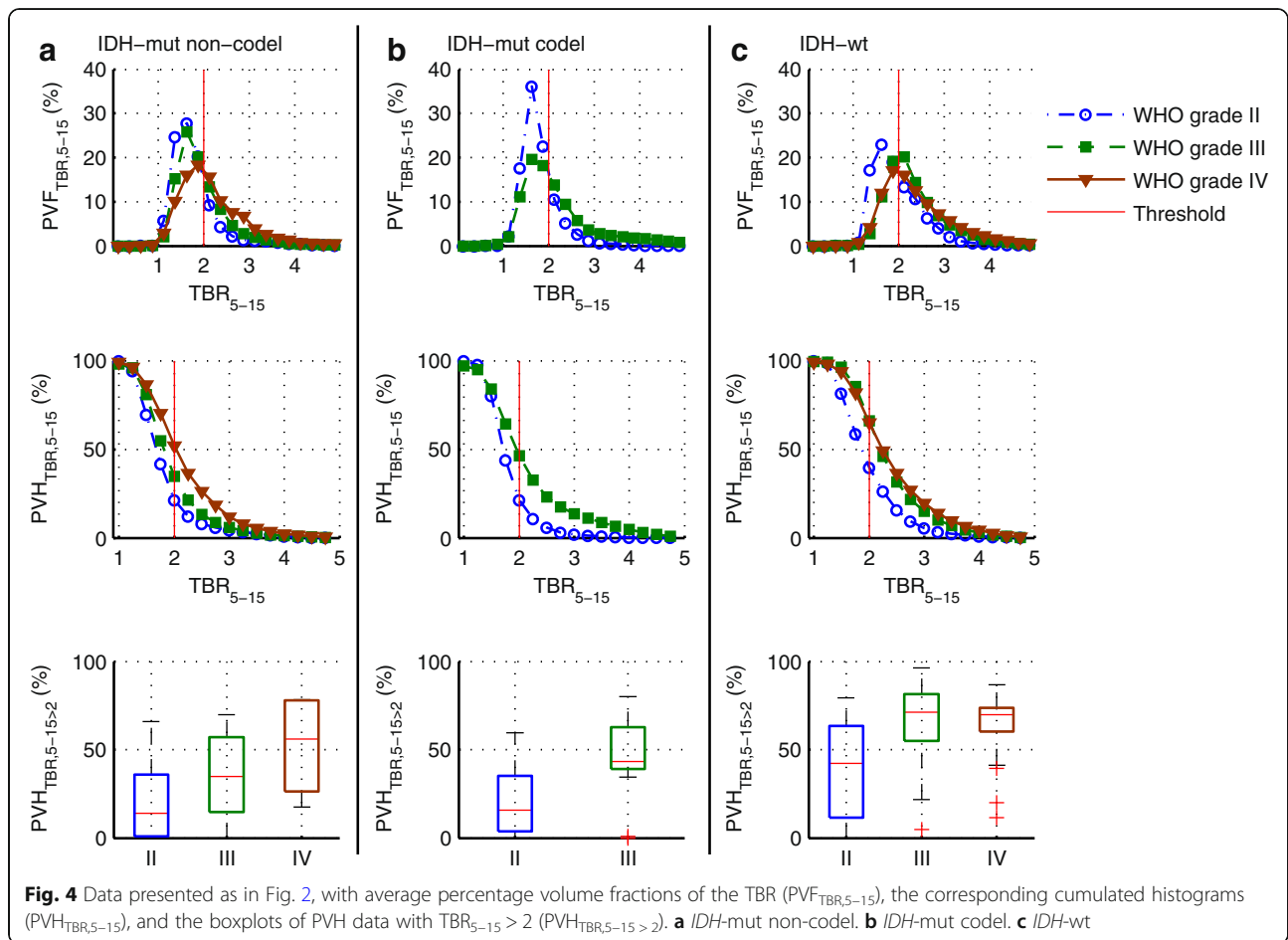
in WHO grade III compared to WHO grade IV gliomas, with simultaneously significantly higher PVH$_{TBR,20-40 > 2}$ in WHO grade IV gliomas. Aggressive sub-volumes defined by TTP < 20 min p.i. and negative Slope$_{15-40}$ showed high overlap with each other, but a low overlap with TBR$_{5-15 > 2}$- and TBR$_{20-40 > 2}$-defined hotspots, indicating a possible complementarity of the investigated kinetic and static parameters. The corresponding parametric images as presented in Fig. 5 may provide valuable information for a fast visual screening of glioma tissue. In summary, this study demonstrates the relevance and suitability of tumour heterogeneity assessment on a voxel basis with static and kinetic ^{18}F-FET PET parameters for a differentiated characterisation of gliomas, although the clinical applicability of parametric 3D information yet requires a comprehensive validation by utilising stereotactic biopsies.

In this context, an elaborate understanding of the underlying processes of ^{18}F-FET uptake is crucial and a matter of current research [20, 31–35]. So far, various studies suggest that regional information from static ^{18}F-FET PET images and from MR-based morphological and functional images is complementary, showing only

moderate overlap and low spatial correlation [36–39]. Still, tissue properties such as rCBV and rCBF might be relevant for the delivery of ^{18}F-FET, potentially influencing ^{18}F-FET uptake behaviour. rCBF was found to correlate significantly with early slope (0–5 min p.i.) in ^{18}F-FET PET and with TBR (20–40 min p.i.), however, not with TAC patterns and late slope (10–50 min p.i.) [40]. Recently, a negative correlation of rCBV and late slope (10–30 min p.i.) and a positive correlation with TBR (10–20 min p.i.) could be shown; however, only a small fraction of the variance of early and late FET uptake could be explained by rCBV [38]. Therefore, it was concluded that rCBV and ^{18}F-FET PET provide congruent and complementary information on the underlying processes. While late TBR may mainly reflect specific trapping within tumour cells, the early TBR and the TAC pattern may be influenced by rCBV and rCBF [38, 41]. Correlation of *IDH* mutation status with MRI parameters has among others shown that *IDH*-wt gliomas tend to exhibit high rCBV values, which is a robust estimate of tumour angiogenesis [32, 35]. In order to retrieve comprehensive information on the underlying processes and their influence on ^{18}F-FET uptake, further

Vomacka *et al. EJNMMI Research* (2018) 8:91

Page 10 of 13
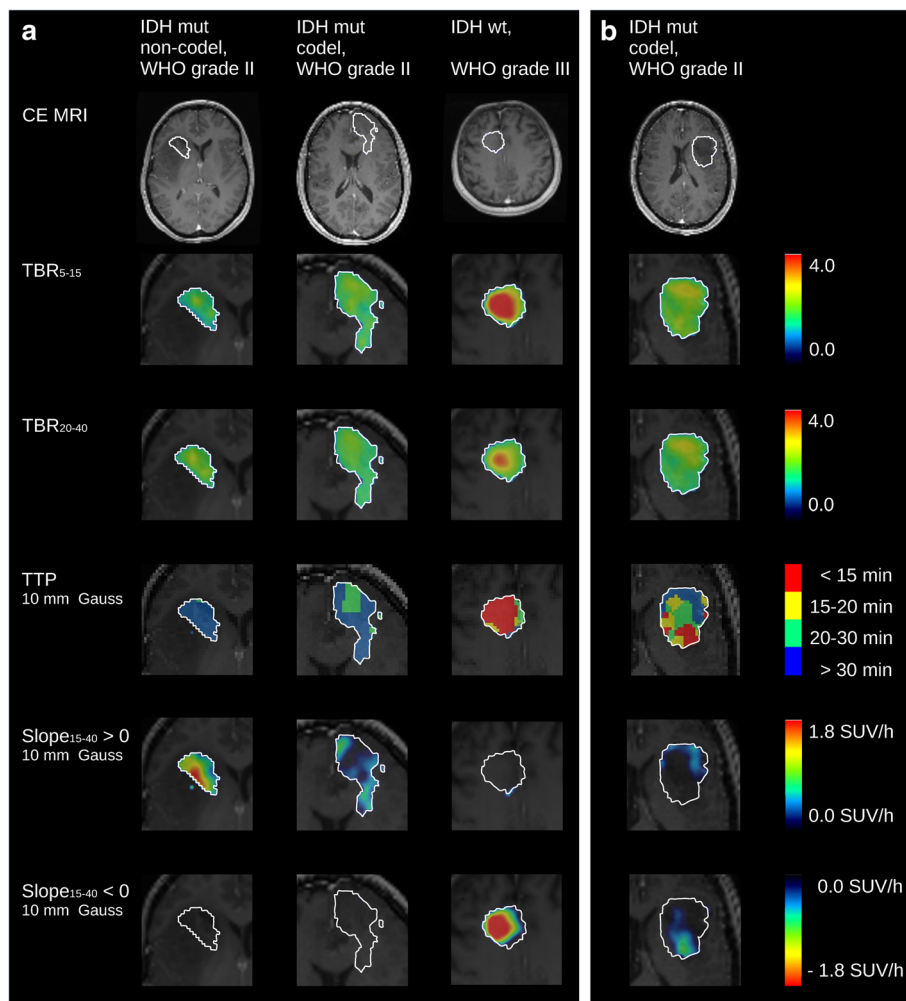
Fig. 5 Contrast-enhanced T$_1$-weighted MRI images of four example patients, and the corresponding parametric images of the early and late TBR, the TTP, and the negative and positive Slope$_{15-40}$ for the voxels within the BTV (zoom factor 2; BTV marked with white contour; TTP and Slope$_{5-15}$ images estimated from dynamic PET data smoothed with a Gaussian with 10 mm FWHM). **a** Images of three example patients with parameter distributions characteristic of one *IDH*-mut non-codel WHO grade II glioma, one *IDH*-mut codel WHO grade II glioma, and one *IDH*-wt WHO grade III glioma. **b** One example patient (*IDH*-mut codel WHO grade II glioma) with a mixed pattern in parametric images, where maximum uptake in TBR images does not co-localise with the hotspot with early TTP and negative Slope$_{15-40}$

investigations may combine information from PWI and pharmacokinetic modelling with dynamic ^{18}F-FET PET data, also considering blocking studies.

Various studies were published evaluating thresholding techniques optimised for the reproduction of true object boundaries in PET images, possibly taking into account different image characteristics [42–45]. The currently established method for BTV definition was verified with at least one biopsy per patient, which was utilised for an optimisation of sensitivity and specificity and resulted in the optimal TBR cut-off of 1.6 [15, 27]. As shown previously in mice, a threshold relying on background and maximal uptake within the tumour is superior for reproduction of histologically proven glioma boundaries [46]. Hence, future studies considering glioma segmentation in humans, possibly further

including information from the characteristic kinetics of the different glioma types, are desirable.

The proposed voxel-wise analysis including TTP and Slope$_{15-40}$ maps and percentage volume histograms of static and kinetic parameters has the potential to provide encompassing information not only for planning of biopsy, surgery, or radiation therapy but also for prognosis, follow-up, and prediction of tumour recurrence based on improved 3D information regarding the local aggressiveness of tumour tissue. In this context, this study has two limitations which need to be addressed in future studies. Firstly, this work would benefit from a correlation analysis of histopathologically assessed tumour heterogeneity and the tumour heterogeneity indicated by the proposed parametric 3D maps. Secondly,

Vomacka *et al. EJNMMI Research* (2018) 8:91

Page 11 of 13

voxel-TACs are prone to noise in dynamic PET data, especially for shorter time frames. In this study, sensitive parameters TTP and Slope$_{15-40}$ were derived directly from single-voxel TACs without the application of TAC smoothing or fitting in order to avoid the introduction of bias, i.e. change in temporal pattern, from TAC pre-processing, and allow for an easy adoption by other research centres. An exemplary simple method for per-frame noise suppression with a spatial Gaussian filter was included and showed that PVH data changed while the ability to differentiate glioma types was preserved, which further underlines the need for stereotactic biopsies. Although the incorporation of a kinetic model which is suitable to describe ^{18}F-FET pharmacokinetics seems conceivable, provided that appropriate blood input data are available, voxel-based fitting of complex models might also be sensitive to noise [19].

The presented data indicate the direct applicability for non-invasive glioma grading and prediction of molecular genetic profile. This is important, since the WHO classification was updated [26], and stratification is now based on molecular genetic information, i.e. *IDH*-wt gliomas are considered as having the same prognosis as glioblastomas themselves. A direct application is the clinical assessment of lesions suspected of glioma, in particular for the selection of the subsequent clinical steps such as biopsy, resection, or "watch and wait", but also for risk-stratification in non-contrast-enhancing gliomas (*IDH*-mut vs. *IDH*-wt). The next steps may further include multi-parametric 3D analysis, machine learning approaches, the evaluation of the influence of small scale motion on voxel-wise analysis, and the assessment of the robustness of alternative methods for the voxel-wise characterisation of gliomas, such as pharmacokinetic modelling or the inclusion of information from other imaging modalities like perfusion-weighted imaging.

Conclusions

Voxel-wise assessment of static and kinetic parameters and partitioning of the entire tumour according to voxel-wise properties enables an improved characterisation of glioma tissue, compared to VOI-based parameters. Moreover, the 3D information might enable a fast visual screening supporting the identification of aggressive sub-volumes, thus guiding individual therapy instrumentation. The correlation between histopathology and the impact on prognosis and prediction of tumour recurrence needs to be evaluated in future studies.

Additional file

Additional file 1: Table S1. *P* values end effect sizes r from post hoc analysis for histologic and molecular genetic differentiation. Effect size *r* is shown colour coded (white-yellow-red continuously scaled from minimal to maximal *r* value). **Table S2.** Area under the curve (AUC) from ROC analysis and the optimal thresholds (*T*) chosen for the highest product of sensitivity (Se, units: %) and specificity (Sp, units: %). Thresholds are given in units of TTP (units: min p.i.), Slope$_{15-40}$ (units: SUV/h), TBR (units: 1), and BTV$_{20-40}$ (units: mL) from VOI-based analysis, and voxel-wise PVH (units: %). AUC is shown colour coded (white-yellow-red continuously scaled from minimal to maximal AUC value). **Figure S1.** Exemplary voxel-wise TACs belonging to the glioma examples shown in Fig. 5. a Voxel-TACs with application of a Gaussian (10 mm FWHM) on dynamic PET data. b Original voxel-TACs without pre-processing of the dynamic PET data. (DOCX 145 kb)

Abbreviations

BG: Background; BTV: Biological tumour volume; FET: O-(2-^{18}F-fluoroethyl)-L-tyrosine; GBM *IDH*-mut: *IDH*1/2-mutant glioblastoma; GBM *IDH*-wt: *IDH*1/2-wildtype glioblastoma; *IDH*-mut codel: *IDH*1/2-mutant and 1p/19q-codeleted oligodendroglioma; *IDH*-mut non-codel: *IDH*1/2-mutant astrocytoma; MRI: Magnetic resonance imaging; PET: Positron emission tomography; PVF: Percentage volume fraction; PVH: Cumulated percentage volume histogram; PWI: Perfusion-weighted imaging; rCBF: Relative cerebral blood flow; rCBV: Relative cerebral blood volume; TAC: Time-activity curve; TBR: Tumour-to-background ratio; TTP: Time-to-peak; VOI: Volume-of-interest

Authors' contributions

LV, MU, SZ, BS, PB, NLA, and GB contributed to the concept and design of the study. LV implemented the voxel-wise analysis, performed the global data and statistical analysis, and drafted the manuscript. EM and GB contributed to the implementation of the voxel-wise analysis. AH, AG, and JB helped with the data analysis. FWK and JCT were in charge of the neuropathological diagnosis according to biopsy or resection. All authors contributed to the drafting of the manuscript, and all authors read and approved the final manuscript.

Ethics approval and consent to participate

The study was authorised by the local ethics committee (IRB 606-16) in accordance with the ICH Guideline for Good Clinical Practice (GCP) and the Declaration of Helsinki. All patients gave written consent to participate in the study.

Consent for publication

Not applicable.

Competing interests

The authors declare that they have no competing interests.

Publisher's Note

Springer Nature remains neutral with regard to jurisdictional claims in published maps and institutional affiliations.

Author details

^{1}Department of Nuclear Medicine, University Hospital, LMU Munich, Marchioninistr. 15, 81377 Munich, Germany. ^{2}German Cancer Consortium (DKTK), Partner site Munich, German Cancer Research Center (DKFZ), Heidelberg, Germany. ^{3}Department of Neurosurgery, University Hospital, LMU Munich, Munich, Germany.

References

1. Arevalo O, Valenzuela R, Esquenazi Y, Rao M, Tran B, Zhu J, et al. The 2016 World Health Organization Classification of Tumors of the Central Nervous System: a practical approach for gliomas, part 2. Isocitrate dehydrogenase status—imaging correlation. Neurographics. 2017;7:344–9.
2. Fouke SJ, Benzinger T, Gibson D, Ryken TC, Kalkanis SN, Olson JJ. The role of imaging in the management of adults with diffuse low grade glioma: a systematic review and evidence-based clinical practice guideline. J Neuro-Oncol. 2015;125:457–79.
3. Ryken TC, Aygun N, Morris J, Schweizer M, Nair R, Spracklen C, et al. The role of imaging in the management of progressive glioblastoma: a

Vomacka *et al. EJNMMI Research* (2018) 8:91

Page 12 of 13

systematic review and evidence-based clinical practice guideline. J Neuro-Oncol. 2014;118:435–60.

4. van den Bent MJ, Wefel JS, Schiff D, Taphoorn MJ, Jaeckle K, Junck L, et al. Response assessment in neuro-oncology (a report of the RANO group): assessment of outcome in trials of diffuse low-grade gliomas. Lancet Oncol. 2011;12:583–93.

5. Heiss P, Mayer S, Herz M, Wester HJ, Schwaiger M, Senekowitsch-Schmidtke R. Investigation of transport mechanism and uptake kinetics of O-(2-[18F]fluoroethyl)-L-tyrosine in vitro and in vivo. J Nucl Med. 1999;40:1367–73.

6. Langen KJ, Jarosch M, Muhlensiepen H, Hamacher K, Broer S, Jansen P, et al. Comparison of fluorotyrosines and methionine uptake in F98 rat gliomas. Nucl Med Biol. 2003;30:501–8.

7. Lopez WO, Cordeiro JG, Albicker U, Doostkam S, Nikkhah G, Kirch RD, et al. Correlation of (18)F-fluoroethyl tyrosine positron-emission tomography uptake values and histomorphological findings by stereotactic serial biopsy in newly diagnosed brain tumors using a refined software tool. Onco Targets Ther. 2015;8:3803–15.

8. Albert NL, Weller M, Suchorska B, Galldiks N, Soffietti R, Kim MM, et al. Response Assessment in Neuro-Oncology working group and European Association for Neuro-Oncology recommendations for the clinical use of PET imaging in gliomas. Neuro-Oncology. 2016;18:1199–208.

9. Langen KJ, Bartenstein P, Boecker H, Brust P, Coenen HH, Drzezga A, et al. German guidelines for brain tumour imaging by PET and SPECT using labelled amino acids. Nuklearmedizin. 2011;50:167–73.

10. Jansen NL, Schwartz C, Graute V, Eigenbrod S, Lutz J, Egensperger R, et al. Prediction of oligodendroglial histology and LOH 1p/19q using dynamic [(18)F]FET-PET imaging in intracranial WHO grade II and III gliomas. Neuro-Oncology. 2012;14:1473–80.

11. Jansen NL, Suchorska B, Wenter V, Eigenbrod S, Schmid-Tannwald C, Zwergal A, et al. Dynamic 18F-FET PET in newly diagnosed astrocytic low-grade glioma identifies high-risk patients. J Nucl Med. 2014;55:198–203.

12. Galldiks N, Stoffels G, Filss C, Rapp M, Blau T, Tscherpel C, et al. The use of dynamic O-(2-18F-fluoroethyl)-l-tyrosine PET in the diagnosis of patients with progressive and recurrent glioma. Neuro-Oncology. 2015;17:1293–300.

13. Jansen NL, Suchorska B, Wenter V, Schmid-Tannwald C, Todica A, Eigenbrod S, et al. Prognostic significance of dynamic 18F-FET PET in newly diagnosed astrocytic high-grade glioma. J Nucl Med. 2015;56:9–15.

14. Lohmann P, Herzog H, Rota Kops E, Stoffels G, Judov N, Filss C, et al. Dual-time-point O-(2-[(18)F]fluoroethyl)-L-tyrosine PET for grading of cerebral gliomas. Eur Radiol. 2015;25:3017–24.

15. Albert NL, Winkelmann I, Suchorska B, Wenter V, Schmid-Tannwald C, Mille E, et al. Early static (18)F-FET-PET scans have a higher accuracy for glioma grading than the standard 20-40 min scans. Eur J Nucl Med Mol Imaging. 2016;43:1105–14.

16. Romagna A, Unterrainer M, Schmid-Tannwald C, Brendel M, Tonn JC, Nachbichler SB, et al. Suspected recurrence of brain metastases after focused high dose radiotherapy: can [18F]FET- PET overcome diagnostic uncertainties? Radiat Oncol. 2016;11:139.

17. Pöpperl G, Kreth FW, Mehrkens JH, Herms J, Seelos K, Koch W, et al. FET PET for the evaluation of untreated gliomas: correlation of FET uptake and uptake kinetics with tumour grading. Eur J Nucl Med Mol Imaging. 2007;34:1933–42.

18. Suchorska B, Giese A, Biczok A, Unterrainer M, Weller M, Drexler M, et al. Identification of time-to-peak on dynamic 18F-FET-PET as a prognostic marker specifically in IDH1/2 mutant diffuse astrocytoma. Neuro-Oncology. 2018;20:279–88.

19. Koopman T, Verburg N, Schuit RC, Pouwels PJW, Wesseling P, Windhorst AD, et al. Quantification of O-(2-[(18)F]fluoroethyl)-L-tyrosine kinetics in glioma. EJNMMI Res. 2018;8:72.

20. Thiele F, Ehmer J, Piroth MD, Eble MJ, Coenen HH, Kaiser HJ, et al. The quantification of dynamic FET PET imaging and correlation with the clinical outcome in patients with glioblastoma. Phys Med Biol. 2009;54:5525–39.

21. Pöpperl G, Kreth FW, Herms J, Koch W, Mehrkens JH, Gildehaus FJ, et al. Analysis of 18F-FET PET for grading of recurrent gliomas: is evaluation of uptake kinetics superior to standard methods? J Nucl Med. 2006;47:393–403.

22. Jansen NL, Graute V, Armbruster L, Suchorska B, Lutz J, Eigenbrod S, et al. MRI-suspected low-grade glioma: is there a need to perform dynamic FET PET? Eur J Nucl Med Mol Imaging. 2012;39:1021–9.

23. Lohmann P, Stoffels G, Ceccon G, Rapp M, Sabel M, Filss CP, et al. Radiation injury vs. recurrent brain metastasis: combining textural feature radiomics

analysis and standard parameters may increase 18F-FET PET accuracy without dynamic scans. Eur Radiol. 2017;27:2916–27.

24. Pyka T, Gempt J, Hiob D, Ringel F, Schlegel J, Bette S, et al. Textural analysis of pre-therapeutic [18F]-FET-PET and its correlation with tumor grade and patient survival in high-grade gliomas. Eur J Nucl Med Mol Imaging. 2016;43:133–41.

25. Unterrainer M, Winkelmann I, Suchorska B, Giese A, Wenter V, Kreth FW, et al. Biological tumour volumes of gliomas in early and standard 20-40 min (18)F-FET PET images differ according to IDH mutation status. Eur J Nucl Med Mol Imaging. 2018;45:1242–9.

26. Louis DN, Perry A, Reifenberger G, von Deimling A, Figarella-Branger D, Cavenee WK, et al. The 2016 World Health Organization Classification of Tumors of the Central Nervous System: a summary. Acta Neuropathol. 2016;131:803–20.

27. Pauleit D, Floeth F, Hamacher K, Riemenschneider MJ, Reifenberger G, Muller HW, et al. O-(2-[18F]fluoroethyl)-L-tyrosine PET combined with MRI improves the diagnostic assessment of cerebral gliomas. Brain. 2005;128:678–87.

28. Unterrainer M, Vettermann F, Brendel M, Holzgreve A, Lifschitz M, Zahringer M, et al. Towards standardization of 18F-FET PET imaging: do we need a consistent method of background activity assessment? EJNMMI Res. 2017;7:48.

29. Kang Y, Choi SH, Kim YJ, Kim KG, Sohn CH, Kim JH, et al. Gliomas: histogram analysis of apparent diffusion coefficient maps with standard- or high-b-value diffusion-weighted MR imaging--correlation with tumor grade. Radiology. 2011;261:882–90.

30. Lee S, Choi SH, Ryoo I, Yoon TJ, Kim TM, Lee SH, et al. Evaluation of the microenvironmental heterogeneity in high-grade gliomas with IDH1/2 gene mutation using histogram analysis of diffusion-weighted imaging and dynamic-susceptibility contrast perfusion imaging. J Neuro-Oncol. 2015;121:141–50.

31. Verger A, Stegmayr C, Galldiks N, Van Der Gucht A, Lohmann P, Stoffels G, et al. Evaluation of factors influencing (18)F-FET uptake in the brain. Neuroimage Clin. 2018;17:491–7.

32. Stadlbauer A, Zimmermann M, Kitzwogerer M, Oberndorfer S, Rossler K, Dorfler A, et al. MR imaging-derived oxygen metabolism and neovascularization characterization for grading and IDH gene mutation detection of gliomas. Radiology. 2017;283:799–809.

33. Richard MA, Fouquet JP, Lebel R, Lepage M. Determination of an optimal pharmacokinetic model of 18F-FET for quantitative applications in rat brain tumors. J Nucl Med. 2017;58:1278–84.

34. Bolcaen J, Lybaert K, Moerman L, Descamps B, Deblaere K, Boterberg T, et al. Kinetic modeling and graphical analysis of 18F-fluoromethylcholine (FCho), 18F-fluoroethyltyrosine (FET) and 18F-fluorodeoxyglucose (FDG) PET for the fiscrimination between high-grade glioma and radiation necrosis in rats. PLoS One. 2016;11:e0161845.

35. Kickingereder P, Sahm F, Radbruch A, Wick W, Heiland S, Deimling A, et al. IDH mutation status is associated with a distinct hypoxia/angiogenesis transcriptome signature which is non-invasively predictable with rCBV imaging in human glioma. Sci Rep. 2015;5:16238.

36. Filss CP, Galldiks N, Stoffels G, Sabel M, Wittsack HJ, Turowski B, et al. Comparison of 18F-FET PET and perfusion-weighted MR imaging: a PET/MR imaging hybrid study in patients with brain tumors. J Nucl Med. 2014;55:540–5.

37. Filss CP, Cicone F, Shah NJ, Galldiks N, Langen KJ. Amino acid PET and MR perfusion imaging in brain tumours. Clin Transl Imaging. 2017;5:209–23.

38. Göttler J, Lukas M, Kluge A, Kaczmarz S, Gempt J, Ringel F, et al. Intra-lesional spatial correlation of static and dynamic FET-PET parameters with MRI-based cerebral blood volume in patients with untreated glioma. Eur J Nucl Med Mol Imaging. 2017;44:392–7.

39. Verger A, Filss CP, Lohmann P, Stoffels G, Sabel M, Wittsack HJ, et al. Comparison of 18F-FET PET and perfusion-weighted MRI for glioma grading: a hybrid PET/MR study. Eur J Nucl Med Mol Imaging. 2017;44:2257.

40. Zhang K, Langen KJ, Neuner I, Stoffels G, Filss C, Galldiks N, et al. Relationship of regional cerebral blood flow and kinetic behaviour of O-(2-(18F-fluoroethyl)-L-tyrosine uptake in cerebral gliomas. Nucl Med Commun. 2014;35:245–51.

41. Kameyama M, Umeda-Kameyama Y. Strategy based on kinetics of O-(2-[(18)F] fluoroethyl)-L-tyrosine ([(18)F] FET). Eur J Nucl Med Mol Imaging. 2016;43:2267–8.

42. Jentzen W, Freudenberg L, Eising EG, Heinze M, Brandau W, Bockisch A. Segmentation of PET volumes by iterative image thresholding. J Nucl Med. 2007;48:108–14.

Vomacka *et al. EJNMMI Research* (2018) 8:91

Page 13 of 13

43. Zaidi H, El Naqa I. PET-guided delineation of radiation therapy treatment volumes: a survey of image segmentation techniques. Eur J Nucl Med Mol Imaging. 2010;37:2165–87.
44. Foster B, Bagci U, Mansoor A, Xu Z, Mollura DJ. A review on segmentation of positron emission tomography images. Comput Biol Med. 2014;50:76–96.
45. Jentzen W. An improved iterative thresholding method to delineate PET volumes using the delineation-averaged signal instead of the enclosed maximum signal. J Nucl Med Technol. 2015;43:28–35.
46. Holzgreve A, Brendel M, Gu S, Carlsen J, Mille E, Boning G, et al. Monitoring of tumor growth with [(18)F]-FET PET in a mouse model of glioblastoma: SUV measurements and volumetric approaches. Front Neurosci. 2016;10:260.

Table S1 *P*-values end effect sizes r from post-hoc analysis for histologic and molecular genetic differentiation. Effect size r is shown colour coded (white-yellow-red continuously scaled from minimal to maximal r value)

| Tumour VOI, post-filtering | Post-hoc | Distinguish WHO grade | | | | | | Distinguish *IDH*-mut codel from *IDH*-mut non-codel | | Distinguish IDH-wt from | | | |
| | | III from II | | IV from II | | IV from III | | | | *IDH*-mut non-codel | | *IDH*-mut codel | |
		P	r	*P*	r	*P*	r	*P*	r	*P*	r	*P*	r
90 % iso-contour	TTP	0.000	0.30	0.000	0.35	0.957	0.08	0.846	0.08	0.000	0.42	0.000	0.30
	Slope$_{15-40}$	0.002	0.27	0.000	0.35	0.554	0.10	1.000	0.02	0.000	0.38	0.000	0.34
	TBR$_{5-15,max}$	0.001	0.28	0.000	0.49	0.008	0.24	1.000	0.05	0.000	0.34	0.002	0.26
	TBR$_{5-15,mean}$	0.000	0.37	0.000	0.51	0.091	0.17	1.000	0.02	0.000	0.39	0.000	0.35
	TBR$_{20-40,max}$	0.053	0.19	0.000	0.43	0.002	0.27	-	-	-	-	-	-
	TBR$_{20-40,mean}$	0.023	0.21	0.000	0.43	0.007	0.24	-	-	-	-	-	-
	BTV$_{20-40}$	0.156	0.15	0.000	0.37	0.007	0.24	-	-	-	-	-	-
TBR$_{20-40}$>1.6	PVH$_{TBR,5-15>2}$	0.000	0.40	0.000	0.53	0.127	0.16	1.000	0.01	0.000	0.43	0.000	0.42
	PVH$_{TBR,20-40>2}$	0.022	0.21	0.000	0.43	0.007	0.24	-	-	-	-	-	-
	PVH$_{TTP>30}$	0.000	0.33	0.000	0.40	0.602	0.10	1.000	0.04	0.000	0.45	0.000	0.48
	PVH$_{TTP<15}$	0.000	0.32	0.000	0.46	0.104	0.17	1.000	0.02	0.000	0.46	0.000	0.46
	PVH$_{TTP<20}$	0.000	0.36	0.000	0.46	0.249	0.14	1.000	0.02	0.000	0.47	0.000	0.47
	PVH$_{Slope<0}$	0.000	0.36	0.000	0.44	0.466	0.11	1.000	0.02	0.000	0.47	0.000	0.48
TBR$_{20-40}$>1.6, 10 mm Gauss	PVH$_{GaussTTP>30}$	0.000	0.35	0.000	0.40	0.945	0.08	1.000	0.05	0.000	0.43	0.000	0.47
	PVH$_{Gauss TTP<20}$	0.000	0.39	0.000	0.48	0.392	0.12	1.000	0.03	0.000	0.45	0.000	0.47
	PVH$_{Gauss,Slope<0}$	0.000	0.39	0.000	0.46	0.518	0.11	1.000	0.04	0.000	0.45	0.000	0.48

Table S2 Area under the curve (AUC) from ROC analysis and the optimal thresholds (T) chosen for the highest product of sensitivity (Se, units: %) and specificity (Sp, units: %). Thresholds are given in units of TTP (units: min p.i.), $Slope_{15-40}$ (units: SUV/h), TBR (units: 1), and BTV_{20-40} (units: mL) from VOI-based analysis, and voxel-wise PVH (units: %). AUC is shown colour coded (white-yellow-red continuously scaled from minimal to maximal AUC value)

| Tumour VOI, post-filtering | ROC analysis | Distinguish WHO grade | | | | | | | | | Distinguish *IDH*-wt from | | | | | |
| | | III from II | | | IV from II | | | IV from III | | | *IDH*-mut non-codel | | | *IDH*-mut codel | | |
		AUC	T	Se, Sp	AUC	T	Se, Sp	AUC	T	Se, Sp	AUC	T	Se, Sp	AUC	T	Se, Sp
90 % iso-contour	TTP	0.70	<21	69, 67	0.76	<23	78, 67	0.56	<15	47, 66	0.78	<23	78, 64	0.72	<23	78, 51
	$Slope_{15-40}$	0.68	<-0.4	56, 76	0.76	<-0.6	67, 84	0.57	<-0.7	62, 56	0.75	<-0.4	74, 69	0.75	<-0.4	73, 74
	$TBR_{5-15,max}$	0.70	>2.8	74, 58	0.86	>3.4	91, 78	0.68	>3.5	87, 53	0.73	>2.9	85, 62	0.69	>3.5	68, 69
	$TBR_{5-15,mean}$	0.76	>1.9	77, 67	0.87	>2.1	84, 80	0.63	>2.2	71, 56	0.77	>2.1	78, 71	0.76	>2.1	78, 79
	$TBR_{20-40,max}$	0.63	>2.8	56, 67	0.82	>2.8	91, 67	0.69	>3.0	80, 56	0.61	>2.9	67, 58	0.61	>3.0	60, 67
	$TBR_{20-40,mean}$	0.64	>1.9	56, 69	0.82	>1.9	82, 71	0.67	>2.1	62, 66	0.61	>1.9	72, 51	0.60	>1.9	65, 56
	BTV_{20-40}	0.61	>9	69, 55	0.77	>9	93, 55	0.68	>15	78, 58	0.58	>9	78, 47	0.53	>9	78, 56
$TBR_{20-40}>1.6$	$PVH_{TBR,5-15>2}$	0.77	>39	73, 75	0.89	>39	91, 75	0.62	>54	80, 48	0.80	>49	79, 71	0.81	>53	76, 79
	$PVH_{TBR,20-40>2}$	0.64	>31	60, 65	0.83	>31	87, 65	0.66	>44	69, 61	0.61	>29	71, 53	0.60	>43	54, 67
	PVH_{TTP-30}	0.71	<42	68, 67	0.81	<32	76, 78	0.56	<28	69, 55	0.81	<38	82, 71	0.85	<30	74, 90
	PVH_{TTP-15}	0.71	>11	65, 73	0.84	>10	91, 71	0.61	>21	76, 55	0.81	>22	73, 82	0.84	>21	74, 90
	PVH_{TTP-20}	0.74	>28	68, 71	0.86	>29	91, 73	0.59	>41	76, 53	0.82	>38	77, 76	0.86	>41	74, 90
	$PVH_{Slope<0}$	0.73	>29	69, 69	0.84	>40	76, 84	0.57	>42	71, 52	0.81	>31	86, 71	0.86	>40	77, 90
$TBR_{20-40}>1.6$, 10 mm Gauss	$PVH_{Gauss TTP>30}$	0.72	<56	66, 71	0.82	<47	78, 78	0.54	<38	71, 50	0.79	<52	82, 69	0.85	<48	78, 79
	$PVH_{Gauss TTP>20}$	0.75	>10	73, 71	0.87	>10	91, 71	0.57	>30	73, 53	0.80	>31	72, 78	0.85	>30	72, 90
	$PVH_{Gauss,Slope<0}$	0.75	>14	71, 73	0.86	>18	87, 76	0.56	>37	73, 52	0.80	>24	79, 73	0.86	>40	71, 92

2

Figure S1 Exemplary voxel-wise TACs belonging to the glioma examples shown in Figure 5. **a** Voxel-TACs with application of a Gaussian (10 mm FWHM) on dynamic PET data. **b** Original voxel-TACs without pre-processing of the dynamic PET data
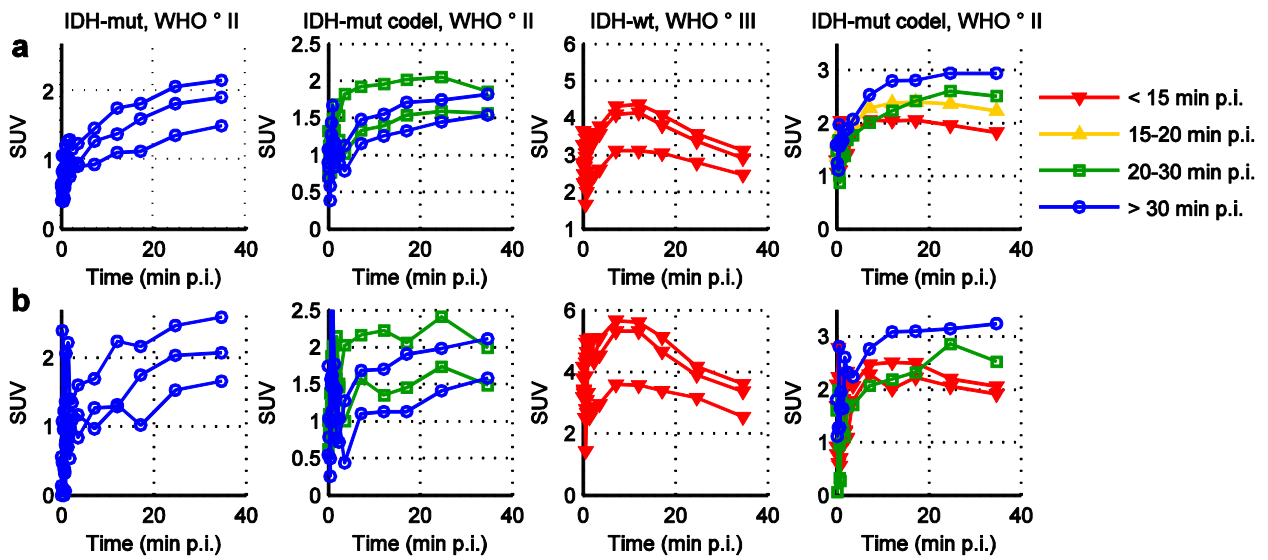
Bibliography

[1] S. R. Cherry, J. A. Sorenson and M. E. Phelps. *Physics in Nuclear Medicine* (Elsevier Health Sciences, 2012).

[2] R. Haubner. "PET radiopharmaceuticals in radiation treatment planning–synthesis and biological characteristics". *Radiother Oncol* 96, 280–287 (2010).

[3] M. Dietlein, K. Kopka and M. Schmidt. *Nuklearmedizin: Basiswissen und klinische Anwendung* (Schattauer Verlag, 2017).

[4] J. Pedroso de Lima. "Nuclear Medicine Physics. sl" (2011).

[5] M. Khalil (ed.) (Springer, 2017).

[6] W. Schlegel and J. Bille. "Medizinische Physik 2". *Medizinische Strahlenphysik* (2002).

[7] A. Sitek and A. M. Celler. "Limitations of Poisson statistics in describing radioactive decay". *Physica Med* 31, 1105–1107 (2015).

[8] M. Bé, V. Chisté, C. Dulieu *et al.* "Table of Radionuclides (vol. 1–4)". *Monographie BIPM* 5 (2008).

[9] C. Champion and C. Le Loirec. "Positron follow-up in liquid water: II. Spatial and energetic study for the most important radioisotopes used in PET". *Phys Med Biol* 52, 6605 (2007).

[10] D. W. Rickey, R. Gordon and W. Huda. "On lifting the inherent limitations of positron emission tomography by using magnetic fields (MagPET)". *Automedica* 14, 355–369 (1992).

[11] R. M. Leahy and J. Qi. "Statistical approaches in quantitative positron emission tomography". *Stat Comp* 10, 147–165 (2000).

[12] Y. Vardi, L. Shepp and L. Kaufman. "A statistical model for positron emission tomography". *J Am Stat Assoc* 80, 8–20 (1985).

[13] H. M. Hudson and R. S. Larkin. "Accelerated image reconstruction using ordered subsets of projection data". *IEEE Trans Med Imaging* 13, 601–609 (1994).

[14] E. J. Hoffman, S.-C. Huang and M. E. Phelps. "Quantitation in positron emission computed tomography: 1. Effect of object size". *Journal Comput Assisted Tomogr* 3, 299–308 (1979).

[15] S.-C. Huang, E. J. Hoffman, M. E. Phelps and D. E. Kuhl. "Quantitation in positron emission computed tomography: 3. Effect of sampling". *Journal Comput Assisted Tomogr* 4, 819–826 (1980).

[16] E. J. Hoffman, S.-C. Huang, D. Plummer and M. E. Phelps. "Quantitation in positron emission computed tomography: 6. effect of nonuniform resolution". *Journal Comput Assisted Tomogr* 6, 987–999 (1982).

[17] A. Attarwala, D. Hardiansyah, C. Romanó *et al.* "A Method for Point Spread Function Estimation for Accurate Quantitative Imaging". *IEEE Trans Nucl Sci* 65, 961–969 (2018).

[18] M. Soret, S. L. Bacharach and I. Buvat. "Partial-volume effect in PET tumor imaging". *J Nucl Med* 48, 932 (2007).

[19] K. Erlandsson, I. Buvat, P. H. Pretorius, B. A. Thomas and B. F. Hutton. "A review of partial volume correction techniques for emission tomography and their applications in neurology, cardiology and oncology". *Phys Med Biol* 57, R119–59 (2012).

[20] O. Munk, L. Tolbod, S. Hansen and T. Bogsrud. "Point-spread function reconstructed PET images of sub-centimeter lesions are not quantitative". *EJNMMI Phys* 4, 5 (2017).

[21] O. G. Rousset, Y. Ma and A. C. Evans. "Correction for partial volume effects in PET: principle and validation". *J Nucl Med* 39, 904–11 (1998).

[22] F. Hofheinz, J. Langner, J. Petr *et al.* "A method for model-free partial volume correction in oncological PET". *EJNMMI Res* 2, 16 (2012).

[23] S. S. Golla, M. Lubberink, B. N. van Berckel, A. A. Lammertsma and R. Boellaard. "Partial volume correction of brain PET studies using iterative deconvolution in combination with HYPR denoising". *EJNMMI Res* 7, 36 (2017).

[24] M. Slifstein and M. Laruelle. "Models and methods for derivation of in vivo neuroreceptor parameters with PET and SPECT reversible radiotracers". *Nucl Med Biol* 28, 595–608 (2001).

[25] A. Bertoldo, G. Rizzo and M. Veronese. "Deriving physiological information from PET images: from SUV to compartmental modelling". *Clin Transl Imaging* 2, 239–251 (2014).

[26] C. S. Patlak, R. G. Blasberg and J. D. Fenstermacher. "Graphical evaluation of blood-to-brain transfer constants from multiple-time uptake data". *J Cereb Blood Flow Metab* 3, 1–7 (1983).

[27] G. Blomqvist. "On the construction of functional maps in positron emission tomography". *J Cereb Blood Flow Metab* 4, 629–632 (1984).

[28] J. Logan, J. S. Fowler, N. D. Volkow *et al.* "Graphical analysis of reversible radioligand binding from time—activity measurements applied to [N-11C-methyl]-(-)-cocaine PET studies in human subjects". *J Cereb Blood Flow Metab* 10, 740–747 (1990).

[29] M. Ichise, H. Toyama, R. B. Innis and R. E. Carson. "Strategies to improve neuroreceptor parameter estimation by linear regression analysis". *J Cereb Blood Flow Metab* 22, 1271–1281 (2002).

[30] A. A. Lammertsma and S. P. Hume. "Simplified reference tissue model for PET receptor studies". *NeuroImage* 4, 153–158 (1996).

[31] K. Chen, D. Bandy, E. Reiman *et al.* "Noninvasive quantification of the cerebral metabolic rate for glucose using positron emission tomography, 18F-fluoro-2-deoxyglucose, the Patlak method, and an image-derived input function". *J Cereb Blood Flow Metab* 18, 716–723 (1998).

[32] R. T. Ogden, F. Zanderigo, S. Choy, J. J. Mann and R. V. Parsey. "Simultaneous estimation of input functions: an empirical study". *J Cereb Blood Flow Metab* 30, 816–826 (2010).

[33] M. A. Mintun, M. E. Raichle, M. R. Kilbourn, G. F. Wooten and M. J. Welch. "A quantitative model for the in vivo assessment of drug binding sites with positron emission tomography". *Annal Neurol* 15, 217–227 (1984).

[34] M. Khalil. *Basic sciences of nuclear medicine* (Springer, 2011).

[35] R. Carson, V. Cunningham, R. Gunn *et al.* "PET pharmacokinetic course manual". *Groningen/Montreal: University of Groningen/McGill University* (2003).

[36] R. N. Gunn, S. R. Gunn, F. E. Turkheimer, J. A. Aston and V. J. Cunningham. "Positron emission tomography compartmental models: a basis pursuit strategy for kinetic modeling". *J Cereb Blood Flow Metab* 22, 1425–1439 (2002).

[37] R. N. Gunn, S. R. Gunn and V. J. Cunningham. "Positron emission tomography compartmental models". *J Cereb Blood Flow Metab* 21, 635–652 (2001).

[38] G. Glatting, P. Kletting, S. N. Reske, K. Hohl and C. Ring. "Choosing the optimal fit function: Comparison of the Akaike information criterion and the F-test". *Med Phys* 34, 4285–4292 (2007).

[39] S. S. Golla, S. M. Adriaanse, M. Yaqub *et al.* "Model selection criteria for dynamic brain PET studies". *EJNMMI Phys* 4, 30 (2017).

[40] R. E. Carson. "Precision and accuracy considerations of physiological quantitation in PET". *J Cereb Blood Flow Metab* 11, A45–A50 (1991).

[41] M. Yaqub, R. Boellaard, M. A. Kropholler and A. A. Lammertsma. "Optimization algorithms and weighting factors for analysis of dynamic PET studies". *Phys Med Biol* 51, 4217 (2006).

[42] N. Sugiura. "Further analysts of the data by akaike's information criterion and the finite corrections". *Commun Statist-Theor Meth* 7, 13–26 (1978).

[43] D. F. Wong, D. Young, P. D. Wilson, C. C. Meltzer and A. Gjedde. "Quantification of neuroreceptors in the living human brain: III. D2-like dopamine receptors: theory, validation, and changes during normal aging". *J Cereb Blood Flow Metab* 17, 316–330 (1997).

[44] R. B. Innis, V. J. Cunningham, J. Delforge *et al.* "Consensus nomenclature for in vivo imaging of reversibly binding radioligands". *J Cereb Blood Flow Metab* 27, 1533–1539 (2007).

[45] E. M. Renkin. "Transport of potassium-42 from blood to tissue in isolated mammalian skeletal muscles". *Am J Physiol* 197, 1205–1210 (1959).

[46] C. Crone. "The permeability of capillaries in various organs as determined by use of the 'indicator diffusion' method". *Acta Physiol Scand* 58, 292–305 (1963).

[47] N. A. Lassen. "Neuroreceptor quantitation in vivo by the steady-state principle using constant infusion or bolus injection of radioactive tracers". *J Cereb Blood Flow Metab* 12, 709–716 (1992).

[48] R. E. Carson, M. A. Channing, R. G. Blasberg *et al.* "Comparison of bolus and infusion methods for receptor quantitation: application to [18F]cyclofoxy and positron emission tomography". *J Cereb Blood Flow Metab* 13, 24–42 (1993).

[49] M. Tonietto, G. Rizzo, M. Veronese *et al.* "Plasma radiometabolite correction in dynamic PET studies: insights on the available modeling approaches". *J Cereb Blood Flow Metab* 36, 326–339 (2016).

[50] W. F. Bowers, S. Fulton and J. Thompson. "Ultrafiltration vs equilibrium dialysis for determination of free fraction". *Clin Pharmacokinet* 9, 49–60 (1984).

[51] M. M. Graham and B. L. Lewellen. "High-speed automated discrete blood sampling for positron emission tomography.". *J Nucl Med* 34, 1357–1360 (1993).

[52] R. Boellaard, A. van Lingen, S. C. van Balen, B. G. Hoving and A. A. Lammertsma. "Characteristics of a new fully programmable blood sampling device for monitoring blood radioactivity during PET". *Eur J Nucl Med* 28, 81–89 (2001).

[53] J. E. Mourik, M. Lubberink, A. Schuitemaker *et al.* "Image-derived input functions for PET brain studies". *Eur J Nucl Med Mol Imaging* 36, 463–471 (2009).

[54] R. A. Bowen and A. T. Remaley. "Interferences from blood collection tube components on clinical chemistry assays". *Biochem Med* 24, 31–44 (2014).

[55] D. Y. Riabkov and E. V. Di Bella. "Estimation of kinetic parameters without input functions: analysis of three methods for multichannel blind identification". *IEEE Trans Biomed Eng* 49, 1318–1327 (2002).

[56] K.-P. Wong, S. R. Meikle, D. D. Feng and M. J. Fulham. "Estimation of input function and kinetic parameters using simulated annealing: application in a flow model". *IEEE Trans Nucl Sci* (2002).

[57] J. E. Mourik, M. Lubberink, U. M. Klumpers *et al.* "Partial volume corrected image derived input functions for dynamic PET brain studies: methodology and validation for [11C]flumazenil". *NeuroImage* 39, 1041–1050 (2008).

[58] D. J. Schlyer, P. O'connor, C. Woody *et al.* "Positron emission tomography wrist detector" (2006). US Patent 7,091,489.

[59] A. Kriplani, D. Schlyer, P. Vaska *et al.* "Feasibility studies for extracting an input function for quantitative positron emission tomography using a wrist scanner". In *Bioengineering Conference, 2007. NEBC'07. IEEE 33rd Annual Northeast*, 51–53 (IEEE, 2007).

[60] B. Ravindranath, S. Junnarkar, M. Purschke *et al.* "3D tomographic wrist scanner for non-invasive determination of input function". In *Nuclear Science Symposium Conference Record (NSS/MIC), 2009 IEEE*, 2917–2919 (IEEE, 2009).

[61] S. Takikawa, V. Dhawan, P. Spetsieris *et al.* "Noninvasive quantitative fluorodeoxyglucose PET studies with an estimated input function derived from a population-based arterial blood curve.". *Radiology* 188, 131–136 (1993).

[62] T. Tsuchida, N. Sadato, Y. Yonekura *et al.* "Rate of glucose using standardized input function". *J Nucl Med* 40, 1441–1445 (1999).

[63] P. Zanotti-Fregonara, K. Chen, J.-S. Liow, M. Fujita and R. B. Innis. "Image-derived input function for brain PET studies: many challenges and few opportunities". *J Cereb Blood Flow Metab* 31, 1986–1998 (2011).

[64] J. Logan. "Graphical analysis of PET data applied to reversible and irreversible tracers". *Nucl Med Biol* 27, 661–670 (2000).

[65] J. Logan. "A review of graphical methods for tracer studies and strategies to reduce bias". *Nucl Med Biol* 30, 833–844 (2003).

[66] C. S. Patlak and R. G. Blasberg. "Graphical evaluation of blood-to-brain transfer constants from multiple-time uptake data. Generalizations". *J Cereb Blood Flow Metab* 5, 584–590 (1985).

[67] M. Slifstein and M. Laruelle. "Effects of statistical noise on graphic analysis of PET neuroreceptor studies". *J Nucl Med* 41, 2083 (2000).

[68] Y. Zhou, W. Ye, J. R. Brašić and D. F. Wong. "Multi-graphical analysis of dynamic PET". *NeuroImage* 49, 2947–2957 (2010).

[69] J. Logan, J. S. Fowler, N. D. Volkow *et al.* "A strategy for removing the bias in the graphical analysis method". *J Cereb Blood Flow Metab* 21, 307–320 (2001).

[70] Y. Zhou, W. Ye, J. R. Brašić *et al.* "A consistent and efficient graphical analysis method to improve the quantification of reversible tracer binding in radioligand receptor dynamic PET studies". *NeuroImage* 44, 661–670 (2009).

[71] G. Blomqvist, S. Pauli, S. Farde *et al.* "Dynamic models for reversible ligand binding". In *Positron emission tomography in clinical research and clinical diagnosis: tracer modelling and radioreceptors* (1989).

[72] V. J. Cunningham, S. P. Hume, G. R. Price *et al.* "Compartmental analysis of diprenorphine binding to opiate receptors in the rat in vivo and its comparison with equilibrium data in vitro". *J Cereb Blood Flow Metab* 11, 1–9 (1991).

[73] R. N. Gunn, A. A. Lammertsma and V. J. Cunningham. *Parametric imaging of ligand-receptor interactions using a reference tissue model and cluster analysis*, 401–406 (Academic Press, 1998).

[74] F. Zanderigo, R. T. Ogden and R. V. Parsey. "Reference region approaches in PET: a comparative study on multiple radioligands". *J Cereb Blood Flow Metab* 33, 888–897 (2013).

[75] C. A. Salinas, G. E. Searle and R. N. Gunn. "The simplified reference tissue model: model assumption violations and their impact on binding potential". *J Cereb Blood Flow Metab* 35, 304–311 (2015).

[76] J. Logan, J. S. Fowler, N. D. Volkow *et al.* "Distribution volume ratios without blood sampling from graphical analysis of PET data". *J Cereb Blood Flow Metab* 16, 834–840 (1996).

[77] S. M. Larson, Y. Erdi, T. Akhurst *et al.* "Tumor treatment response based on visual and quantitative changes in global tumor glycolysis using PET-FDG imaging: the visual response score and the change in total lesion glycolysis". *Clinical Positron Imaging* 2, 159–171 (1999).

[78] P. E. Kinahan and J. W. Fletcher. "Positron emission tomography-computed tomography standardized uptake values in clinical practice and assessing response to therapy". In *Seminars in Ultrasound, CT and MRI*, vol. 31, 496–505 (Elsevier, 2010).

[79] F. H. van Velden, P. Cheebsumon, M. Yaqub *et al.* "Evaluation of a cumulative SUV-volume histogram method for parameterizing heterogeneous intratumoural FDG uptake in non-small cell lung cancer PET studies". *Eur J Nucl Med Mol Imaging* 38, 1636–1647 (2011).

[80] H. Zaidi and I. El Naqa. "PET-guided delineation of radiation therapy treatment volumes: a survey of image segmentation techniques". *Eur J Nucl Med Mol Imaging* 37, 2165–87 (2010).

[81] B. Foster, U. Bagci, A. Mansoor, Z. Xu and D. J. Mollura. "A review on segmentation of positron emission tomography images". *Comput Biol Med* 50, 76–96 (2014).

[82] A. C. Evans, A. L. Janke, D. L. Collins and S. Baillet. "Brain templates and atlases". *NeuroImage* 62, 911–922 (2012).

[83] J. A. van Dalen, A. L. Hoffmann, V. Dicken *et al.* "A novel iterative method for lesion delineation and volumetric quantification with FDG PET". *Nucl Med Commun* 28, 485–493 (2007).

[84] L. Drever, W. Roa, A. McEwan and D. Robinson. "Iterative threshold segmentation for PET target volume delineation". *Med Phys* 34, 1253–1265 (2007).

[85] W. Jentzen, L. Freudenberg, E. G. Eising *et al.* "Segmentation of PET volumes by iterative image thresholding". *J Nucl Med* 48, 108–114 (2007).

[86] W. Jentzen. "An improved iterative thresholding method to delineate PET volumes using the delineation-averaged signal instead of the enclosed maximum signal". *J Nucl Med Technol* 43, 28–35 (2015).

[87] S. Belhassen and H. Zaidi. "A novel fuzzy C-means algorithm for unsupervised heterogeneous tumor quantification in PET". *Medical physics* 37, 1309–1324 (2010).

[88] M. S. Sharif, M. Abbod, A. Amira and H. Zaidi. "Artificial neural network-based system for PET volume segmentation". *J Biomed Imaging* 2010, 4 (2010).

[89] F. E. Turkheimer, P. Edison, N. Pavese *et al.* "Reference and target region modeling of [11C]-(R)-PK11195 brain studies". *J Nucl Med* 48, 158 (2007).

[90] K. J. Friston, J. Ashburner, C. D. Frith *et al.* "Spatial registration and normalization of images". *Hum Brain Mapp* 3, 165–189 (1995).

[91] P. M. Thompson, R. P. Woods, M. S. Mega and A. W. Toga. "Mathematical/computational challenges in creating deformable and probabilistic atlases of the human brain". *Hum Brain Mapp* 9, 81–92 (2000).

[92] A. Hammers, R. Allom, M. J. Koepp *et al.* "Three-dimensional maximum probability atlas of the human brain, with particular reference to the temporal lobe". *Hum Brain Mapp* 19, 224–247 (2003).

[93] I. S. Gousias, D. Rueckert, R. A. Heckemann *et al.* "Automatic segmentation of brain MRIs of 2-year-olds into 83 regions of interest". *NeuroImage* 40, 672–684 (2008).

[94] K. J. Friston, A. P. Holmes, K. J. Worsley *et al.* "Statistical parametric maps in functional imaging: a general linear approach". *Hum Brain Mapp* 2, 189–210 (1994).

[95] K. Friston, J. Ashburner, S. Kiebel, W. Penny and T. Nichols. *Statistical Parametric Mapping: The Analysis of Functional Brain Images.* Academic Press (Elsevier Science, 2007).

[96] A. P. Holmes, R. Blair, J. Watson and I. Ford. "Nonparametric analysis of statistic images from functional mapping experiments". *J Cereb Blood Flow Metab* 16, 7–22 (1996).

[97] K. Friston, C. Frith, P. Liddle *et al.* "The relationship between global and local changes in PET scans". *J Cereb Blood Flow Metab* 10, 458–466 (1990).

[98] K. J. Worsley, S. Marrett, P. Neelin *et al.* "A unified statistical approach for determining significant signals in images of cerebral activation". *Hum Brain Mapp* 4, 58–73 (1996).

[99] K. J. Friston, A. Holmes, J.-B. Poline, C. J. Price and C. D. Frith. "Detecting activations in PET and fMRI: levels of inference and power". *NeuroImage* 4, 223–235 (1996).

[100] P. Lambin, E. Rios-Velazquez, R. Leijenaar *et al.* "Radiomics: extracting more information from medical images using advanced feature analysis". *Eur J Cancer* 48, 441–446 (2012).

[101] P. Lambin, R. T. Leijenaar, T. M. Deist *et al.* "Radiomics: the bridge between medical imaging and personalized medicine". *Nat Rev Clin Oncol* 14, 749 (2017).

[102] Pyradiomics community. "Pyradiomics Documentation" (2018). Release 2.1.0.post7+g167888b.

[103] A. Zwanenburg, S. Leger, M. Vallières, S. Löck *et al.* "Image biomarker standardisation initiative". *arXiv preprint arXiv:1612.07003* (2016).

[104] R. T. Leijenaar, G. Nalbantov, S. Carvalho *et al.* "The effect of SUV discretization in quantitative FDG-PET Radiomics: the need for standardized methodology in tumor texture analysis". *Sci Rep* 5, 11075 (2015).

[105] L. Papp, N. Pötsch, M. Grahovac *et al.* "Glioma survival prediction with combined analysis of in vivo 11C-MET PET features, ex vivo features, and patient features by supervised machine learning". *J Nucl Med* 59, 892–899 (2018).

[106] R. M. Haralick, K. Shanmugam *et al.* "Textural features for image classification". *IEEE Trans Syst Man Cybern* 610–621 (1973).

[107] W. E. Lorensen and H. E. Cline. "Marching cubes: A high resolution 3D surface construction algorithm". In *ACM siggraph computer graphics*, vol. 21, 163–169 (ACM, 1987).

[108] B. Obermeier, R. Daneman and R. M. Ransohoff. "Development, maintenance and disruption of the blood-brain barrier". *Nat Med* 19, 1584 (2013).

[109] B. T. Hawkins and T. P. Davis. "The blood-brain barrier/neurovascular unit in health and disease". *Pharmacol Rev* 57, 173–185 (2005).

[110] N. J. Abbott, L. Rönnbäck and E. Hansson. "Astrocyte–endothelial interactions at the blood–brain barrier". *Nat Rev Neurosci* 7, 41 (2006).

[111] M. V. Sofroniew. "Reactive astrocytes in neural repair and protection". *The Neuroscientist* 11, 400–407 (2005).

[112] W. Risau. "Differentiation of endothelium". *FASEB J* 9, 926–933 (1995).

[113] W. Risau. "Development and differentiation of endothelium". *Kidney Int* 54, S3–S6 (1998).

[114] S. C. Satchell and F. Braet. "Glomerular endothelial cell fenestrations: an integral component of the glomerular filtration barrier". *Am J Physiol Renal Physiol* 296, F947–F956 (2009).

[115] W. M. Deen, M. J. Lazzara and B. D. Myers. "Structural determinants of glomerular permeability". *Am J Physiol Renal Physiol* 281, F579–F596 (2001).

[116] C. Zhao, W. Deng and F. H. Gage. "Mechanisms and functional implications of adult neurogenesis". *Cell* 132, 645–660 (2008).

[117] N. J. Abbott. "Blood–brain barrier structure and function and the challenges for CNS drug delivery". *J Inherit Metab Dis* 36, 437–449 (2013).

[118] D. J. Begley and M. W. Brightman. "Structural and functional aspects of the blood-brain barrier". In *Peptide transport and delivery into the central nervous system*, 39–78 (Springer, 2003).

[119] J. Greenwood. "Mechanisms of blood-brain barrier breakdown". *Neuroradiology* 33, 95–100 (1991).

[120] D. M. McDonald and P. Baluk. "Imaging of angiogenesis in inflamed airways and tumors: newly formed blood vessels are not alike and may be wildly abnormal*: Parker B. Francis Lecture". *Chest* 128, 602S (2005).

[121] L. Claesson-Welsh. "Vascular permeability—the essentials". *Upsala J Med Sci* 120, 135–143 (2015).

[122] J. U. Harrer, G. J. Parker, H. A. Haroon *et al.* "Comparative study of methods for determining vascular permeability and blood volume in human gliomas". *J Magn Reson Imaging* 20, 748–757 (2004).

[123] J. R. Ewing, S. L. Brown, M. Lu *et al.* "Model selection in magnetic resonance imaging measurements of vascular permeability: Gadomer in a 9L model of rat cerebral tumor". *J Cereb Blood Flow Metab* 26, 310–320 (2006).

[124] A. Singh, M. Haris, D. Rathore *et al.* "Quantification of physiological and hemo-dynamic indices using T1 dynamic contrast-enhanced MRI in intracranial mass lesions". *J Magn Reson Imaging* 26, 871–880 (2007).

[125] S. Sourbron, M. Ingrisch, A. Siefert, M. Reiser and K. Herrmann. "Quantification of cerebral blood flow, cerebral blood volume, and blood–brain-barrier leakage with DCE-MRI". *Magn Reson Med* 62, 205–217 (2009).

[126] A. Kassner, T. Roberts, B. Moran, F. Silver and D. Mikulis. "Recombinant tissue plasminogen activator increases blood-brain barrier disruption in acute ischemic stroke: an MR imaging permeability study". *Am J Neuroradiol* 30, 1864–1869 (2009).

[127] A. Kermode, A. Thompson, P. Tofts *et al.* "Breakdown of the blood-brain bar-rier precedes symptoms and other MRI signs of new lesions in multiple sclerosis: pathogenetic and clinical implications". *Brain* 113, 1477–1489 (1990).

[128] M. Ingrisch, S. Sourbron, D. Morhard *et al.* "Quantification of perfusion and permeability in multiple sclerosis: dynamic contrast-enhanced MRI in 3D at 3T". *Invest Radiol* 47, 252–258 (2012).

[129] M. Absinta, D. S. Reich and M. Filippi. "Spring cleaning: time to rethink imaging research lines in MS?". *J Neurol* 263, 1893–1902 (2016).

[130] D. J. Mikulis and T. P. Roberts. "Neuro MR: protocols". *J Magn Reson Imaging* 26, 838–847 (2007).

[131] F. Erdő, L. Denes and E. de Lange. "Age-associated physiological and pathological changes at the blood–brain barrier: a review". *J Cereb Blood Flow Metab* 37, 4–24 (2017).

[132] P. S. Tofts, G. Brix, D. L. Buckley *et al.* "Estimating kinetic parameters from dynamic contrast-enhanced T1-weighted MRI of a diffusable tracer: standardized quantities and symbols". *J Magn Reson Imaging* 10, 223–232 (1999).

[133] D. Israeli, D. Tanne, D. Daniels *et al.* "The application of MRI for depiction of subtle blood brain barrier disruption in stroke". *Int J Biol Sci* 7, 1 (2011).

[134] S. Sourbron and D. L. Buckley. "Tracer kinetic modelling in MRI: estimating perfusion and capillary permeability". *Phys Med Biol* 57, R1 (2011).

[135] A. K. Heye, R. D. Culling, M. d. C. V. Hernández, M. J. Thrippleton and J. M. Wardlaw. "Assessment of blood–brain barrier disruption using dynamic contrast-enhanced MRI. A systematic review". *NeuroImage: Clinical* 6, 262–274 (2014).

[136] T. Tourdias, S. Roggerone, M. Filippi *et al.* "Assessment of disease activity in multiple sclerosis phenotypes with combined gadolinium-and superparamagnetic iron oxide–enhanced MR imaging". *Radiology* 264, 225–233 (2012).

[137] D. J. Brooks, R. P. Beaney, A. A. Lammertsma *et al.* "Quantitative measurement of blood—brain barrier permeability using rubidium-82 and positron emission tomography". *J Cereb Blood Flow Metab* 4, 535–545 (1984).

[138] R. Kessler, J. Goble, J. Bird *et al.* "Measurement of blood-brain barrier permeability with positron emission tomography and [68Ga] EDTA". *J Cereb Blood Flow Metab* 4, 323–328 (1984).

[139] P. Herscovitch, M. E. Raichle, M. R. Kilbourn and M. J. Welch. "Positron emission tomographic measurement of cerebral blood flow and permeability—surface area product of water using [15O] water and [11C] butanol" (1987).

[140] M. Laruelle, M. Slifstein and Y. Huang. "Relationships between radiotracer properties and image quality in molecular imaging of the brain with positron emission tomography". *Mol Imag Biol* 5, 363–375 (2003).

[141] R. N. Waterhouse. "Determination of lipophilicity and its use as a predictor of blood–brain barrier penetration of molecular imaging agents". *Mol Imag Biol* 5, 376–389 (2003).

[142] V. W. Pike. "PET radiotracers: crossing the blood–brain barrier and surviving metabolism". *Trends Pharmacol Sci* 30, 431–440 (2009).

[143] X. Liu, B. J. Smith, C. Chen *et al.* "Use of a physiologically based pharmacokinetic model to study the time to reach brain equilibrium: an experimental analysis of the role of blood-brain barrier permeability, plasma protein binding, and brain tissue binding". *J Pharmacol Exp Ther* 313, 1254–1262 (2005).

[144] U. Bickel. "How to measure drug transport across the blood-brain barrier". *NeuroRx* 2, 15–26 (2005).

[145] Q. Guo, M. Brady and R. N. Gunn. "A biomathematical modeling approach to central nervous system radioligand discovery and development". *J Nucl Med* 50, 1715 (2009).

[146] E. Urich, S. E. Lazic, J. Molnos, I. Wells and P.-O. Freskgård. "Transcriptional profiling of human brain endothelial cells reveals key properties crucial for predictive in vitro blood-brain barrier models". *PLoS One* 7, e38149 (2012).

[147] B. W. Jakoby, Y. Bercier, C. C. Watson, B. Bendriem and D. W. Townsend. "Performance characteristics of a new LSO PET/CT scanner with extended axial field-of-view and PSF reconstruction". *IEEE Trans Nucl Sci* 56, 633–639 (2009).

[148] M. Defrise, P. E. Kinahan, D. W. Townsend *et al.* "Exact and approximate rebinning algorithms for 3-D PET data". *IEEE Trans Med Imaging* 16, 145–158 (1997).

[149] C. Lartizien, C. Comtat, P. E. Kinahan *et al.* "Optimization of injected dose based on noise equivalent count rates for 2-and 3-dimensional whole-body PET". *J Nucl Med* 43, 1268–1278 (2002).

[150] C. Lartizien, P. E. Kinahan and C. Comtat. "A lesion detection observer study comparing 2-dimensional versus fully 3-dimensional whole-body PET imaging protocols". *J Nucl Med* 45, 714 (2004).

[151] D. Pauleit, F. Floeth, K. Hamacher *et al.* "O-(2-[18F] fluoroethyl)-L-tyrosine PET combined with MRI improves the diagnostic assessment of cerebral gliomas". *Brain* 128, 678–687 (2005).

[152] B. Knäusl, A. Hirtl, G. Dobrozemsky *et al.* "PET based volume segmentation with emphasis on the iterative TrueX algorithm". *Z Med Phys* 22, 29–39 (2012).

[153] B. Knäusl, I. F. Rausch, H. Bergmann *et al.* "Influence of PET reconstruction parameters on the TrueX algorithm. A combined phantom and patient study". *Nuklearmedizin* 52, 28–35 (2013).

[154] P. Fasbender and H. W. Kolmel. "Incidence of multiple sclerosis in the urban area of Erfurt, Thuringia, Germany". *Neuroepidemiology* 30, 147–51 (2008).

[155] A. Alonso and M. A. Hernan. "Temporal trends in the incidence of multiple sclerosis: a systematic review". *Neurology* 71, 129–35 (2008).

[156] M. Comabella and S. J. Khoury. "Immunopathogenesis of multiple sclerosis". *Clin Immunol* 142, 2–8 (2012).

[157] M. Filippi, M. A. Rocca, F. Barkhof *et al.* "Association between pathological and MRI findings in multiple sclerosis". *Lancet Neurol* 11, 349–360 (2012).

[158] L. Airas, E. Rissanen and J. O. Rinne. "Imaging neuroinflammation in multiple sclerosis using TSPO-PET". *Clin Transl Imaging* 3, 461–473 (2015).

[159] L. Airas, M. Nylund and E. Rissanen. "Evaluation of Microglial Activation in Multiple Sclerosis Patients Using Positron Emission Tomography". *Front Neurol* 9, 181 (2018).

[160] R. Hinz and R. Boellaard. "Challenges of quantification of TSPO in the human brain". *Clin Transl Imaging* 3, 403–416 (2015).

[161] F. E. Turkheimer, G. Rizzo, P. S. Bloomfield *et al.* "The methodology of TSPO imaging with positron emission tomography". *Biochem Soc Trans* 43, 586–92 (2015).

[162] P. J. Schweitzer, B. A. Fallon, J. J. Mann and J. S. Kumar. "PET tracers for the peripheral benzodiazepine receptor and uses thereof". *Drug Discov Today* 15, 933–42 (2010).

[163] D. R. Owen, R. N. Gunn, E. A. Rabiner *et al.* "Mixed-affinity binding in humans with 18-kDa translocator protein ligands". *J Nucl Med* 52, 24–32 (2011).

[164] D. R. Owen, A. J. Yeo, R. N. Gunn *et al.* "An 18-kDa translocator protein (TSPO) polymorphism explains differences in binding affinity of the PET radioligand PBR28". *J Cereb Blood Flow Metab* 32, 1–5 (2012).

[165] Q. Guo, D. R. Owen, E. A. Rabiner, F. E. Turkheimer and R. N. Gunn. "Identifying improved TSPO PET imaging probes through biomathematics: the impact of multiple TSPO binding sites in vivo". *NeuroImage* 60, 902–910 (2012).

[166] G. Rizzo, M. Veronese, M. Tonietto *et al.* "Kinetic modeling without accounting for the vascular component impairs the quantification of [11C]PBR28 brain PET data". *J Cereb Blood Flow Metab* 34, 1060–1069 (2014).

[167] J. Ashburner, J. Haslam, C. Taylor, V. Cunningham and T. Jones. *A cluster analysis approach for the characterisation of dynamic PET data*, 301–306 (Academic Press, 1996).

[168] R. Boellaard, F. E. Turkheimer, R. Hinz *et al.* "Performance of a modified supervised cluster algorithm for extracting reference region input functions from (R)-[11C]PK11195 brain PET studies". In *Nuclear Science Symposium Conference Record, 2008. NSS'08. IEEE*, 5400–5402 (IEEE, 2008).

[169] M. Yaqub, B. N. Van Berckel, A. Schuitemaker *et al.* "Optimization of supervised cluster analysis for extracting reference tissue input curves in (R)-[11C]PK11195 brain PET studies". *J Cereb Blood Flow Metab* 32, 1600–1608 (2012).

[170] Z. Su, K. Herholz, A. Gerhard *et al.* "[11C]-(R)PK11195 tracer kinetics in the brain of glioma patients and a comparison of two referencing approaches". *Eur J Nucl Med Mol Imaging* 40, 1406–1419 (2013).

[171] S. Sridharan, F. X. Lepelletier, W. Trigg *et al.* "Comparative Evaluation of Three TSPO PET Radiotracers in a LPS-Induced Model of Mild Neuroinflammation in Rats". *Mol Imag Biol* 19, 77–89 (2017).

[172] L. Vomacka, N. L. Albert, S. Lindner *et al.* "TSPO imaging using the novel PET ligand [18F]GE-180: quantification approaches in patients with multiple sclerosis". *EJNMMI Res* 7, 1–9 (2017).

[173] M. E. Phelps, S. C. Huang, E. J. Hoffman *et al.* "Tomographic measurement of local cerebral glucose metabolic rate in humans with (F-18)2-fluoro-2-deoxy-D-glucose: validation of method". *Ann Neurol* 6, 371–88 (1979).

[174] G. Gründer, T. Siessmeier, C. Lange-Asschenfeldt *et al.* "[18F] Fluoroethylflumazenil: a novel tracer for PET imaging of human benzodiazepine receptors". *Eur J Nucl Med Mol Imaging* 28, 1463–1470 (2001).

[175] Y. Magata, T. Mukai, M. Ihara *et al.* "Simple analytic method of 11C-flumazenil metabolite in blood". *J Nucl Med* 44, 417–21 (2003).

[176] Z. Fan, V. Calsolaro, R. A. Atkinson *et al.* "Flutriciclamide (18F-GE180) PET: first in human PET study of novel 3rd generation in vivo marker of human translator protein". *J Nucl Med* jnumed–115 (2016).

[177] C. Feeney, G. Scott, J. Raffel *et al.* "Kinetic analysis of the translocator protein positron emission tomography ligand [18F]GE-180 in the human brain". *Eur J Nucl Med Mol Imaging* 43, 2201–2210 (2016).

[178] F. E. Turkheimer, P. Edison, N. Pavese *et al.* "Reference and target region modeling of [11C]-(R)-PK11195 brain studies". *J Nucl Med* 48, 158–67 (2007).

[179] P. Zanotti-Fregonara, B. Pascual, G. Rizzo *et al.* "Head-to-Head Comparison of 11C-PBR28 and 18F-GE180 for Quantification of the Translocator Protein in the Human Brain". *J Nucl Med* 59, 1260–1266 (2018).

[180] M. A. Kropholler, R. Boellaard, A. Schuitemaker *et al.* "Development of a tracer kinetic plasma input model for (R)-[11C]PK11195 brain studies". *J Cereb Blood Flow Metab* 25, 842–51 (2005).

[181] C. Plisson, R. N. Gunn, V. J. Cunningham *et al.* "11C-GSK189254: a selective radioligand for in vivo central nervous system imaging of histamine H3 receptors by PET". *J Nucl Med* 50, 2064–72 (2009).

[182] M. Toth, J. Haggkvist, A. Varrone *et al.* "ABC transporter-dependent brain uptake of the 5-HT1B receptor radioligand [(11)C]AZ10419369: a comparative PET study in mouse, rat, and guinea pig". *EJNMMI Res* 4, 64 (2014).

[183] H. Wadsworth, P. A. Jones, W. F. Chau *et al.* "[18F]GE-180: A novel fluorine-18 labelled PET tracer for imaging translocator protein 18kDa (TSPO)". *Bioorg Med Chem Lett* 22, 1308–1313 (2012).

[184] N. L. Albert, M. Unterrainer, D. Fleischmann *et al.* "TSPO PET for glioma imaging using the novel ligand 18F-GE-180: first results in patients with glioblastoma". *Eur J Nucl Med Mol Imaging* 44, 2230–2238 (2017).

[185] M. Unterrainer, C. Mahler, L. Vomacka *et al.* "TSPO PET with [18F]GE-180 sensitively detects focal neuroinflammation in patients with relapsing-remitting multiple sclerosis". *Eur J Nucl Med Mol Imaging* 45, 1423–1431 (2018).

[186] W. C. Kreisl, M. Fujita, Y. Fujimura *et al.* "Comparison of [11C]-(R)-PK11195 and [11C]PBR28, two radioligands for translocator protein (18kDa) in human and monkey: Implications for positron emission tomographic imaging of this inflammation biomarker". *NeuroImage* 49, 2924–2932 (2010).

[187] M. Ikawa, T. G. Lohith, S. Shrestha *et al.* "11C-ER176, a radioligand for 18-kDa translocator protein, has adequate sensitivity to robustly image all three affinity genotypes in human brain". *J Nucl Med* 58, 320–325 (2017).

[188] H. Folkersma, R. Boellaard, W. P. Vandertop *et al.* "Reference tissue models and blood-brain barrier disruption: lessons from (R)-[11C]PK11195 in traumatic brain injury". *J Nucl Med* 50, 1975–9 (2009).

[189] P. Plavén-Sigray, G. J. Matheson, Z. Cselényi *et al.* "Test-retest reliability and convergent validity of (R)-[11C]PK11195 outcome measures without arterial input function". *bioRxiv* 298992 (2018).

[190] D. N. Louis, A. Perry, G. Reifenberger *et al.* "The 2016 World Health Organization Classification of Tumors of the Central Nervous System: a summary". *Acta Neuropathol* 131, 803–20 (2016).

[191] O. Arevalo, R. Valenzuela, Y. Esquenazi *et al.* "The 2016 World Health Organization Classification of Tumors of the Central Nervous System: A Practical Approach for Gliomas, Part 1. Basic Tumor Genetics". *Neurographics* 7, 334–343 (2017).

[192] C. Houillier, X. Wang, G. Kaloshi *et al.* "IDH1 or IDH2 mutations predict longer survival and response to temozolomide in low-grade gliomas". *Neurology* 75, 1560–6 (2010).

[193] B. C. Christensen, A. A. Smith, S. Zheng *et al.* "DNA methylation, isocitrate dehydrogenase mutation, and survival in glioma". *J Natl Cancer Inst* 103, 143–53 (2011).

[194] P. Kickingereder, F. Sahm, A. Radbruch *et al.* "IDH mutation status is associated with a distinct hypoxia/angiogenesis transcriptome signature which is non-invasively predictable with rCBV imaging in human glioma". *Sci Rep* 5, 16238 (2015).

[195] J. Barajas, R. F., J. G. Hodgson, J. S. Chang *et al.* "Glioblastoma multiforme regional genetic and cellular expression patterns: influence on anatomic and physiologic MR imaging". *Radiology* 254, 564–76 (2010).

[196] C. J. Belden, P. A. Valdes, C. Ran *et al.* "Genetics of glioblastoma: a window into its imaging and histopathologic variability". *Radiographics* 31, 1717–40 (2011).

[197] K. Yamashita, A. Hiwatashi, O. Togao *et al.* "MR Imaging-Based Analysis of Glioblastoma Multiforme: Estimation of IDH1 Mutation Status". *AJNR Am J Neuroradiol* 37, 58–65 (2016).

[198] O. Arevalo, R. Valenzuela, Y. Esquenazi *et al.* "The 2016 World Health Organization Classification of Tumors of the Central Nervous System: A Practical Approach for Gliomas, Part 2. Isocitrate Dehydrogenase Status—Imaging Correlation". *Neurographics* 7, 344–349 (2017).

[199] N. L. Albert, M. Weller, B. Suchorska *et al.* "Response Assessment in Neuro-Oncology working group and European Association for Neuro-Oncology recommendations for the clinical use of PET imaging in gliomas". *Neuro Oncol* 18, 1199–208 (2016).

[200] G. Pöpperl, F. W. Kreth, J. H. Mehrkens *et al.* "FET PET for the evaluation of untreated gliomas: correlation of FET uptake and uptake kinetics with tumour grading". *Eur J Nucl Med Mol Imaging* 34, 1933–42 (2007).

[201] Kunz, M. and Thon, N. and Eigenbrod, S. and Hartmann, C. and Egensperger, R. and Herms, J. and Geisler, J. and la Fougere, C. and Lutz, J. and Linn, J. and Kreth, S. and von Deimling, A. and Tonn, J. C. and Kretzschmar, H. A. and Pöpperl, G. and Kreth, F. W. "Hot spots in dynamic (18)FET-PET delineate malignant tumor parts within suspected WHO grade II gliomas". *Neuro Oncol* 13, 307–16 (2011).

[202] N. L. Jansen, B. Suchorska, V. Wenter *et al.* "Dynamic 18F-FET PET in newly diagnosed astrocytic low-grade glioma identifies high-risk patients". *J Nucl Med* jnumed–113 (2014).

[203] N. L. Albert, I. Winkelmann, B. Suchorska *et al.* "Early static 18F-FET-PET scans have a higher accuracy for glioma grading than the standard 20–40 min scans". *Eur J Nucl Med Mol Imaging* 43, 1105–1114 (2016).

[204] B. Suchorska, A. Giese, A. Biczok *et al.* "Identification of time-to-peak on dynamic 18F-FET-PET as a prognostic marker specifically in IDH1/2 mutant diffuse astrocytoma". *Neuro Oncol* 20, 279–288 (2018).

[205] D. Pauleit, F. Floeth, H. Herzog *et al.* "Whole-body distribution and dosimetry of O-(2-[18F]fluoroethyl)-L-tyrosine". *Eur J Nucl Med Mol Imaging* 30, 519–524 (2003).

[206] K. J. Langen, K. Hamacher, M. Weckesser *et al.* "O-(2-[18F]fluoroethyl)-L-tyrosine: uptake mechanisms and clinical applications". *Nucl Med Biol* 33, 287–94 (2006).

[207] P. Heiss, S. Mayer, M. Herz *et al.* "Investigation of transport mechanism and uptake kinetics of O-(2-[18F]fluoroethyl)-L-tyrosine in vitro and in vivo". *J Nucl Med* 40, 1367–73 (1999).

[208] T. Lahoutte, V. Caveliers, S. M. Camargo *et al.* "SPECT and PET amino acid tracer influx via system L (h4F2hc-hLAT1) and its transstimulation". *J Nucl Med* 45, 1591–6 (2004).

[209] D. Pauleit, G. Stoffels, W. Schaden *et al.* "PET with O-(2-18F-Fluoroethyl)-L-Tyrosine in peripheral tumors: first clinical results". *J Nucl Med* 46, 411–6 (2005).

[210] A. Habermeier, J. Graf, B. F. Sandhofer *et al.* "System L amino acid transporter LAT1 accumulates O-(2-fluoroethyl)-L-tyrosine (FET)". *Amino Acids* 47, 335–44 (2015).

[211] K. J. Langen, G. Stoffels, C. Filss *et al.* "Imaging of amino acid transport in brain tumours: Positron emission tomography with O-(2-[18F]fluoroethyl)-L-tyrosine (FET)". *Methods* (2017).

[212] C. Stegmayr, D. Oliveira, N. Niemietz *et al.* "Influence of Bevacizumab on Blood-Brain Barrier Permeability and O-(2-18F-Fluoroethyl)-l-Tyrosine Uptake in Rat Gliomas". *J Nucl Med* 58, 700–705 (2017).

[213] L. Vomacka, M. Unterrainer, A. Holzgreve *et al.* "Voxel-wise analysis of dynamic 18F-FET PET: a novel approach for non-invasive glioma characterisation". *EJNMMI Res* 8, 1–13 (2018).

[214] *TH1 Class Reference* (2018 (accessed October 1, 2018)). URL `https://root.cern/doc/v610/classTH1.html`.

[215] *ITK 4.11 Histogram To Texture Features Filter* (2018 (accessed October 1, 2018)). URL `https://itk.org/Doxygen411/html/classitk_1_1Statistics_1_1HistogramToTextureFeaturesFilter.html`.

[216] G. Lehmann. "Label object representation and manipulation with ITK". *Insight J* 8 (2007).

[217] T. Koopman, N. Verburg, R. C. Schuit *et al.* "Quantification of O-(2-[18F]fluoroethyl)-L-tyrosine kinetics in glioma". *EJNMMI Res* 8, 72 (2018).

[218] J. Göttler, M. Lukas, A. Kluge *et al.* "Intra-lesional spatial correlation of static and dynamic FET-PET parameters with MRI-based cerebral blood volume in patients with untreated glioma". *Eur J Nucl Med Mol Imaging* 44, 392–397 (2017).

[219] K. Zhang, K. J. Langen, I. Neuner *et al.* "Relationship of regional cerebral blood flow and kinetic behaviour of O-(2-(18)F-fluoroethyl)-L-tyrosine uptake in cerebral gliomas". *Nucl Med Commun* 35, 245–51 (2014).

[220] M. Lundemann, P. Munck Af Rosenschold, A. Muhic *et al.* "Feasibility of multiparametric PET and MRI for prediction of tumour recurrence in patients with glioblastoma". *Eur J Nucl Med Mol Imaging* (2018).

[221] S. Jan, G. Santin, D. Strul *et al.* "GATE: a simulation toolkit for PET and SPECT". *Phys Med Biol* 49, 4543–61 (2004).

[222] Y. Zhou, S.-C. Huang, M. Bergsneider and D. F. Wong. "Improved parametric image generation using spatial-temporal analysis of dynamic PET studies". *NeuroImage* 15, 697–707 (2002).

[223] M. Unterrainer, D. Fleischmann, C. Diekmann *et al.* "Comparison of 18 F-GE-180 and dynamic 18 F-FET PET in high grade glioma: a double-tracer pilot study". *Eur J Nucl Med Mol Imaging* 1–11 (2018).

List of Figures

List of Tables

Danksagung

Für die vielfältig erfahrene Unterstützung während der Promotion möchte ich mich an dieser Stelle bei allen ganz herzlich bedanken.

Mein besonderer Dank gilt meinem Betreuer PD Dr. Guido Böning für die Einführung in die objektorientierte Programmierung und die regen Diskussionen insbesondere im Hinblick auf die Gestaltung von Vorträgen und Publikationen.

Ganz herzlich bedanke ich mich bei Herrn Prof. Bartenstein für die Möglichkeit an der Klinik und Poliklinik für Nuklearmedizin zu promovieren und an einer Vielzahl von interessanten Projekten mitzuwirken. Durch seine reichhaltige Erfahrung in der nuklearmedizinischen Gehirn-Bildgebung und sein entgegengebrachtes Vertrauen fühlte ich mich stets gefördert und motiviert.

Bei meinen Kollegen Dr. Christian Zach, Dr. Markus Strigl, Georg Stark und Dr. Andreas Delker möchte ich mich für die Unterstützung bei meiner Ausbildung zur Medizinphysikexpertin bedanken.

Ein großer Dank gilt auch meinen medizinischen Kollegen PD Dr. Nathalie Albert, Dr. Marcus Unterrainer, Dr. Erik Mille, Adrien Holzgreve, Dr. Matthias Brendel und Thomas Höllbacher für die freundschaftliche Arbeitsatmosphäre und die vielen wertvollen Anregungen und fachlichen Diskussionen, welche wesentlich zum Gelingen dieser Arbeit beigetragen haben.

Für die fachliche Hilfestellung, die Unterstützung bei der Planung der Studien und bei der Erstellung der Publikationen möchte ich mich außerdem bei meinen Kollegen Dr. Simon Lindner, Prof. Sibylle Ziegler, Anika Brunegraf, Larissa Ermoschkin, Astrid Gosewisch und Julia Brosch aus der Nuklearmedizin; Prof. Martin Kerschensteiner, Prof. Tania Kümpfel und Christoph Mahler aus der Neuroimmunologie; sowie Dr. Bogdana Suchorska, Prof. Jörg-Christian Tonn und Prof. Friedrich-Wilhelm Kreth aus der Neurochirurgie bedanken.

Mein größter Dank gilt meiner Familie, meinen Freunden und ganz besonders meinem Mann Mathias Kaiser für die liebevolle Unterstützung, Aufmunterung und Geduld während der Erarbeitung meiner Dissertation.